Università degli studi di Udine

Corso di dottorato di ricerca in:
Informatica e Scienze Matematiche e Fisiche
Ciclo XXXVI

Study of the divergent pointing mode for the Cherenkov Telescope Array Observatory Southern array

Candidata:
Irene Burelli

Supervisore:
Prof. ssa Barbara De Lotto

Co-supervisori:
Prof. Francesco Longo
Dr. Michele Palatiello

Anno 2024

Contents

Abstract

γ-rays are the most energetic among all electromagnetic radiation and provide us with a fascinating view of our universe under extreme conditions. Cherenkov telescopes represent one of the most efficient techniques for the ground based detection of γ-rays. The present generation of imaging atmospheric Cherenkov telescopes have taken γ-ray astronomy to an unprecedented level.The next generation of instruments for observing high-energy γ-rays is embodied by the Cherenkov Telescope Array Observatory (CTAO), which is currently under construction. More than 60 telescopes will be spread between two array sites in the Northern and Southern hemispheres, covering a wide range of energies from 20 GeV up to 300 TeV. Thanks to a sensitivity between 5 and 10 times greater than that of the current generation of instruments, CTAO will have unprecedented accuracy in high-energy γ-rays detection. While the properties of Cherenkov telescopes are optimal for the Very High Energy sky's study, the time they need to achieve target sensitivity for the observation of large sky regions is really huge, due to their limited Field of View (FoV). To optimize the time spent to perform such tasks, a so-called *divergent mode* was proposed as an alternative observation strategy to the traditional - parallel - pointing. The idea that underlies this strategy is simple: an imaginary telescope, positioned at the center of gravity of the array, is pointed to a direction of interest, and all the telescopes are tilted outward from this direction. The single telescope pointing directions are computed thanks to a simple code that only requires one input parameter, called divergence (div). This strategy, while bringing the advantage of increasing the total instantaneous arrays' FoV results in a worsening of the array performance. The goal of the studies performed on this topic is to find a balance between the FoV dimension and the array performance. Starting from 2013, when the strategy was first proposed, a few studies have been presented. Recently the Northern array performance was obtained in divergent mode. The simulations used for that study are based on an up-to-date simulation setup. The Southern site on the other hand was only simulated in older studies which were taking into account preliminary site and telescope (number and properties) definitions. This study aims at defining the Southern site performance in divergent mode for a set of configurations with different divergent setup applied. All classes of telescopes are considered and the most recent simulation configurations, for the telescope positions, cameras, optics, ecc, are used. Several scientific tasks can benefit from the enlarged FoV offered by this observation mode. Divergent pointing was part of a document stating CTA science requirements, as a strategy to perform extragalactic survey and a project referred to as *transient survey*. In recent years, with the first detection of Gravitational Wave events, the possibility to apply this strategy to look for electromagnetic counterparts of these objects has been opened. This thesis is organized as follows:

- **Chapter One**: Introduction to γ-ray astronomy and ground based detection of γ-ray sources;
- **Chapter Two**: Imaging Atmospheric Cherenkov Technique and introduction the Cherenkov Telescope Array;

- **Chapter Three**: Introduction to the pointing modes alternative to the parallel one;
- **Chapter Four**: Description of the software needed for simulations and analysis;
- **Chapter Five**: Description of the Southern site simulations and analysis of the performance;
- **Chapter Six**: Analysis of the FoV evolution while tracking an object in divergent mode;
- **Chapter Seven**: Open questions and possible alternative definitions of the divergent configuration.

In addition, contributions to the LST collaboration are reported. This chapter is devoted to some cross-check analysis performed during the calibration of the LST-1 spare CaliBox and the data analysis performed during the Burst Advocate shifts.

Chapter 1

Ground based γ-ray astronomy

The regions of our Universe showing the most extreme conditions constitute the most powerful accelerators nature offers. Astrophysical sources were, before the 1950s, the only accelerators available. Many new particles (often predicted by the theory) were discovered thanks to Cosmic Ray (CR) physics: positrons (predicted by Dirac in 1928 and discovered by Anderson in 1933), pions, muons and strange particles.
Today it is known that nature can accelerate particles to energies up to hundreds of Exa-electronvolts (EeV, 10^{18} eV). Thanks to their non charged nature astrophysical γ–rays offer the best opportunity to study the sites of particle acceleration, especially with observations ranging from 100 MeV to over 100 TeV.
In this chapter I will introduce Cosmic Rays, their discovery, spectra and composition, Very High Energy (VHE) γ-rays, focusing on the processes of emission and acceleration of the emitting particles, and the processes that lead to ground based detection of this extremely energetic radiation.

1.1 Cosmic Rays

The origin of Cosmic Rays represents one of the most challenging problems in high energy astroparticle physics. CRs, which form an important component of the non-thermal Universe, are charged particles, mainly protons, isotropically arriving at Earth. Their discovery dates back to the early 20^{th} century when the Austrian physicist Victor Hess performed a series of ascents in a hydrogen balloon to measure the radiation in the atmosphere. The aim was to look for the source of the ionizing radiation responsible for the discharge of electroscopes. Three sources were taken into consideration as a possible origin of the effect: extra-terrestrial radiation possibly from the Sun [95], radioactivity from the Earth's crust, and radioactivity in the atmosphere. The prevailing theory was that the radiation came from the Earth's rocks. In an attempt to test this hypothesis, German scientist Theodor Wulf, in 1909, measured ionization rates near the top of the Eiffel Tower (approximately 300 meters high) using a portable electroscope [108]. Though the ionization rate was expected to decrease with height, Wulf noted that the ionization rate at the tower's summit was only about half that at ground level, a far less

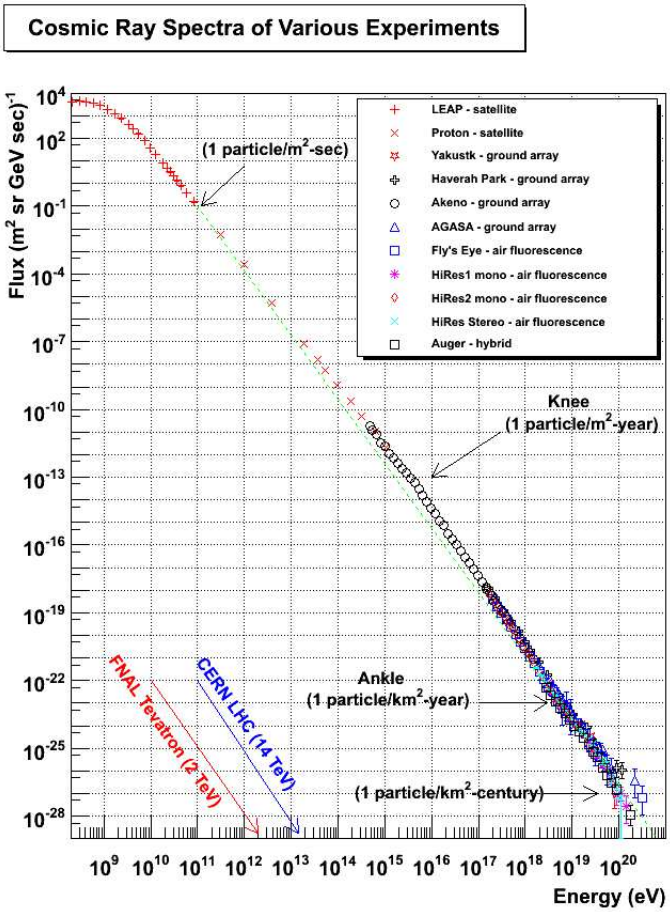

Figure 1.1: Overall differential energy spectra of Cosmic Rays from various experiments. Credits https://web.physics.utah.edu/ whanlon/spectrum.html

substantial decrease than expected. The terrestrial origin of the atmospheric ionization was also challenged by the Italian physicist DomenicoPacini, who conducted experiments underwater finding a significant decrease in the electroscopes discharge rate [89]. Following Wulf's results Hess, who supported the cosmic origin of the radiation, started a series of balloon flights that led in 1912 to the discovery that, around 5300m above sea level (a.s.l.), the ionization rate was approximately three times that at sea level. This led to the conclusion that penetrating radiation was entering Earth's atmosphere from above.

Since then their spectrum has been measured by several instruments, showing a wide energy coverage, ranging from $\sim 10^8\, eV$ up to $\sim 10^{21}\, eV$ and a smooth power law behaviour $F(E) \propto E^{-\alpha}$ (Figure 1.1). It is characterised by two identifiable features: the first one is called the knee, at about 3×10^6 GeV where the spectrum steepens from $\alpha = 2.7$ to $\alpha = 3.1$ and the other one, the ankle, at about 3×10^9 GeV where the

spectrum becomes flat again . The origin of the low-energy part (below 10 GeV) can be traced back to the Sun, the high-energy part ranging up to the knee is believed to originate from Galactic accelerators and those at higher energies from extra-galactic ones. The charged nature of Cosmic Ray particles makes it difficult to identify the sources that emit them: galactic and intergalactic magnetic fields deflect them so that the incoming direction is not related to the emitting source. a well-established fact that when charged particles undergo acceleration to reach relativistic energies, they emit γ-rays through various processes. These γ-rays, as neutral messengers, remain unaltered in their trajectory and point back to their emitting sources, offering valuable insights into the mechanisms behind Cosmic Ray acceleration and progenitors. Apart from the possibility of solving the puzzle of CR origin, γ-rays are interesting per se since they give important clues about the emission regions and emission mechanisms of various astrophysical sources. Also they can help probing frontiers in physics, e.g., they help in studying the nature of Dark Matter (DM), through indirect detection of the γ-rays resulting from the annihilation of a DM particle with the corresponding antiparticle, or understand photon propagation under quantum gravitational effects.

1.2 Very High energy γ-rays

Very High Energy (VHE) γ-ray emission involves charged particles, leptons or hadrons, which are accelerated to high energies. This emission arises from astrophysical objects powered by the release of gravitational energy and the relativistic acceleration of particles. Among the processes that can be responsible for particle acceleration the most commonly addressed are the first and second order Fermi mechanisms.

Second order Fermi mechanism

Proposed by Enrico Fermi in 1949 [53], this acceleration mechanism describes the acceleration of relativistic particles in regions characterized by very strong inhomogeneous magnetic fields. The process can be seen as the scattering of the particle by magnetic field irregularities (magnetic mirrors). The model assumes that the cloud has a mass, M, much greater than the particle mass, m, and that moves randomly with typical velocity V, in the observer's frame. In a reference frame where the mirror is at rest the scattering between the particle and the cloud can be considered elastic. In this frame the particle energy before the shock is

$$E' = \gamma_V (E + Vp\cos\theta) \tag{1.1}$$

where the non primed quantities refer to the observer's frame, with p and E being the particle's momentum and initial energy. θ is the angle between the particle initial direction and the normal to the mirror surface and

$$\gamma_V = \left(1 - \frac{V^2}{c^2}\right)^{-1/2} \tag{1.2}$$

The x-component of the relativistic three-momentum of the particle is

$$p'_x = p' \cos\theta' = \gamma_V \left(p \cos\theta + \frac{VE}{c^2} \right) \tag{1.3}$$

In the cloud reference frame the particle's energy is conserved, $E'_{before} = E'_{after}$, while the p_x component is reversed, $p'_x \longrightarrow -p'_x$. Applying this conservation relations and moving back to the observer's frame, the energy of the particle after the collision is

$$E_{after} = \gamma_V \left(E' + V p'_x \right) \tag{1.4}$$

Using the previous relations and recalling that $p_x/E = v\cos\theta/c^2$ we get

$$E_{after} = \gamma_V^2 E \left[1 + \frac{2Vv\cos\theta}{c^2} + \left(\frac{V}{c} \right)^2 \right] \tag{1.5}$$

Expanding the previous equation at first order in V/c and integrating over θ the average increase in the particle energy results to be

$$\langle \frac{\Delta E}{E} \rangle = \langle \frac{E_{after} - E}{E} \rangle = \frac{8}{3} \left(\frac{V}{c} \right)^2 \tag{1.6}$$

As the name of the process suggests, the average increase in energy is second-order in V/c. The energy gain process in this case is very slow since the speed of the cloud is much less than that of the particle making the process not really efficient.

First order Fermi mechanism

The first-order acceleration mechanism, first introduced by Fermi in 1954 [52], succeeds into describing a way to obtain an energy gain that is linear in (V/c), a condition that would make the acceleration process more effective, especially at relatively high values of V.

The model involves a strong shock propagating through a diffuse medium. The surface that separates the region behind the shock (downstream) from the surrounding medium (upstream), can be described as an abrupt discontinuity. These discontinuities are called shock waves.

When a high energy particle crosses the shock front, it obtains a small increase in energy. The particles are then scattered in the region behind the shock front and their velocity distributions become isotropic with respect to that flow. A particle moving from the downstream region to the upstream one undergoes exactly the same process of receiving a small increase in energy ΔE on crossing the shock from the downstream to the upstream flow as it did in travelling from upstream to downstream.

It can be shown that the average increase in energy at each shock front crossing is of order $\Delta E/E \sim V/c$. Let's consider a particle crossing the shock from the upstream to the downstream side. The gas on the downstream side approaches the

particle at a velocity V and so, performing a Lorentz transformation, the particle's energy when it passes into the downstream region is, as before,

$$E' = \gamma_V (E + p_x V) \tag{1.7}$$

where $p_x = p\cos\theta$, where again θ is the angle between the particle initial direction and the normal to the shock and γ_V is the same quantity defined in 1.2. The shock is assumed to be non-relativistic,$V \ll c$, $\gamma_V = 1$, but the particles are relativistic and so $E = pc$, $p_x = (E/c)\cos\theta$. Therefore,

$$\begin{aligned} \Delta E &= pV\cos\theta \\ \frac{\Delta E}{E} &= \frac{V}{c}\cos\theta \end{aligned} \tag{1.8}$$

The probability of particles crossing the shock arriving within the angles θ to $\theta + d\theta$ is proportional to $\sin\theta d\theta$. The rate at which they approach the shock front is proportional to the x-component of their velocities, $c\cos\theta$. Therefore the probability of the particles crossing the shock is proportional to $\sin\theta\cos\theta\, d\theta$. Normalising so that the integral of the probability distribution over all the particles approaching the shock is equal to 1 the mean energy gain per crossing is

$$\langle \frac{\Delta E}{E} \rangle = \frac{2}{3}\frac{V}{c} \tag{1.9}$$

As anticipated this is first order in V/c. A significant aspect of this model is that the particles undergo scattering in both the upstream and downstream regions. Although the first-order acceleration mechanism is an improvement upon the original (second order) Fermi mechanism, it remains a relatively gradual process: the particles must undergo numerous back-and-forth diffusions across the shock wave times, this process resulting into an upper limit to the energy up to which particles can be accelerated.

Accelerated particles can emit VHE γ-rays both through leptonic or hadronic channels. The main mechanisms of VHE γ-ray emission will be described in the rest of this section, for an exhaustive description a good reference is the book Radiative Processes in Astrophysics by Rybicki and Lightman [98].
In the leptonic scenario energetic electrons can produce γ-rays via inverse Compton scattering, synchrotron emission and bremsstrahlung [32]. Among these processes the most important are indubitably Inverse Compton (IC) radiation and synchrotron emission.
Electrons accelerated inside astrophysical sources typically show a power-law energy distribution of the form $\phi_e \propto E_e^{-p}$, where p is the power-law index and E_e is the energy of the electron. In the presence of a magnetic field the trajectory of these particles is bent perpendicular to the direction of the magnetic field by the Lorentz force. As the particle gyrates electromagnetic radiation is emitted. This radiation, called synchrotron radiation, in relativistic regime is beamed in the direction of the motion. For electrons

with a power-law spectrum the synchrotron radiation spectrum is

$$\phi_\gamma \propto E_\gamma^{-(p+1)/2} \tag{1.10}$$

where p is once again the power-law index describing the accelerated electrons' spectrum. Synchrotron power emitted by the charged particle is proportional to $1/m^4$, where m is the mass of the particle. Therefore this process is more efficient in case of radiating electrons and positrons compared to protons.
Inverse Compton scattering is the name used to describe the collision between low energy photons (γ_{LE}, namely photons whose energy ranges from microwaves - Cosmic Microwave Background (CMB) - to GeV (X-ray band)) and relativistic electrons. In the process electrons transfer part of their energy to photons:

$$e^- + \gamma_{LE} \rightarrow e^- + \gamma_{HE}. \tag{1.11}$$

If the energy of the photon before scattering is well below the rest mass energy of the electron, scattering takes place in what is called Thomson regime. In this regime the process cross-section, σ_T, is independent of electron or photon energy, and the number of scattered photons per unit time is constant. The energy spectrum of up-scattered photons is given by the same relation describing the flux for synchrotron emission:

$$\phi_\gamma \propto E_\gamma^{-(p+1)/2} \tag{1.12}$$

Conversely, when the photon energy before scattering is much greater than the electron's rest mass, scattering takes place in what is called Klein-Nishina regime. This time the process cross-section, σ_{KN}, depends on the energy of the electron, E_e, as well as the number of scattered photons per unit time ($n \propto E_e^{-1}$). This results in an energy spectrum of up-scattered photons given by

$$\phi_\gamma \propto E_\gamma^{-(p+1)} \tag{1.13}$$

The main hadronic channel for γ-ray production is the neutral pion (π^0) decay. When accelerated protons, collide with other protons or photons an equal number of charged (π^+/π^-) and neutral pions (π^0) are produced. Therefore 1/3rd of the produced pions are neutral. While charged pions decay producing muons and neutrinos (lifetime $\sim 10^{-8}\,s$) π^0 decay into two γ-ray photons (lifetime $\sim 10^{-16}\,s$)

$$p + p(\gamma) \rightarrow \pi^0 \rightarrow 2\gamma \tag{1.14}$$

each of which will carry about 1/6th of the primary hadron energy. If the pion flux is described by a power-law spectrum

$$\phi_{\pi^0} \propto E_{\pi^0}^{-p} \tag{1.15}$$

where p is the power law index, then the resulting γ-ray spectrum will be

$$\phi_\gamma \propto E_\gamma^{-p} \tag{1.16}$$

Cosmic Ray protons are commonly thought to be accelerated through first-order Fermi acceleration mechanism; the power-law index expected at the source is equal to -2. Being the spectrum of secondary pions similar to the one of the parent protons, the γ-rays produced will also show an E^{-2} spectrum,

1.3 γ-rays and the atmosphere

The electromagnetic spectrum ranges from radio waves to PeV energy γ rays. The Earth atmosphere is transparent only to radio waves above a certain frequency, some infrared wavelengths, visible light and ultraviolet light, as shown in Figure 1.2.

Direct detection of high energy radiation thus requires balloon-based or space-borne

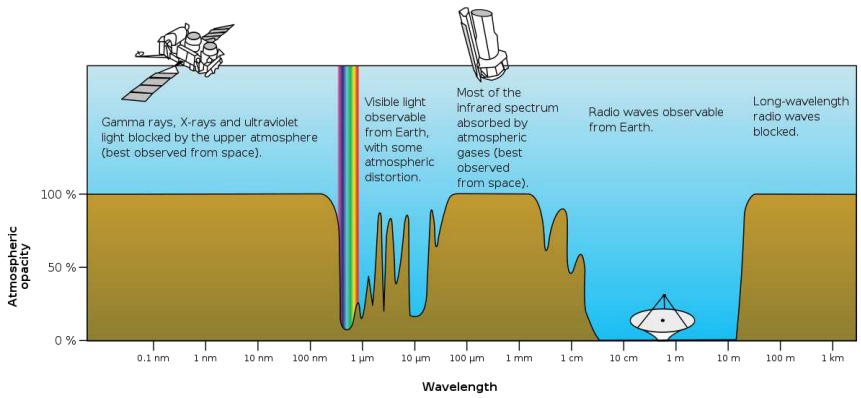

Figure 1.2: Atmospheric electromagnetic opacity as a function of radiation wavelength

instruments, which have shown to be very effective in monitoring the sky up to GeV energies. Nevertheless such a technique is no longer efficient in the VHE regime, given that the γ-ray flux is extremely low. Collection areas of balloon and satellite experiments are comparable to the physical size of these instruments, which is of the order of a ~ 1 m^2 at most. Above 100 GeV this allows detection only of a flux of the order of a single event per day, even for bright sources. For this reason scientists decided to move to ground based detectors, which allow large collection areas. VHE photons detection from the Earth is indirect. The properties of the secondary particles resulting from the interaction of the γ-rays with the atmosphere, or from the Cherenkov flashes emitted by the former, are used to infere the nature, direction, and energy of the primary particle.

Cosmic Rays and high energy γ-rays interact with atmospheric nuclei, usually several tens kilometers a.s.l. and in such collisions many new particles are created in a cascade process called Extensive Air Shower (EAS).

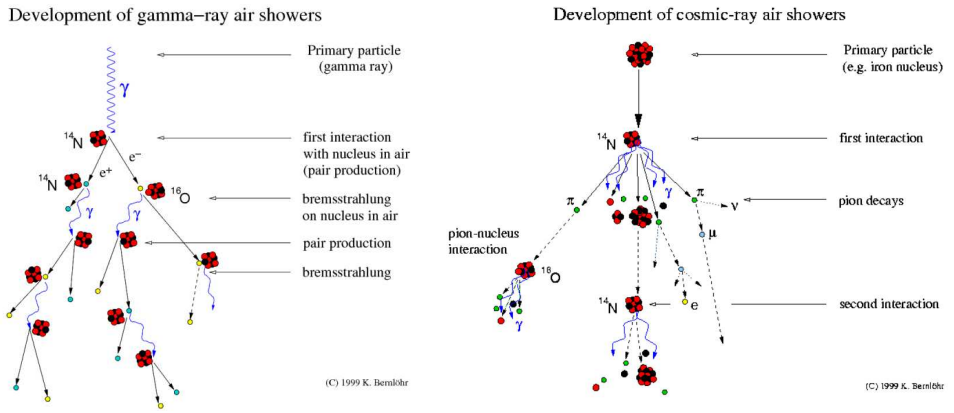

Figure 1.3: **Left**: EAS initiated by a γ-ray. **Right** EAS initiated by a Cosmic Ray. γ-ray produces electromagnetic cascade, whereas Cosmic Ray produces three overlapping cascades: electromagnetic, pionic, and nuclear. Credits: https://www.mpi-hd.mpg.de/hfm/CosmicRay/Showers.html.

Thanks to a toy model, proposed by Heitler [65], its possible to give a qualitative description of the shower developement and its main features. The model considers as a primary particle a photon of energy E_0 interacting in the atmosphere. At each interaction length X_0, defined as the grammage path length ($\int$density(x) dx) in which the particle energy is attenuated by a factor of 1/e, two new particles are created each one of them carrying 1/2 of the energy. The process goes on until the particle energy is lower than the critical energy E_c, defined as the value at which the energy losses by ionisation predominate over the processes generating the cascade. For simplicity let's consider a γ-ray generated shower. At each interaction existing γ-rays convert to electron-positron pair through pair production, while each existing electron or positron produces a new γ-ray through Bremsstrahlung. In the atmosphere, the radiation length X_0 for Bremsstrahlung and pair-production processes is about 37 g/cm^2. This means that after t radiation lengths the shower will contain $2t$ particles with an equal fraction of electrons, positrons and photons each with an average energy given by:

$$E(t) = \frac{E_0}{2^t} \tag{1.17}$$

where E_0 is the primary particle energy as it hits the atmosphere. The cascading process stops abruptly when the critical energy is reached, corresponding to a thickness of the absorber t_{max}. This quantity can be written in terms of the initial and critical energy as follows: $E_c = \frac{E_0}{2^t}$ hence $2^t = \frac{E_0}{E_c}$ and

$$t_{max} = \log_2 \frac{E_0}{E_c} \tag{1.18}$$

The maximum number of particles in the cascade depends on the primary particle

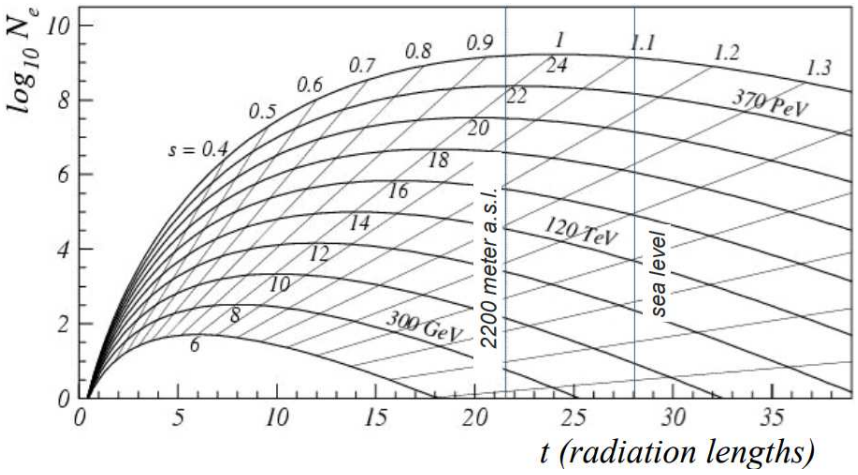

Figure 1.4: Longitudinal shower development from a photon-initiated cascade. The highlighted value of 2200m a.s.l is the typical altitude of sites hosting Imaging Atmospheric Cherenkov Telescopes. Adapted from R.M. Wagner, PhD dissertation, MPI Munich 2007

energy and is given by $N_{max} = E_0/E_c$. The shower maximum occurs at a depth

$$X_{max} = X_0 \ln \frac{E_0}{E_c} \tag{1.19}$$

along the shower axis. The number of particles as a function of depth is called the electromagnetic longitudinal profile and can be expressed with the Greisen formula [62]:

$$N_e = \frac{0.31}{\sqrt{t_{max}}} e^t s^{-3t/s} \tag{1.20}$$

where T is the atmosphere depth measured in radiation lengths (X/X_0), $t_{max} = \log_2 E_0/E_c$ and s is the so called shower age, defined as $s = 3t/(t + 2t_{max})$. In Figure 1.4 the longitudinal development of the shower in radiation lengths is reported for different values of the primary particle energy. The shower maximum occurs at $s = 1$.
This description of EAS is a simplified one which allows to have a qualitative understanding of the process. A proper treatment of the phenomena needs to take into account also the lateral distribution of the shower, determined by the multiple scattering of particles in the atmosphere.
The development of showers initiated by hadrons is different with respect to the one initiated by a γ-ray because the first interaction of this particle with the air molecules is governed by the strong force and particles such as pions are produced. Pions also decay into photons, electrons, positrons and muons generating secondary electromagnetic showers or muon-generated showers. Thanks to their long lifetime and low energy losses

almost all of the muons generated in hadronic showers reach the ground, being a good tracker of the total number of particles in the shower. Hadronic showers have also an electromagnetic contribution, coming from the decay of neutral pions, which carries, on average, one third of the total energy available from the primary particle. Due to the nature of the interactions involved, the transverse momentum of secondary particles in hadronic showers is larger than that of secondary leptons in the electromagnetic ones, resulting in showers being wider. As for electromagnetic showers the Heilter model can be used also to describe hadronic showers, obtaining a qualitative understanding of their development[84][85]. The products of the interaction between the primary particle, in this case a proton, and the atmosphere are two: one containing a charged pion, $\pi^{\pm}$, and one containing neutral pions, π^0. The former interacts producing more pions, both charged and neutral, until the pion critical energy E_c^{π} is reached. This is defined as the energy at which the decay length of a charged pion becomes less than the next interaction point. When this condition is met the charged pions decay into muons reaching the ground. Neutral pions on the other hand decay into γ-ray pairs, starting electromagnetic sub-cascades. To derive the number of particle in the shower and their energy the atmosphere can be described as a set of layers of thickness $\lambda_I \log 2$ [85], where λ_I is the interaction length of hadrons (for pions ~ 120 gcm^{-2}). If we call N_{ch} the number of charged pions produced in each layer, the corresponding number of neutral pions will be $N_{ch}/2$ and the number of charged pions after n layers will be $N_{\pi} = (N_{ch})^n$. Assuming equipartition of the energy between the particles, the energy per charged pion after the n-th interaction can be the written as:

$$E_{\pi} = \frac{E_0}{\frac{3}{2}N_{ch}} \tag{1.21}$$

The number of interactions occurring before critical energy is reached can be derived for $E_{\pi} = E_c^{\pi}$ and is equal to

$$n_c = \frac{\ln(E_0/E_c^{\pi})}{\ln(3N_{ch}/2)} \tag{1.22}$$

At the ground muons instead of pions are observed, and since almost all of them survive $N_{\pi} = N_{\mu}$ can be used. With this assumption, from 1.22, the number of pions/muons can be obtained:

$$N_{\mu} = N_{\pi} = \left(\frac{E_0}{E_c^p i}\right)^{\beta} \tag{1.23}$$

where $\beta = \ln(N_{ch})/\ln(3N_{ch}/2)$. The total number of electrons from the electromagnetic component of the shower obtained from this model underestimates the real value, which is given by [101]:

$$N_e^{max} = 6 \cdot 10^5 \left(\frac{E_0}{PeV}\right)^{1.046} \tag{1.24}$$

The other important quantity is the depth of shower maximum X_{max}, which can be calculated as the sum of the depth at which the first interaction occurs and the maximum depth of an electromagnetic shower of initial energy $E_0/(3N_{ch})$. This approximation

uses only the first generation of photons, so the resulting maximum depth will be underestimated [101]

$$X^p_{max} = \lambda_I \ln 2 + X_0 \ln \left(\frac{E_0}{3N_{ch}E_c} \right) \tag{1.25}$$

Due to the high energy of the primary particle, the secondary charged particles are produced with a high energy such that they travel in air with a speed v greater that the speed of light in that medium, namely c/n. This high speed results in the ionization of the atmospheric particles which go back to their relaxed state emitting a flash of UV radiation, the so called Cherenkov radiation. The angle of propagation of radiation with respect the particle velocity (θ in Figure 1.5) is fixed and its value can be easily derived from geometrical considerations [79]. If n is the refractive index of the medium and $\beta = v/c$ the following relation holds:

$$\cos\theta = \frac{1}{\beta n} \tag{1.26}$$

From the previous relation it can be seen that the threshold conditions for particles to

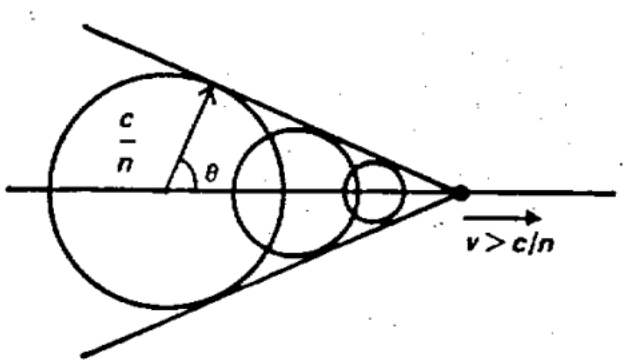

Figure 1.5: Illustration of Huygens' construction for the wavefront of coherent radiation of a charged particle moving at constant velocity $v > c/n$ through a medium of refractive index n [79]

emit Cherenkov radiation in a medium is $\beta > \frac{1}{n}$ and that the maximum value of theta is reached when particles are ultra-relativistic ($\beta \sim 1$), $cos\theta_{max} = \frac{1}{n}$.
The refractive index of air is close to 1 and its value varies with altitude (at the sea level is slightly higher, $n \sim 1.00029$, and decreases with growing altitude). This means that at the sea level the maximum emission is expected at an angle $\theta = 1.4°$, decreasing values are measured with increasing altitude ($\theta = 1°$ at 5km and $\theta = 0.66°$ at 10 km.
Therefore Cherenkov light is beamed around the direction of the incident primary particle and illuminates on the ground an area of about 250 m diameter measured at about 10 km above the sea level, referred to as the Cherenkov light pool [10]. While the area illuminated by Cherenkov photons is very large the photon density is very low (few photons per m^2 for a 100 GeV γ-ray induced shower).

1.4 Detecting γ-rays from the ground

As anticipated, small detectors onboard satellites (e.g., the Fermi Gamma Ray Observatory) allow direct observation of γ-rays up to tens of GeV. To detect photons at higher energies, where the flux is lower, it is necessary to build up ground-based detectors allowing for larger effective collection areas. Since the Earth's atmosphere is opaque to γ-rays ground-based detection must be indirect. It is important to consider the atmosphere also as part of the extended detector system, with atmospheric monitoring especially critical to ground-based γ-ray measurements.

The detection can be carried out by means of two different experimental techniques:

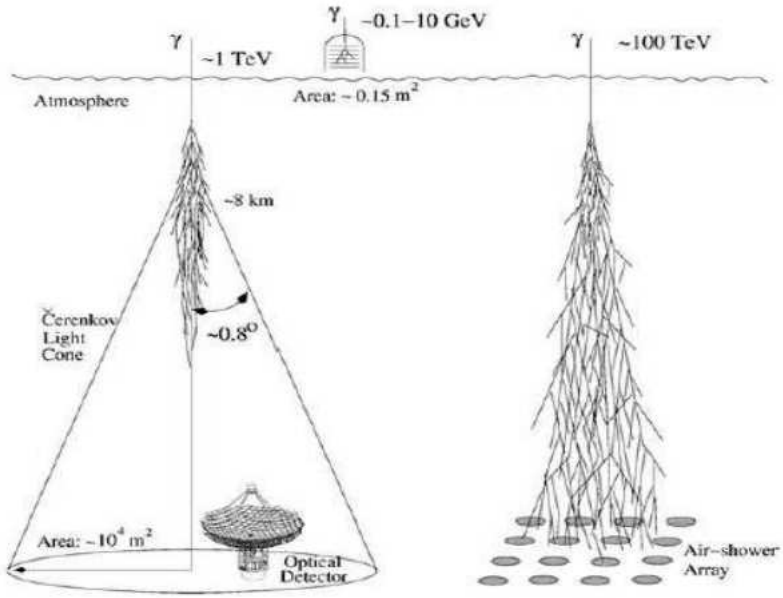

Figure 1.6: Experimental techniques used for the detection of high energy γ-rays from ground. IACT on the left and air shower array on the right. From [51]

- A calorimeter can be used to sample the number of secondary charged particles reaching the ground level (shower arrays)
- The Cherenkov light produced in air can be detected through an active inhomogeneous calorimeter, by means of telescopes (Atmospheric Cherenkov Telescopes).

Both techniques exploit the atmosphere as a calorimeter, share the same principle of reconstructing the primary γ-ray events and struggle with the same dominant Cosmic Ray background. Nevertheless, the usage of either the Cherenkov light to track the development of the shower or the remaining shower particles reaching the ground causes a number of differences between the two approaches, strongly affecting the detector

performance.
Air shower arrays directly exploit secondary particles that reach the ground providing a snapshot of the shower lateral distribution at the moment it reaches the ground. Typically they consist of a large number of charged particle detectors spread over an area of $10^4 - 10^5$ m^2 with a spacing of 10–20 m. The key observables in all air shower arrays are the local shower particle densities and the secondary particle arrival times, with which the shower arrival direction, the energy, and the nature (photon or hadron) of the primary particle are reconstructed. Detectors like these boast an extensive duty cycle, potentially reaching up to 100%, and a wide FoV. However, they tend to have a relatively high energy threshold due to the fact that high-energy showers are more penetrating and generate charged particles at lower altitudes compared to lower energy showers. Moreover, these detectors are typically positioned at altitudes around 4000 m a.s.l., condition that only allows accessing shower tails. As a consequence the number of collected particles is maximized, but the capability to discriminate the showers induced by γ-rays from the much more numerous showers induced by Cosmic Rays is rather poor. During the past decades several types of particle samplers were built, including scintillator arrays (like the Tibet experiment [19]), resistive plate chamber carpets (Argo-YBJ experiment [15]) and water Cherenkov ponds (such as Milagro [23], HAWC [5] [6] and LHAASO [33]).
Cherenkov telescopes enable the detection of air showers that have extinguished before

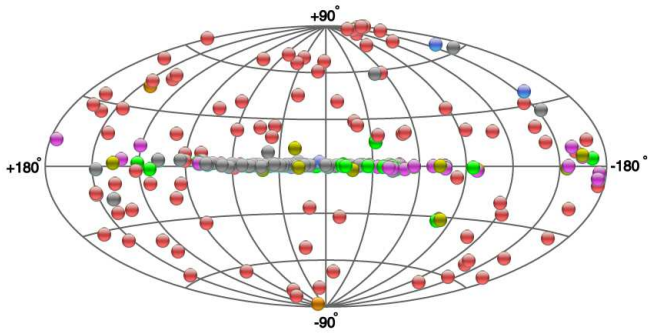

Figure 1.7: Overlay image in Galactic coordinates of the VHE sources detected by now. Color code represents the kind of sources. Data obtained using the TeVCat (`http://tevcat2.uchicago.edu` accessed on 26 August 2022) service.

reaching the ground through the observation of the Cherenkov light produced in the atmosphere. As the showers reach their maximum at the height of ∼10 km a.s.l., and the Cherenkov radiation is emitted at an angle of ∼1°, and is spread over a region with a radius of ∼120 m, the so-called light pool. The most successful technique for this kind of observations has shown to be the use of optical telescopes to record the Cherenkov light emitted, taking a sort of a “picture” of the showers. These so-called “Imaging Atmospheric Cherenkov Telescopes” (IACTs) possess a relatively small field of view, typically spanning a few degrees in angular diameter, and are characterized by a low duty

cycle (∼10%, corresponding to moonless, clear nights). However, they compensate for this limitation with a very large effective area, equivalent size of the light-pool (projection on the ground of the Cherenkov light cone) illuminated by the showers ($\sim 10^5$ m^2). Robust background rejection capabilities, approaching approximately 90% effectiveness, as detailed in [18] is also property of tehse instruments. IACTs are composed by a mirror dish, acting as the Cherenkov photons collector and a camera, converting the Cherenkov light into a digital image of the shower.
During the last 30 years or so instruments exploiting both techniques allowed us to detect almost ~ 250 sources at VHE (see Figure 1.7). The table in Figure 1.8 summarizes the basic performance parameters the two classes of detectors. The performance parameters of both types of instruments show an improvement with energy. The table reports angular and energy resolutions for the best sensitivity range.
The relatively higher energy threshold (*sim* 10 TeV) of SA can be explained taking into account that low-energy (sub-TeV) showers develop mainly in the higher layers of the atmosphere (see Figure 1.4), and only a small number of particles will reach the ground, providing little input for the SA.

Characteristic	IACT	SA/WCD
Energy threshold	$\sim$ tens of GeV (for a few hundred m^2 mirror dish)	∼TeV
Duty cycle	$\sim$ 10%	$\lesssim$ 100%
Field of view	$\sim$ a few millisr	$\sim$ sr
Energy resolution	$\sim$ 15%	$\sim$ 40%
Angular resolution	$\sim 0.1^\circ$	$\sim 0.2^\circ$
Sensitivity	$\sim$ 1% Crab Nebula flux in 25 h	a few % Crab Nebula flux in 5 yr
Main present instruments	H.E.S.S., MAGIC, VERITAS	Tibet AS-γ, HAWC, LHAASO-WCDA, LHAASO-KM2A
Future instruments	CTA	SWGO, ALPACA

Figure 1.8: Comparison of the typical performance parameters of IACT and SA instruments. Due to the energy dependence of the performance parameters, the energy resolution, angular resolution and sensitivity are given for the best sensitivity range the instruments. From [100]

On the other hand, SAs are not limited to observations during moonless and good weather nights, and have a large field of view (FoV) that allows a continuous monitoring of a large fraction of the sky. This difference leads to difficulty in the comparison of the sensitivity of the two types of instruments [100]. Although for transient phenomena and short-term variability IACTs are clearly superior, the possibility of integration of a large exposure by SA instrument owing to its broad FoV provide an efficient method both for studies of steady sources, and for unbiased studies of the typical states of variable emitters. Those differences are reflected in the exposure times quoted for sensitivity calculations: 1 or 5 years for SAs and 50 h for IACTs.

Chapter 2

Imaging Atmospheric Cherenkov Telescopes

The Imaging Atmospheric Cherenkov technique is one of the most successful ways to detect γ-ray sources from the ground level. Due to the properties of the Cherenkov signal a large mirror dish and a fast photon detector (camera, trigger and data acquisition system) are required to collect Cherenkov photons, record them and convert Cherenkov light to an image of the shower. The non straightforward part in IACT technique is related to the γ-ray discrimination against background and reconstruction. The most successful approach by far is the stereoscopic imaging technique: large convex reflectors, constituted by several mirrors, focus Cherenkov photons onto a camera, endowed with a large number of photo-detector pixels.
In this chapter I will summarize the historical development of this technique and describe the current operating facilities and the Cherenkov Telescope Array Observatory, that represents the future generation of IACTs.

2.1 The atmospheric Cherenkov technique

The first experimental evidences of what we today call Cherenkov light dates back to 1910, when Marie Curie classified it as some sort of luminescence. In the 1920s some systematic studies were performed by Mallet, a french scientist who could give a description of the phenomena and measure its continuous emission spectrum. The absence of emission lines reported in this study contradicted the previous interpretation of a luminescence phenomena.
Cherenkov radiation is named after the PhD student Pavel Cherenkov who in 1934 published a paper [36] explaining the origin of the "bluish luminescence" he was studying. This first paper was followed by a second one in 1937 [35] where Cherenkov experimentally showed the anisotropic nature of the emission; light is emitted only within a cone beamed in the direction of the particle's motion. A theoretical explanation of the phenomenon came in the same years by Igor Tamm and Ilya Frank [56].
Cherenkov emission in the atmosphere was not observed until 1953. As early as is 1948,

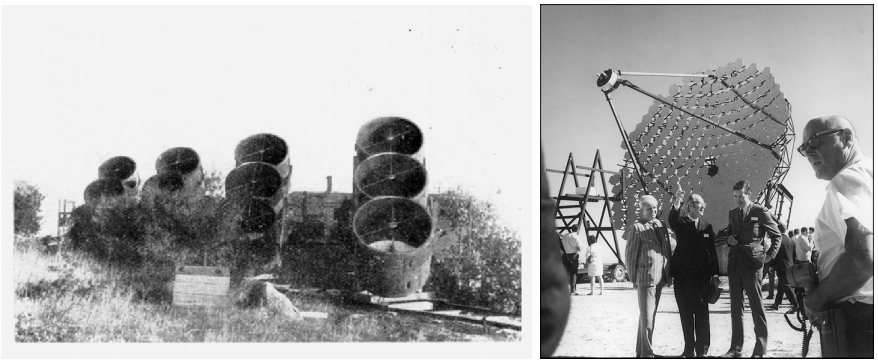

Figure 2.1: **Left**: The first γ-ray telescope constructed by Chudakov and operated in Katsiveli, Crimea in 1960-1963 [77]. **Right**: Fred Lawrence Whipple (middle) at the 10-m Gamma Ray Reflector on the day the "Mount Hopkins Observatory" opened its doors in 1968. It was renamed the Fred Lawrence Whipple Observatory in honor of Dr. Whipple in 1981.

Patrick Blackett, during his investigation of the light emitted from the night sky and aurorae, estimated that a 10^{-4} part of this light should be attributed to the Cherenkov light emitted in the atmosphere air shower elementary particles. Meanwhile J.V. Jelley and W. Galbraith were also experimenting with Cherenkov light emission, but using water. In 1952 they built a simple setup, a 25 cm diameter parabolic signaling mirror fixed into a dustbin with a short focal length, and a single 5 cm Photomultiplier Tube (PMT) in its focus, that in a short time allowed them to observe for the first time pulses of UV light coming from the atmosphere. The discovery was published in 1953 [58] and marked the beginning of atmospheric Cherenkov technique and measurements.
In 1959 Giuseppe Cocconi suggested constructing an air shower array at a high altitude above sea level with an angular resolution of $\sim 1^{\circ}$ to measure γ-rays from cosmic sources at TeV energies. He made some very optimistic predictions on the possible flux of γ-rays from the Crab Nebula, which were predicted to be about 10^3 times higher than the background.
In 1960 Alexander Chudakov and his colleagues built a system of 4 telescopes, whose number was increased to 12 the following year, in Katsiveli, Crimea, near the shore of the Black Sea, starting the era of the so called first generation Cherenkov telescopes [77][86]. These were mostly built recycling old military equipment, smartly adapted to scientific purposes. Cameras were already made of Photomultiplier tubes (PMTs) but the energy threshold was too high and background rejection not good enough to allow the detection of any source. Nonetheless these instruments allowed to set upper limits for some sources which were expected to emit VHE γ-rays. It is interesting to note that already at that time some researchers clearly understood the potential of the coincidence measurements, allowing to separate real showers from background events. This strategy is also known as stereoscopic technique.
The second generation of telescopes allowed to finally detect γ-ray signal. In 1967 Gio-

Figure 2.2: Currently operating IACT facilities.

vanni Fazio and colleagues began constructing a 10m diameter telescope on mount Hopkins, at the Whipple observatory at a height of 2300m a.s.l. For nearly 20 years Whipple allowed to observe a signal from Crab at the limit of detection level ($\sim 3-5\,\sigma$). Finally a clear detection of Crab Nebula form Whipple happened in 1989 with a significance of 9σ [106]. This observation marked the beginning of Imaging Cherenkov Astronomy.
To the same generation of instrumentation belongs HEGRA (High Energy Gamma Ray Astronomy). The stereoscopic system imaging air Cherenkov telescopes was located on the Roque de los Muchachos Observatory (ORM) on the Canary island of La Palma, at an altitude of 2,200 m above sea level and started operations in late fall 1991. The construction went on for a few years and finally, in 1997 the array of five telescopes was completed. The telescopes were arranged on the corners of a square with a side length of 100 m with a fifth telescope positioned in the center. HEGRA operated until 2002. The overall relative operation efficiency of the HEGRA system of Cherenkov telescopes reached 85% of the total available darkness time such that 5,500 hours of data on more than 100 objects and various scans were collected in 67 months of operation [11]. The major stereoscopic IACT systems currently operating, MAGIC, H.E.S.S. and VERITAS, also called third generation Cherenkov telescopes, are shown in Figure 2.2. The High Energy Stereoscopic System (H.E.S.S.) is located in the desert of Namibia and started its operations in 2003 with the H.E.S.S. I array and since 2012 it operates in the H.E.S.S. II array configuration. It consists of five telescopes, four with a diameter of 13 m (H.E.S.S. I) plus a fifth one, built in 2012, with a diameter of 28 m. This last telescope was built to lower the energy threshold of the array and improve its sensitivity [61]. The energy range covered spans from 10s of GeV to 10s of TeV. It is the only IACT system currently

located in the Southern hemisphere. The field of view is of 5° for the H.E.S.S. I system and 3.2° for the central telescope.
The two Major Atmospheric Gamma-Ray Cherenkov telescopes, MAGIC, started operations in 2004 (MAGIC I) and 2009 (MAGIC II). Both of them have a parabolic dish with a diameter of 17 m and cover the energy range between 50 GeV and more than 50 TeV [17] with a field of view of 3.5 deg. MAGIC is constructed to maximize the repositioning speed in order to quickly react to alerts for transient events like Gamma Ray Bursts. It is able to react to them within a very short delay of around 30 seconds including redirecting the telescope axis and reloading software and trigger tables.
The Very Energetic Radiation Imaging Telescope Array System, VERITAS, was built in 2007 in the same site that used to host the Whipple telescope, the Fred Lawrence Whipple Observatory, Southern Arizona. This is a system of four 12m IACTs operating in an energy range going from $\sim$ 85 GeV to more than 30 TeV [91].
All these instruments have shown the potential of the IACT technique. Still many important questions important questions about γ-ray sources they observe are open. A significant improvement in sensitivity at TeV energies is required in order to achieve a deeper understanding of the sky in this energy range. Of fundamental importance are also a wider energy coverage in the band ranging from tens of GeV to hundreds of TeV and an improved angular and energy resolution with respect to the currently operating facilities. This idea has led to the project of the Cherenkov Telescope Array Observatory (CTAO [109]). In this work the acronym CTA will be used when referring to the array of telescopes, while CTAO will be used when referring to the Observatory infrastructure.

2.2 The Cherenkov Telescope Array

CTAO will comprise $\sim$ 100 IACTs located in two sites: one in the Northern hemisphere, on the Canary island of La Palma (same site currently hosting the MAGIC telescopes) and one in the Southern hemisphere in the Atacama desert, Chile. This will allow a full sky coverage, a necessary feature because many phenomena to be studied are rare and individual objects can be very important. In order to fulfill the requirement of a large energy band coverage, three classes of telescopes with different characteristics will be constructed. The motivations for a wide energy range are multiple: the lowest energies provide access to the whole universe (γ-γ absorption on the Extragalactic Background Light - EBL - is lower at lower energies), while highest energies are needed to study extreme accelerators. We know they are present in our Galaxy thanks to the observations of PeV γ-rays (these must be emitted in the Galaxy neighbourhood, otherwise they would be absorbed by the EBL). Furthermore a wide energy range maximizes the chance of serendipitous measurements of new classes of sources with unknown spectra.
After more than a decade the CTA project design phase is almost over. The design of the telescope ground positions arrangement, in the full-scope configuration, foresees concentric sub-array layouts, one per telescope type, with an increasing averaged distance between neighboring telescopes when moving outwards [109].

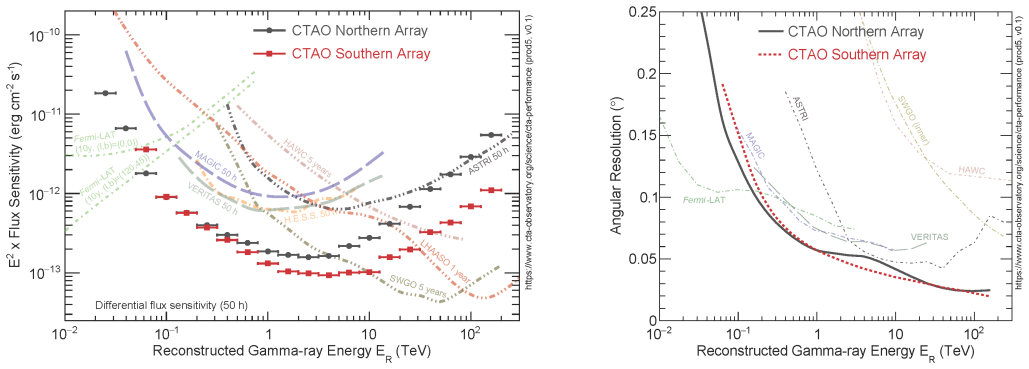

Figure 2.3: On-axis differential flux sensitivity (**Left**) and angular resolution vs. reconstructed energy curve (**Right:**) for point-like sources of the two CTAO arrays compared to that of external facilities with an overlapping energy range [38].

- **The Large Size Telescopes(LSTs)**:
  This class of telescopes will cover the energy range between 20 GeV and 3 TeV. At the lowest energies, γ-rays are abundant but their Cherenkov flashes are very faint. Thanks to this condition a small number of telescopes with large reflective surfaces (light-collection areas) is sufficient. LSTs will have a primary mirror with a diameter of 23m, a focal length of 28m and a FoV diameter of 4.3 deg. A prototype of the LST (LST-1) is currently in commissioning phase since 2018 in La Palma. The lightweight LST structure is designed to allow fast slewing, and hence facilitate follow-up observations of transients. Due to its position LST-1 performs a lot of observations jointly with the MAGIC telescopes and a pipeline for the analysis of the joint data is under development [42].

- **The Medium Size Telescopes (MSTs)**:
  MSTs will be present in a large number on both sites. The primary mirror will have a diameter of 11.5 m and the camera will allow to cover a FoV of $\sim$ 7.5 deg. MSTs have been optimized for the core VHE range, i.e. the TeV range, and the same optical design as H.E.S.S. and VERITAS. For this class of telescopes two different camera designs have been approved, the so called NectarCam [103], similar to the H.E.S.S. one, which will be implemented in the Northern site and the FlashCam [93] which will be used for the MSTs in the Southern site. A MST prototype was deployed in Berlin in 2012 and is currently undergoing performance testing. The main purpose of the prototype is to validate the design of the individual components, test the interfaces and define the assembly process of the product.

- **The Small Size Telescopes (SSTs)**:
  At the highest energies (1 to 300 TeV), γ-ray photons are rare but their Cherenkov light flashes very bright and hence associated to large light pools. This condition requires a huge number of telescopes spread over a large area. This led to the design

of the SSTs, a rather small IACT compared with the existing. The structure will be different with respect to the previous two classes. They will have a primary mirror with a diameter of 4.3 m and a secondary monolithic one with a diameter of 1.8 m. The FoV will be quite wide, 10.5 deg. An SST prototype called ASTRI operates at the Astrophysical Observatory of Catania in Serra La Nave (Etna, Sicily)

Figure 2.4: **Left**: Picture of the LST1 prototype. **Center**: MST prototype hosted in Berlin, undergoing performance testing. **Right**: ASTRI telescope at Serra La Nave, Catania.

In the initial configuration, called Alpha Configuration (Figure 2.6), the CTAO Northern Array, located in the Observatorio Roque de los Muchachos, comprises 4 LSTs and 9 MSTs, covering an area of about $0,25 km^2$. The CTAO Southern Array, situated in the Atacama desert, approximately 11 kilometers southeast of the European Southern Observatory (ESO) Paranal Observatory, consists of 14 MSTs and 37 SSTs, with an overall footprint of about $3\,km^2$. A specialization of the two observation stations forseen in terms of core science cases: the Southern one will focus on the Galactic targets whose visibility is better from the Southern hemisphere, leaving to the Northern one the extra-Galactic ones. Already in the Alpha Configuration a significant improvement in sensitivity is expected, over the entire energy range, with respect to current facilities. In particular, the on-axis differential sensitivity for 50 hr of observations will be a factor 5 to 10 better than the MAGIC/H.E.S.S./VERITAS one. Multi-square-kilometre collection area is essential at the highest energies where there is essentially zero background even in long exposures and sensitivity is limited by the collection of sufficient signal photons. CTAO has been designed to rapidly respond to external alerts, and rapidly issue its own alerts. In particular the LSTs are optimised for rapid movement, with a goal slewing time of 20 s (minimum requirement 50 s) to anywhere in the observable sky. This feature, together with a real-time analysis pipeline, will enable the identification of significant γ-ray activity in any part of the field of view and the issuing of alerts to other instruments within one minute.
The plot in Figure 2.3 shows the state-of-art performance derived from detailed Mon-

	LST	MST	SST
energy range of optimization	20-150 GeV	0.15-5 TeV	5-300 TeV
optical design	parabolic	Davies-Cotton	Schwarzchild-Couder
primary dish diameter	23 m	12 m	4.3 m
focal length	28 m	16 m	2.15 m
total weight	100 tonne	82 tonne	17.5 tonne
type of camera sensors	PMTs	PMTs	SiPMs
number of pixels	1855	1855 (NectarCam) 1764 (FlashCam)	2048
camera FoV	4.3°	~7°	8.8°

Figure 2.5: Main parameters of the three types of CTAO telescopes. The table is split into three sections: the first one refers to the driving energy range considered for the optimization of the design, the second section refers to mechanical and optical parameters, whereas the last one to the camera parameters [109]

teCarlo (MC) studies using an updated detector model of the CTAO telescopes, and optimized array layouts (the so-called 'Production 5' or 'Prod5' [38]).

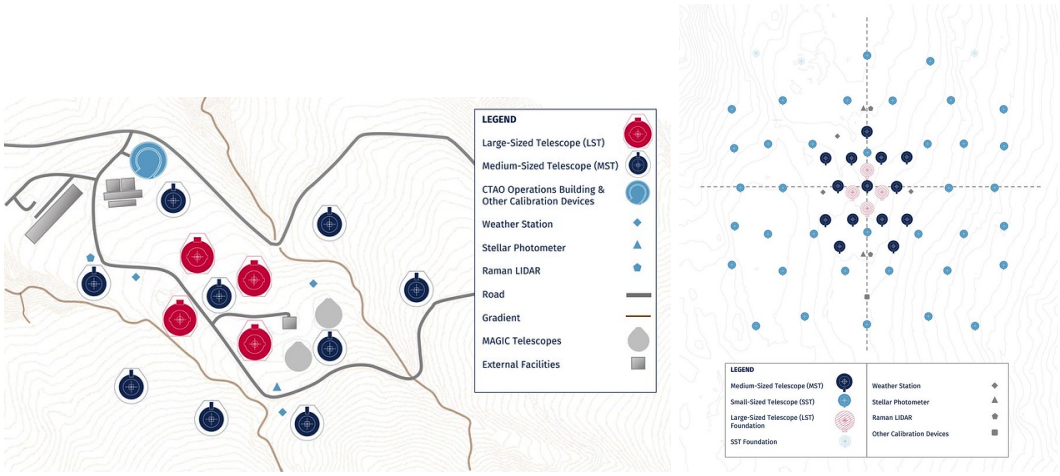

Figure 2.6: Preliminary layouts of the two CTAO arrays of the Alpha Configuration. **Left**: Northern Array in the Canary island of La Palma (Spain). **Right**: Southern Array at Paranal (Chile) [38].

2.2.1 Scientific objectives of CTAO

For the first time in Very High Energy astronomy CTAO will be operated as an open, proposal-driven observatory. The observatory-mode operation of CTA is expected to significantly boost scientific output by engaging a research community much wider than the historical ground-based γ-ray astronomy community.

Over the observatory lifetime most of the available observation time will be split into open time and time dedicated to the Core Program consisting of a list o Key Science Projects [37], to which approximately 40% of the time will be devoted during the first 10 years. Open time be allocated to Guest Observer proposers based on scientific merit and awarded by a Time Allocation Committee. Nine Key Science projects are defined: Galactic Centre, Star Forming Systems, Galactic Plane Survey, Transients, Active Galactic Nuclei, Large Magellanic Cloud Survey, Cosmic Ray PeVatrons, Clusters of Galaxies and Extragalactic survey. They will enhance our knowledge of the high-energy Universe and provide new insight into the open questions of astrophysics, theoretical physics, and particle physics. When the Observatory will be operational the KSPs will need to be revised, to match the effective properties of CTA (number of telescopes, time availability for the different tasks) and because of the new scientific discoveries that have happened since 2018 (such as the association of GW and GRBs [2][1], the detection of a neutrino signal during an AGN flare[70] and the detection of GRBs at VHE [82]. Some of the scientific groups of CTA already published their study presenting an update on the scientific interest and needs for the topics of their interest. For such tasks, the most recent works will be cited in the following section. Even taking into account the aforementioned changes the goal of the observatory is still to address a wide range of major questions in and beyond astrophysics, which can be grouped into three broad themes:

- Understanding the origin and role of relativistic cosmic particles
- Probing extreme astrophysical environments
- Exploring physics frontiers

To address these themes CTA will exploit synergies with currently operating and forthcoming instruments seeking Gravitational Wave (GW) and astrophysical neutrino detection as well as with other photon observatories. A brief description of the KSPs is given in the rest of this section, a complete description of the science goals of CTAO can be found in the document "Science with the Cherenkov Telescope Array" [37].

Galactic Center

The region within a few degrees of the Galactic Centre is one of the most studied regions of the sky in nearly every wave-band because of the wide variety of possible emitters. The region yielded notable scientific breakthroughs including the discovery of an unidentified point-like γ-ray source in the galactic center [12][20] possibly associated with $SgrA^*$ and a complex pattern of diffuse emission which might be a probe of a local PeV Cosmic-Ray acceleration in the recent past [66]. CTAO will allow us to conduct a comprehensive examination, in-depth examination of the Galactic Center region, providing unprecedented spatial and spectral insights into this complex area. This comprehensive study holds the potential to accomplish several critical goals, including the identification of the central source, the clarification of various models proposed to explain the observed extended emission, and a more profound understanding of the mechanisms underlying cosmic-ray acceleration within our Milky Way.

Survey of the Large Magellanic Cloud (LMC)

The Large Magellanic Cloud (LMC) galaxy hosts extraordinary objects, including one of the most active star-forming regions in the local group of galaxies. This activity is attested by the presence of a large number of Supernova Remnants (SNRs), dozens to hundreds of atomic hydrogen (HII) regions, bubbles and shells observed at various wavelengths. All of these structures are promising sources of γ-rays. LMC is thus a unique place to obtain a significantly-resolved global view of a star-forming galaxy at very high energies. Thanks to Fermi-LAT and H.E.S.S. a small number of sources, some of uncertain nature, have already been observed, paving the way for further and deeper explore the entire LMC with CTAO. The scientific objectives of the survey comprise:

- population studies of the particle accelerators aimed at determining if the sources in the LMC are different in any way from the γ-ray source classes known today?
- analysis of the interstellar medium and galactic CRs lifecycle. Production and propagation models for CRs can be studied in an environment with different properties with respect to the Milky Way.

A detailed study of the detection prospects for the LMC survey with CTA is presented in a recent work by CTA Consortium [9]. The LMC is also a suitable target to investigate the nature of DM. More than half of the LMC mass is due to its dark halo, and from the analysis of the rotational curves of the LMC turns out that it must contain a dark compact bulge with an anomalously high mass-to-luminosity ratio compared to that calculated for the Milky Way.

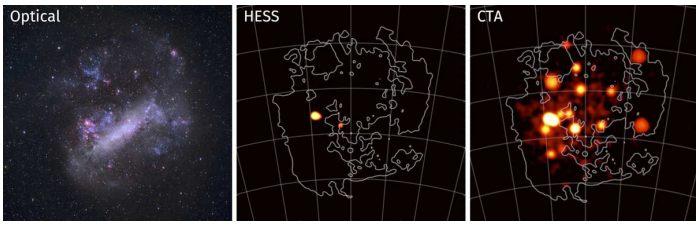

Figure 2.7: The Large Magellanic Cloud survey comparison. A comparison of CTAO's survey of the LMC (simulated) compared with optical and H.E.S.S. current images. From https://www.cta-observatory.org/.

Galactic Plane Survey (GPS)

Astronomical surveys of the Galaxy provide essential, large-scale datasets that form the foundation for Galactic science at all photon energies. The region within a few degrees of the Galactic Centre contains a wide variety of possible high-energy emitters, including multiple SNR and pulsar wind nebulae, as well as structures like dense molecular clouds, strong star-forming activity and the base of what may be

large-scale Galactic outflows (commonly referred to as the *Fermi bubbles*). CTAO survey of the Galactic Plane fulfill a number of important science goals:

- provide a census of Galactic VHE γ-ray source populations, through the detection of hundreds of new sources. This will substantially increase the Galactic source count and allow more advanced population studies,
- identify a list of promising targets for follow-up observations, such as new γ-ray binaries and PeVatron candidates,
- determine the properties of the diffuse Galactic plane emission
- produce a multi-purpose, legacy data set, comprising the complete Galactic plane at very high energies, that will have long-lasting value to the entire astronomical and astroparticle physics communities
- unveil new and unexpected phenomena in the Galaxy, such as new source classes and new types of transient and variable behavior

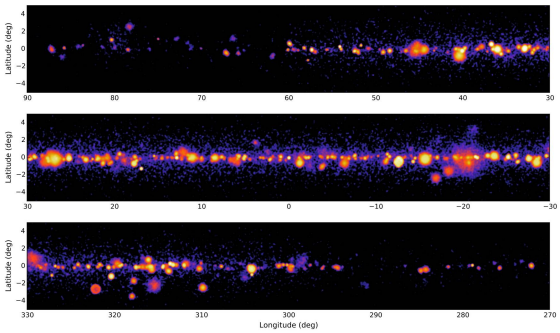

Figure 2.8: Simulated sky map showing the inner region ($-90° < l < 90°$) of the galactic plane that will be obtained during the CTA galactic plane survey. From https://www.cta-observatory.org/.

The GPS will consist of observations of the entire Galactic plane using both the Southern and Northern CTA arrays. The target sensitivity for isolated point-like sources is, at integral photon fluxes above 1 TeV, $\approx 5{\times}10^{-14}$ cm^{-2} s^{-1} A snapshot of the status of the project, together with predictions and expected results is presented in [94]. Not only the paper does describe in detail the simulation parameters taken into account, but studies on the optimization of the pointing strategy are also reported. The results presented provide a reasonable baseline of the expected scientific outcome of this project.

Galaxy Clusters

Clusters of galaxies represent the most advanced stage in the ongoing process of cosmic structure formation. These clusters are the largest gravitationally bound systems within the Universe, boasting radii on the order of a few megaparsecs and masses typically ranging from 10^{14} to 10^{15} times the mass of our Sun ($M_\odot$).

Galaxies and gas contribute roughly 5% and 15%, respectively, to the mass of the cluster, while the remaining 80% of is in the form of dark matter. They are thus expected to be reservoirs of CRs accelerated by structure formation processes, galaxies and Active Galactic Nuclei (AGN) as well as excellent targets for the search of γ-ray signals from DM annihilation. Based on simulations, the capabilities of CTA are expected to enable the establishment of groundbreaking limits on the CR proton content within galaxy clusters. Such findings could potentially necessitate a significant reevaluation of the current paradigm regarding the acceleration and confinement of protons inside clusters. The detection of diffuse γ-ray emission originating from clusters of galaxies would introduce a novel category of γ-ray sources. Consequently, this achievement would be of considerable significance and could potentially revolutionize our understanding of cosmic-ray acceleration and its interplay with large-scale structure formation processes, the inter-cluster medium, and magnetic fields.

Cosmic Ray PeVatrons

The spectrum of cosmic rays observed at Earth is largely dominated by protons up an energy of a few peta-electronvolts (1PeV=10^{15} eV), indicating that there must exist cosmic ray factories accelerating particles to PeV energies, or PeVatrons. The Galactic magnetic fields lead to the deflection of Cosmic Rays, making it challenging to determine the source location through measurements of their arrival direction on Earth. However, when target nuclei are present at or near the site of CR acceleration, the interaction between these accelerated CRs and the target nuclei generates secondary γ-rays, along with neutrinos. Consequently, by studying Galactic γ-ray sources, it becomes possible to discern the positions of PeVatrons, which are the sources responsible for accelerating CRs to PeV energies. The Galactic Center shows emission at PeV energies and, recently, LHAASO

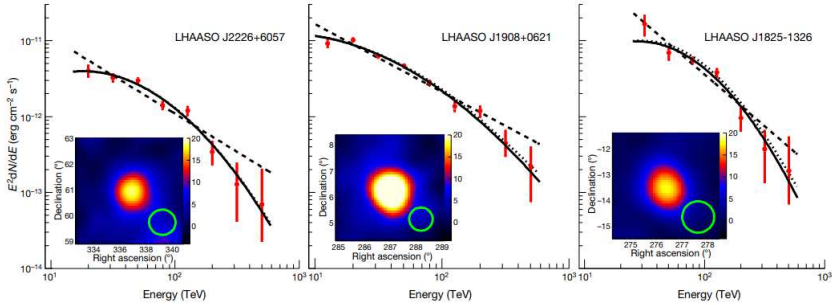

Figure 2.9: Spectral energy distributions and significance maps for LHAASO J2226+6057 (left), LHAASO J1908+0621 (center), and LHAASO J1825-1326 (right) [34]

collaboration presented the observation of photons up to 1.4 PeV from 12 galactic sources [34]. Excluding the Crab Nebula, which is a widely accepted PeVatron emitter, LHAASO reported detections have some possible counterparts in their

proximity, including pulsar wind nebulae, supernova remnants and star-forming regions but have not yet been firmly localized. The deep investigation of these sources using CTA at full sensitivity will provide crucial information possibly including a firmer association, thanks to CTA angular sensitivity.
A discussion on the ability of CTA to detect hadronic PeVatrons is presented by the CTA Consortium [8], with a focus on CTA spectral capabilities. The study also investigates the capabilities of CTA to test the leading hypothesis that SNRs are responsible for the acceleration of Galactic PeV CRs, stating that detection is expected from multiple sources. From the simulations studies it is concluded that, while CTA will have limited spectral sensitivity to search for PeVatrons in scanning mode with GPS data, the prospects to find PeVatrons are excellent in deep observations.

Star Forming Systems

Cosmic rays are considered a significant factor in regulating the process of star formation. Therefore, it is crucial to gain an understanding of the locations where CRs are accelerated, how they propagate through space, and where they interact within the interstellar medium (ISM). This knowledge is essential for comprehending the intricate interplay between cosmic rays and the mechanisms that drive the formation of stars within galaxies. γ-rays coming from the interaction of cosmic rays with the ambient gas and radiation fields are among the best tools to study cosmic-ray properties in star-forming environments. CTA observations of star-forming systems spanning a wide range of star-formation rates (SFR) across six orders of magnitude are poised to offer valuable insights into the connection between high-energy particles and the star-formation process. Through this Key Science Project (KSP), legacy data products will be generated, benefiting the entire astronomical community. These data products will include catalogs of sources, flux maps, and data cubes (such as γ-ray excess maps binned in energy) for regions of interest, including Cygnus and Carina.

Active Galactic Nuclei (AGN)

VHE observations of active galaxies harboring supermassive black holes (SMBHs) and ejecting relativistic outflows represent a unique tool to probe the physics of extreme environments. are well-known for emitting variable radiation across the entire electromagnetic spectrum, reaching up to multi-TeV energies. These emissions exhibit fluctuations occurring on timescales ranging from several years down to just a few minutes. Currently, AGNs account for roughly 40% of the sources detected at very high energies using ground-based telescopes. The AGN Key Science Project is instrumental in addressing the three primary CTA key science themes listed earlier, offering a wealth of information about the physics of γ-ray-emitting AGNs. This, in turn, has direct implications for our understanding of acceleration and emission processes, the characteristics of relativistic jets, and the accretion regimes at play. In order to successfully implement this observational program both the Northern and Southern arrays are needed, in order to maximize the sam-

ple of accessible sources. Given that part of the program can commence with partially complete arrays, it is strongly recommended to initiate observations as soon as possible. This approach allows for the simultaneous coverage of sources with the Fermi Large Area Telescope (Fermi-LAT) before the conclusion of its mission, maximizing the scientific benefits derived from such observations.

Transient phenomena

The category of sources known as transient collects a diverse population of astrophysical objects, within our Galaxy and beyond. These objects are characterized by sudden and unpredictable explosions or intense bursts of radiation across a wide range of the electromagnetic spectrum. The timescales for these events can vary significantly, ranging from milliseconds to years. Transients hold immense scientific significance, as they are linked to catastrophic events involving relativistic compact objects like Neutron Stars (NSs) and Black Holes (BHs). These objects manifest some of the most extreme physical conditions found in the universe.
This category of sources is of particular interest for this work because the proposed strategy foresees follow-up observations of six classes of targets, triggered by external or internal alerts:

- **Gamma-Ray Bursts:**
  Thanks to its low energy threshold, large effective area and rapid slewing capabilities,CTA will have the capacity to accurately measure the spectra and variability of GRBs up to energies in the TeV range, with unprecedented photon statistics. In addition to addressing key issues regarding the physics of GRBs, which is still poorly understood, CTA will use GRBs as probes of cosmic-ray physics, observational cosmology and fundamental physics [71].
- **Galactic transients:**
  A wide variety of Galactic sources show transient emission at soft and hard X-ray energies. Although most of them can show emission up to MeV and/or GeV energies, many have not yet been detected in the TeV domain by IACTs. Thanks to the great sensitivity to short timescale phenomena and fast repointing capabilities CTA will allow to detect new Transient sources inside our galaxy. Some of the transient sources are already known, such as microquasars, novae, pulsar wind nebulae, transitional millisecond pulsars and magnetars. Nonetheless it can be foreseen that CTA will detect other variable γ-ray sources possibly even of unknown nature. A study of CTA capabilities to detect galactic transients is presented in [80].
- **X-ray, optical and radio transients:**
  A multitude of X-ray, optical, and radio transient events will be newly discovered and monitored by present and upcoming transient survey facilities, that have the capability to regularly survey extensive sky regions in these wavelength bands. By observing a carefully selected sample of such alerts using CTA, new approaches will be developed for understanding well-known types

of transient phenomena. Additionally, this endeavor holds the potential for uncovering entirely novel classes of sources that were previously unknown.

- **High-energy neutrino transients:**
  Cosmic high-energy neutrinos are clear indicators of hadronic cosmic-ray production, thus a coincident emisson of VHE γ-ray signal is expected. The detection of γ-rays linked to a high-energy neutrino event, known as IceCube-170922A [70], and attributed to the Blazar TXS 0506+056, was particularly significant for multi-messenger astronomy. CTA, through follow-up observations of carefully chosen alerts, will play a pivotal role in uncovering potentially new sources of neutrino emissions. It will also contribute to advancing our understanding of the sources responsible for ultra-high-energy cosmic rays, thus facilitating significant breakthroughs in astrophysics and our comprehension of the universe.
- **GW transients:**
  The detection of electromagnetic emissions subsequent to the gravitational wave event GW170817 marked the beginning of the era of multi-messenger astronomy. This event also furnished the first direct confirmation that at least some binary neutron star (BNS) mergers serve as precursors to short GRBs. In the coming years, CTA will play a fundamental role in the follow-up of GWs at VHE, thanks to its unprecedented sensitivity, its rapid slewing capabilities, and its large FoV.
- **Serendipitous VHE transients:**
  Unpredictable by definition, they constitute important exploratory targets whose follow-up prospects depend on the performance of the Real-Time Analysis.

In addition to these targets, an unbiased survey for transients can be performed utilizing divergent pointing observations. This survey, also referred as VHE transient survey, will apply divergent pointing to achieve a large instantaneous FoV. It could offer not only more efficient surveying of the extragalactic sky but also unique prospects for a VHE transient survey not biased by alerts [50].

Extragalactic Survey

This Key Science Project consists of a blind survey of 25% of the total sky. This survey represents a groundbreaking endeavor, as it marks the first time that such a substantial portion of the sky is observed uniformly and with exceptional sensitivity at these high-energy range. The uniqueness of the survey also enables the search for new source classes, as well as the search for large-scale structures in the electron spectrum. Divergent pointing mode will be applied to perform this task in case simulations show that it is more sensitive than normal pointing.

Chapter 3

Alternative Pointing modes

One of the characteristics of CTA, that will make its performance superior to any of the previous IACT systems, is the huge number of highly performing telescopes that will be part of the array. Currently, the array with the greatest number of telescopes is H.E.S.S., with its five members. CTA, even in its smallest configuration - Northern site alpha configuration - will double that number.
One of the advantages of this huge telescope multiplicity is that for the first time it will be possible to apply non-standard pointing strategies. Up to now the pointing mode that as been studied is the full-array, parallel pointing. This means that all the telescopes in the array are pointed together at the same position of the sky. This strategy is of course the most efficient for arrays with a small number of telescopes. Nonetheless, a large number of telescopes allows us to break this scheme. The simplest way is to think about two different strategies, violating one assumption at a time: we can point objects in a non-parallel way (divergent and convergent pointing) or use subgroups of telescopes simultaneously for different tasks (SubArray strategy).
In this chapter I will introduce the divergent pointing and the SubArray strategies, introducing the state-of-art analysis of array performance in these configuration and describing briefly the science tasks that could possibly benefit from those strategies.

3.1 Divergent pointing

Divergent pointing was introduced as a possible pointing strategy to be used by CTA to optimize the IACTs extragalactic survey task by Dubus et al. in 2013 [50]. The underlying idea is to tilt telescopes into the outward direction by an angle increasing with the telescope distance from the array center. This configuration allows to increase the array FoV, thus reducing the time needed to scan large sky regions, like the ones faced when performing surveys or looking for electromagnetic counterparts of Gravitational Wave (GW) events. This enlarged FoV unfortunately comes with drawbacks, namely a reduced sensitivity and worsened energy and angular resolution. The divergent configurations, suitable for the science goals one intends to achieve, can be selected analysing the array behaviour in divergent conditions. The goal is to maximize the size of the FoV

while maintaining a good performance. An important parameter in this kind of study is the average telescope multiplicity - number of telescopes looking at the same part of the sky.

For this purpose MonteCarlo (MC) simulations are performed, with the aim to obtain array response functions (IRFs), which are defined in 4.3 and establish if the performance of the array will be suitable for specific scientific goals.
Some preliminary studies of divergent mode performance were presented in the past few years. In [102] Szanecki et al. analysed the performance of an array of MSTs located at the H.E.S.S. site, at that time one of the candidate sites for the Southern array. The considered pointing modes, illustrated in Figure 3.1, are parallel, divergent and convergent. This study used the first CTA MC simulations [26] (`prod1`) and included 23 telescopes. For each pointing mode the basic parameters used to describe the performance of ground-based γ-ray detectors (e.g. impact parameter, collection area, trigger rates, acceptance, energy and direction reconstruction) are analysed both at trigger (before γ-hadron separation) and analysis (after γ-hadron separation) levels. The convergent mode shows the most accurate energy and angular resolution at high energies, and at low energies its resolutions are similar to other modes. For the energies around 150 GeV it also offers the least biased energy reconstruction. The divergent mode, on the other hand, offers the most efficient detection of sources, but has a rather poor reconstruction performance, especially at high energies. What is suggested by the authors is to consider a mixed mode (e.g. using at the same time the SST subarray in convergent mode and the MST one in divergent) to allow for more accurate spectral and morphological studies of the discovered high-energy sources.

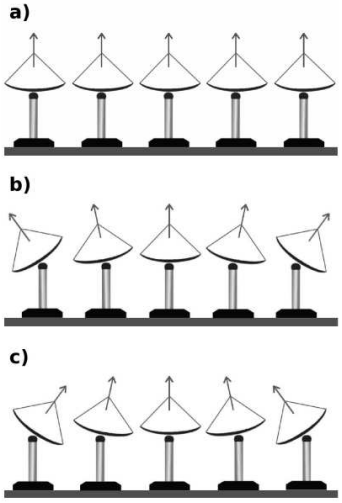

Figure 3.1: Three configuration modes for the telescope system used in the sky-survey scans: a) normal (parallel); b) divergent; c) convergent. From [102]

The same year another study by Gérard was presented [60], analysing the performance of an array constituted of 18 MSTs and 56 SSTs pointed in divergent mode. Once again the MC simulations used were those previously named `prod1` and the site was the Southern one. That study did not consider LSTs; their smaller field of view and the small number of telescopes (two to four) in the array, makes them unsuitable for a divergent pointing mode aiming for a $\sim 20^\circ$ field of view. Its results showed that a homogeneous performance over a 14° field of view can be achieved with the divergent pointing mode; the angular and energy resolutions and the sensitivity at the core energies of the array are $\sim 20\%$ worse than those obtained with a normal pointing mode, and the performance of the divergent mode relative to the parallel mode increases with the number of telescopes

present in the array (see Figure 3.2).
A more recent work [49] analysed the performance of CTAO Northern array for several

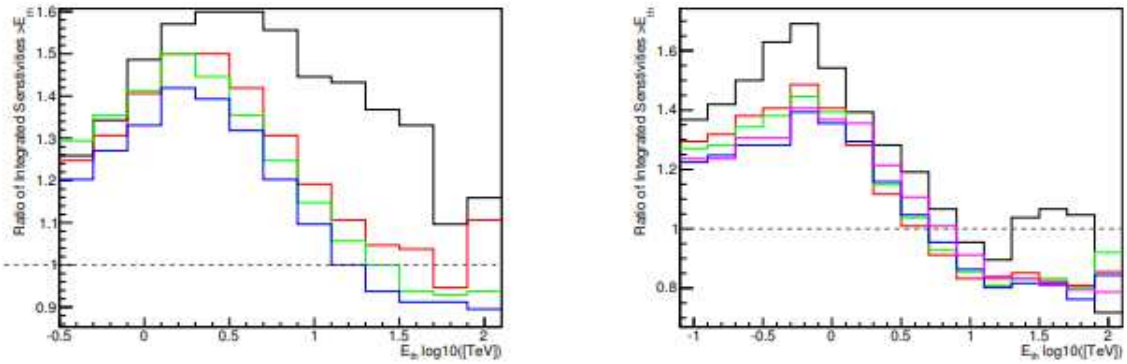

Figure 3.2: Ratio of integrated sensitivities, see [60] for details. **Left**: SST-only arrays, with 16 (black), 24 (red), 40 (green) and 56 (blue) telescopes. **Right**: 18 MSTs array without SSTs (black) and with 16 SSTs (red), 24 SSTs (green), 48 SSTs (blue) and 56 SSTs (pink).

divergent configurations, optimized for the site omega configuration (also referred to as final or full-scope). The MC simulations used for this study are the ones referred to as `prod3b` [29]. These simulations are than analysed with `protopipe`, a python tool based on the `ctapipe` library [74],[78]. This is a python package providing library functions and command-line tools to perform raw data reduction, event cleaning and reconstruction. The advantage of using `ctapipe` based pipelines is that the event reconstruction is performed in a common 3D telescope reference frame in a way that makes it independent of the array pointing strategy applied [59]. This allows to analyse divergent simulations as if they were standard (parallel) data.
Since all the previous works show that the divergent pointing mode is a promising strategy, the analysis of CTA performance under such pointing conditions is still ongoing. In this work updated simulations and performance analysis will be presented for both sites.

3.2 SubArrays

This pointing strategy violates the full-array condition usually applied while keeping the telescope pointing directions consistent to each other (parallel pointing). The reason to introduce such a pointing strategy is that there might be some scientific tasks that do not require the full array sensitivity, e.g. because the sources are bright enough to be seen with a reduced number of telescopes or the source does not emit into the energy range covered by one of the telescope classes. Among standard IRFs provided by CTAO there are already some kind of SubArray IRFs: for each array the response functions for single telescope classes are available. What is still to be done is to determine the performance of SubArrays made of a smaller number of telescopes (e.g. 3 MSTs) and,

at the same time, determine what are the capabilities of the remaining part of the array. Unlike the divergent case, for the analysis of SubArray performance no customized MonteCarlo simulations are needed, one just needs to analyse subsets of telescopes from the full array simulations. What is still needed is a customized performance analysis. This can be performed with the same libraries and pipelines used for divergent pointing.
This pointing strategy was considered before by Dubus et al. [50] to perform surveys in a more efficient way. As for the divergent strategy this analysis has been carried out for `prod1` simulations considering one system of four LSTs, two systems of MSTs (four or nine members) and finally an array of three SSTs.
During one of the periodic meetings this task was illustrated to the CTA scientific groups, namely Galactic, Extragalactic and Transient working groups, all of which have expressed interest in the topic and sent some requests for the telescope numbers/combinations. Following these guidelines several configurations have been taken into account, starting from the ones made up of the same class of telescopes (e.g. subgroups of MSTs) for the Northern site, which will be the first one to be completed. The Southern array and mixed groups (LSTs + MSTs or MSTs + LSTs) will later be considered.
Part of the analysis has been carried on in collaboration with a bachelor student of Trieste University and has been the object of her thesis.

3.3 Science cases

The pointing strategies introduced in the previous section will mainly benefit two research fields of CTAO, namely the extragalactic or all-sky survey and the research of transient sources. As mentioned, both divergent pointing and the SubArray strategy were introduced as possible ways to reduce the time needed to perform surveys with CTA.
Surveys constitute versatile datasets that enable the detection of unexpected sources. Divergent pointing can also be beneficial in the search for GW counterparts and poorly localized Gamma-Ray Bursts (GRBs). The large FoV allows large sky regions to be covered, like the ones associated with these kind of events, with a significantly lower number of pointings with respect to the ones requiring pointing in parallel mode.
Another task that will indirectly benefit from an enlarged FoV is the serendipitous discovery of transients. In order to discover transient sources a large FoV is mandatory, because we have no idea, a priori, of the location or the time when these sources will be visible. This is the reason why Air Shower Arrays are more suitable for such observations. On October 9th 2022 LHAASO showed this efficiency detecting GRB221009A. The source was in the field of view from the trigger time (T_0), but TeV emission began several minutes after T_0. The photons observed by LHAASO are associated with the GRB afterglow; prompt emission remains elusive in the TeV band. Nonetheless, IACTs have better angular resolution and an early detection of transients with Cherenkov telescopes would allow us to determine their properties at VHE with unprecedented detail.

3.3.1 Surveys with CTA

Surveys constitute an unbiased, systematic exploratory approach: they favor discoveries of unknown source classes providing legacy datasets for future reference. Due to the invaluable importance of the data thus obtainable all the current astronomical facilities, at all wavelengths, have or plan to have survey tasks included in their scientific program. This is particularly critical for observational domains that are opening up, such as very high energy γ-rays, with wide scope for surprises. Among CTAO key science projects two survey tasks are included: a Galactic and an Extragalactic survey. While the first task has already been carried on with IACTs - by H.E.S.S. and VERITAS - the latter has never been performed before with this kind of instruments.
Galactic Plane surveys are particularly well-suited for IACTs. This is because they involve a limited sky area to cover and offer the advantages of lower energy thresholds and reduced confusion levels compared to EAS arrays. It's worth noting that more than half of the presently known WHE sources are situated within a few degrees of the Galactic Plane. The density of VHE sources is notably higher in proximity to the Galactic plane, even though there is some bias due to the larger exposure accumulated in this region. With the exception of a few cases like the Galactic Center, γ-ray binaries, and AGNs, VHE Galactic sources tend to be both extended and non-variable.
In 1998 and 1999 the Whipple Observatory 10 m telescope was used to search for diffuse γ-ray emission from the Galactic plane covering the range of $38.5° < l < 41.5°$ and $-2° < b < 2°$, respectively, in Galactic longitude and latitude. Even though the telescope was equipped with a large field of view (4.8 deg) camera, well suited to detect diffuse γ-ray emission, no significant evidence of emission was found [75].
This was followed by surveys conducted by HEGRA, covering a wider range in Galactic longitude and latitude. Both surveys covered a large portion of the Galactic plane, the second one managed to survey one quarter of it ($-2° < l < 85°$) looking for TeV γ-ray emission from point sources and moderately extended sources (diameter $\leq 0.8°$). The region covered included 86 known pulsars (PSR), 63 known SNR and nine GeV sources, representing a significant fraction of the populations known at the beginning of 2000. No evidence for emission of TeV gamma radiation was detected from these or other sources [13] [14].
Only the present (third) generation of telescopes allowed surveys of the Galactic plane in the VHE band with high resolution and good sensitivity to be carried out, leading to the detection of a high number of new sources.
The most comprehensive Galactic plane survey up to now is the one carried out by H.E.S.S. [63]. Being located in the Southern hemisphere it is the most suitable instrument to study the galactic plane. The most recent survey reported by H.E.S.S. was based on data collected during 2004-2013. It covered a wide range in Galactic longitude ($250° < l < 65°$) and latitude ($-3° < b < 3°$) spanning 2700 hours of data. This survey achieved remarkable sensitivity, reaching levels below 1.5% of the Crab flux for point sources. The observational strategy also incorporated high angular resolution, with a mean point spread function of approximately 0.08° or 5 arcminutes (68% containment radius). These characteristics were maintained consistently over the broad energy range

spanning from 0.2 to 100 TeV. In total 78 VHE sources were detected, out of which 31 were identified as pulsar wind nebulae (PWN), SNRs, composite SNRs or γ-ray binaries. Compared to previous IACT arrays, surveys with CTA can benefit from the increased sensitivity (detection of fainter sources), larger field-of-view (to study multiple or extended sources), improved angular resolution (to alleviate source confusion), broader energy range and better energy resolution (to help determination of the source spectral energy distribution). Source confusion represents the biggest challenge in the study of this region, requiring the best angular resolution possible. For this reason divergent pointing is not the optimal strategy for the Galactic plane survey task, nonetheless this task is the best example of the scientific potential of surveys.
Ground-based *gamma*-ray telescopes have successfully detected numerous extragalactic sources, with a predominant focus on AGNs. However, a comprehensive survey of the extragalactic sky has not been conducted with these instruments to date. While AGNs constitute the majority of these detections, VHE *gamma*-rays have also been detected from the afterglow emission of a few GRBs and from a couple of starburst galaxies (SBGs).
Large surveys with IACTs face challenges due to low observation duty cycles (nighttime and moonlight constraints) and limited fields of view (a few degrees). EAS arrays, on the other hand, are better suited for such tasks. However, EAS arrays come with compromises in terms of angular resolution and background rejection capabilities. The lower energy threshold and better properties of IACT data make them invaluable for scientific research. A survey with IACTs has the potential to unveil a significant number of new and potentially unexpected sources in the extragalactic sky, similar to the success of the Galactic survey.
If there is nothing we can do to enhance the duty cycle of IACTs we can still try to enlarge the FoV. For this purpose divergent pointing strategy was introduced. A larger FoV would allow to reduce the time needed to perform this KSP, which is the most demanding, leaving more time to be devoted to other tasks. An estimate of the time required for the Extragalactic survey in divergent mode can be determined once the array's performance is assessed. The possibility that the reduced performance of divergent pointing might not yield a time gain is considered. Nonetheless, even in such a scenario, the observing strategy would still be preferred as it allows for the execution of the "Transient Survey," as described in the following section.

3.3.2 Observing transient sources with CTA

The Universe hosts a diverse population of dynamical astrophysical objects, within our Galaxy and beyond, that explode or flare up in dramatic and unpredictable fashion across the electromagnetic spectrum and over a broad range of timescales. Many of these transient sources are known to be emitters of high-energy γ-rays and are also potential sources of non-photonic signals that include cosmic rays, neutrinos and/or gravitational waves. The great scientific interest in these objects comes from their association with catastrophic events involving relativistic compact objects such as neutron stars and black holes that manifest the most extreme physical conditions in the Universe.

However, the dynamic nature of these transients, which makes them so intriguing, also presents the primary challenge in terms of detailed observational characterization and building a robust physical understanding. One of the major strengths of the CTA lies in its unparalleled sensitivity to very high-energy γ-rays for transient phenomena and short-timescale variability. This capability has the potential to revolutionize our understanding of cosmic transients. Furthermore, CTA's relatively large FoV is a valuable asset for both the discovery of transient events independently and for following up on alerts of transients issued by monitoring instruments As already mentioned, the CTA

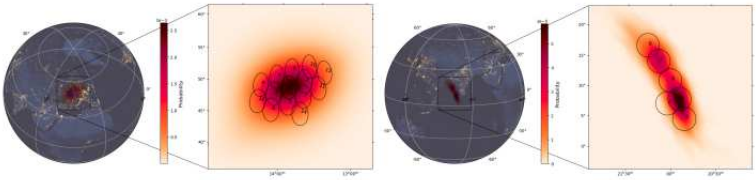

Figure 3.3: Simulated follow-up of the poorly localized GRB alert (left panel) and a GW event (right panel). The strategy applied is described in [40]

Transient program includes follow-up observations of a wide range of multi-wavelength and multi-messenger alerts, ranging from compact galactic binary systems to extragalactic events such as GRBs, core-collapse supernovae and bright AGN flares.
Some of the target sources of the CTA transient program are characterized by poor localization and large error areas. GW events represent the prime example of this condition. The current generation GW detectors allows to reach a sky-localization of the order of 100-1000 deg^2, really large if compared with the typical dimension of current IACTs FoV ($5 - 10\,deg^2$). The same issue can also affect GRBs, sometimes associated with a poor localization, like the ones triggered by the *Fermi* Gamma-ray Burst Monitor (GBM). Optimized pointing strategies have been mainly developed by mid- and small-FoV instruments in the context of GW follow-up campaigns, and actively used in current generation IACTs [21]. Similar studies are carried out for CTA to cover large portions of the localization uncertainty region [92] [25]. However, the rapidly decaying emission transient events makes it difficult to observe them with the relatively narrow FoV of the current and even future generation facilities.
Divergent pointing, with its enlarged FoV, allows these error boxes to be covered with a number of pointings significantly lower than the one needed applying the parallel pointing strategy. This can result in a faster coverage of such sky regions, enhancing the probability to detect rapidly fading sources. Another possibility is to observe these regions with SubArryas, pointing different groups of telescopes, at the same time, to different regions of the sky to scan.
Another advantage of divergent pointing is that it makes possible to realize what is sometimes called a transient survey. This is not a stand-alone project, but a consequence of performing the extragalactic survey in divergent mode. As anticipated, a larger instan-

taneous FoV means a greater probability to detect serendipitous transients inside the observed region. This will hopefully lead to observe for the first time the GRBs prompt phase at VHE.

Chapter 4

Analysis and simulation tools

Cherenkov showers are short ($\sim$ ns), faint, ultraviolet signals triggering the system and recorded by the telescope camera as current inside PMT pixels. The analysis of data collected by Cherenkov telescopes can ideally be split into two macro-sections:

- low level data analysis, that processes data from raw telescope format to lists of reconstructed gamma-ray candidate events, characterized by their arrival direction, energy and probability to be a real gamma-ray and

- high level data analysis, where high level scientific products such as lightcurves, spectra and skymaps, are obtained from event lists.

For a correct reconstruction of the primary particle properties, simulated MonteCarlo (MC) data are needed in order to have an estimate of the instrument's performance. MCs are of fundamental importance in the telescope calibration, since there is no controlled beam of γ-rays to be used as a reference for telescope performance estimates. Since for Cherenkov Telescopes the atmosphere acts as a calorimeter, simulations need to take into account many parameters in order to be as realistic as possible. This requires detailed models of the atmosphere and its interactions with particles hence large computing resources. This chapter will introduce the main tools used by CTAO for MonteCarlo simulations and the analysis of both simulated and real data, together with the definition of standard data levels that will be used as a standard for gamma-ray astronomy.

4.1 Shower simulation: `CORSIKA` and `sim_telarray`

Generating Monte Carlo simulation for IACTs means taking care of two major components: the development of the extensive air showers and emission of Cherenkov light by the shower particles and the detection of this light and signal recording of by the instrument.
For CTAO these steps are performed by two packages called COsmic Ray SImulations for

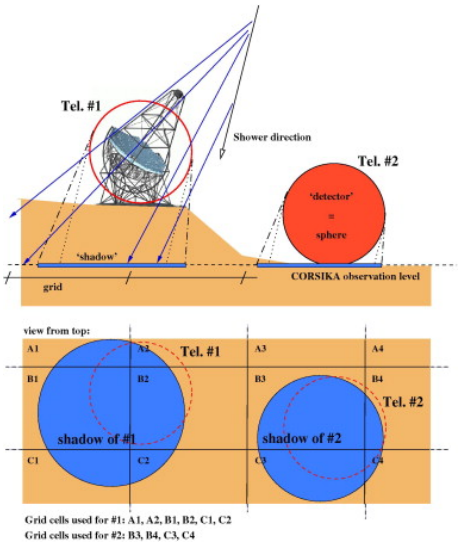

Figure 4.1: Definition of grid cells at the detection level. The shadow of a sphere is large enough to include all Cherenkov light emitted up to 10° from the shower direction and intersecting the sphere. From [28].

KAscade (`CORSIKA`[1]) and `sim_telarray`[2]. `CORSIKA` is a publicly available, open-source code for detailed simulation of extensive air showers initiated by high energy cosmic ray particles. It was originally developed to perform simulations for the KASCADE (KArlsruhe Shower Core and Array DEtector) experiment [48]. It has since than been improved and several instruments, including CTA, adopt it as a standard for simulations.
The original `CORSIKA` Cherenkov option – developed mainly at the University of Madrid – was designed for simulating the HEGRA AIROBICC array of non-imaging detectors. This option required a horizontal plane with a rectangular grid of rectangular detectors. To accommodate more recent non-horizontal detector layouts, the Cherenkov component in CORSIKA has undergone a complete revision. Additionally, a new output interface has been developed and is activated using the IACT option [27].
With this updated IACT/ATMO package, the detector configuration is modeled as a collection of three-dimensional fiducial spheres that contain the reflector or detector [28]. To optimize computational efficiency, an approximation is applied: Cherenkov light emitted within a certain angle (approximately 10 degrees) from the shower axis is assumed to be guaranteed to reach detectors located at the 'detection level', as illustrated in Figure 4.1. Photon bunches are recorded if they pass within a specified radius from a detector (telescope) position. For performance studies gammas, protons and electrons must be simulated. Particles can be simulated as coming from a single point in the sky (point-like) or specifying a cone around the source position within which the particles can come

[1]https://www.iap.kit.edu/corsika/index.php
[2]https://www.mpi-hd.mpg.de/hfm/ bernlohr/sim_telarray/

from (diffuse). The parameter that allows to define a point-like or diffuse simulation is called `VIEWCONE`. Protons and electrons, constituting the background, are always simulated as diffuse components while gamma-rays are simulated both as point-like and diffuse. The former are used only for performance estimation purposes while the latter are also needed to train the models used to estimate energy, incoming direction and probability of the primary being a gamma-ray (the last parameter is called gammaness). The choice between point-like and diffuse gammas depends of the class of gamma-ray sources one needs to analyse.
The volume of simulations needed in order to have a statistically meaningful dataset is quite large and dominated by of proton-induced showers needed for background estimations. For this reason the CTA computing GRID is needed for the massive production of showers and detector simulations: if interested in point-like sources, point-like gamma-rays will be used, while diffuse gammas are used to estimate the array performance when observing diffuse sources.
The simulation of the detector response is performed by the telescope simulation package `sim_telarray`, based on software developed for HEGRA and than adapted to the H.E.S.S. system by making it much more configurable. `sim_telarray` implements all the details of the detector, like the optical-ray tracing of the photons from the mirror to the photomultiplier tubes in the camera, the electronics and the digitization of the signals, as well as the trigger system. `sim_telarray` also allows to account for noise induced by the night-sky background and the electronics. All these features allow to generate a detailed and realistic detector simulation.
Detailed simulation models of the CTA telescopes are included in `sim_telarray` package. These models are periodically updated in order to correctly account for the correct properties of the site (atmospheric transmission, magnetic field), telescope characteristics, expected Night Sky Background (NSB) level per pixel, and trigger thresholds. A crosscheck for the correct implementation of these features can be obtained from the agreement between real data and simulations. One important feature of `sim_telarray` simulations is that each telescope can be configured separately on the command line and via configuration files. This allows to define a different pointing direction for each telescope.
The two packages can be run together or separately according to simulation needs. The advantage of running them separately is that `CORSIKA` simulations can be used multiple times for different array configurations (e.g. different divergent configurations) reducing the computing resources needed.

4.2 Data levels

For CTAO some reference data levels have been defined that indicate the progression of the data along the processing chain.

R0 (raw low-level)
Raw waveform data. The content and format of the data is internal to each device

and will not be written on disk.

R1 (raw common)
Waveform data with calibration applied. The calibration is unique to each camera (camera-wise) and is needed to achieve a common data format between all telescopes. R1 is the first data level that, however, still contains too much data for long-term storage.

DL0 (raw archived)
R1 data with data volume reduction applied (pixels likely containing no Cherenkov signal are removed). These data are the first input for the analysis pipeline.

DL1 (calibrated)
At this step Hillas parameters ([67], see next paragraph) have been computed by the offline data processing pipeline. Information is still telescope-wise.

DL2 (reconstructed)
Shower parameters, including energy, direction, and the nature of the primary particle (gamma or hadron) are computed and stored as an event list. At this stage individual telescope information is not relevant anymore.

DL3 (reduced)
At this level the data is stored as lists of gamma-like events and the corresponding Instrument Response Functions (IRFs). The instrument response includes effective area, point spread function (PSF), energy dispersion and residual hadronic background (reconstructed direction, reconstructed energy, arrival time). From this step on the official tool to handle data is `gammapy`

DL4 (science)
Higher-level science data products. Thanks to the choice of coordinates system, region or energy binning and events are binned into multidimensional data structures (maps) with the selected geometry.

DL5 (high-level)
Modeled and fitted datasets. At this step legacy datasets, such as the CTA survey sky maps or the CTA source catalogue, are generated.

Their definition is essential to ensure compatibility between data coming from different telescopes. The choice to define common data levels, together with the development of open-source science tools is the result of the open observatory nature of next generation telescopes and of an increasing demand for open science. Open community access is a novelty in this domain, challenging the implementation of services that make very high energy gamma-ray astronomy as accessible as any other waveband.

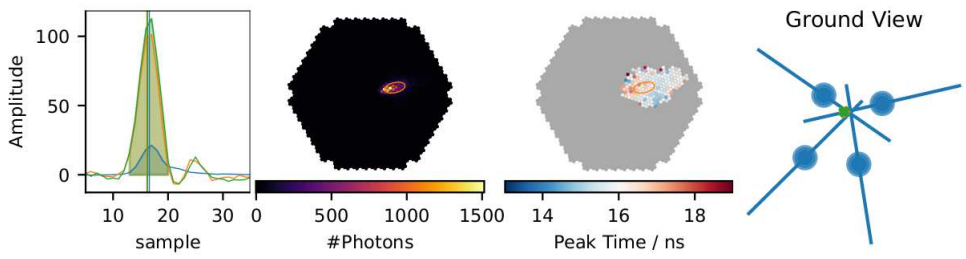

Figure 4.2: Steps of the analysis up to shower geometry reconstruction: 1. The Cherenkov pulses in each pixel are found and integrated (left) to obtain the number of photons (second from left) and peak times (third from left). 2. The resulting image is cleaned, the pixels not selected are shown in gray in the peak time plot. 3. The images are parameterized, including the Hillas parameters which are visualized using an ellipse. 4. The physical properties of the primary are reconstructed. The plot on the right shows the impact point of the primary on the ground. Credits [88].

4.3 Low level data analysis: `ctapipe` and `pyirf`

`ctapipe` is a python package which is being developed for the processing of CTA low-level data, being them either simulated data or real ones, such as those collected by the LST-1 telescope currently under commissioning in La Palma. The software is developed as an open-source project via GitHub since 2015 [74]. `ctapipe` core dependencies are some python scientific libraries such as `astropy` [22] for astronomical computations and unit support, `numpy` [64] and `scipy` [104] for numerical algorithms and statistics and `pytables3` for IO using Hierarchical Data Format, Version 5 (HDF5[3]), which is a general purpose library and file format for storing scientific data.

The signal in the R0 data level comes from the ADC counter and is recorded as a waveform for each gain channel. The reason to have more than one gain channel is to enlarge the dynamic range of the instrument. At DL0 level only one gain channel will be selected for each pixel. As a standard high gain is selected, unless saturated. The amount of useful information, collected across the camera pixels, is arguably a small fraction of the total waveform volume, on average only 3% of the pixels will be kept at DL0 level. A data volume reduction process is needed: pixels most likely containing actual signal are selected, to avoid storing useless data.

The main step in the DL0 to DL1 event processing is the image extraction. Typical extraction techniques involve two stages: peak finding, to identify the most probable position in time for the signal peak, and signal integration, to extract the charge with a window whose width must be appropriate to capture the signal while minimising the amount of noise (e.g. Night Sky Background, electronic noise ...) included. `ctapipe` supports different algorithms to extract these quantities from single-pixel waveforms.

[3]https://www.hdfgroup.org/HDF5/

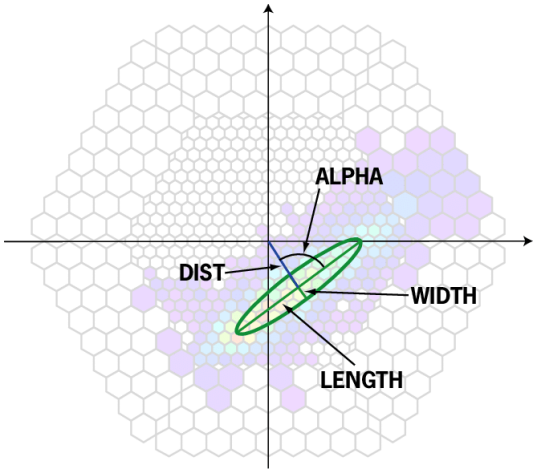

Figure 4.3: Example parameterization of a shower image with Hillas parameters [16].

These range from simple peak finding algorithms to more complex ones which combine the waveforms of multiple pixels or fit the expected time evolution of the shower and use it to define the integration window for each pixel.
The next operation is image cleaning, aimed at identifying pixels which are likely to host real Cherenkov signal. This is usually done by applying a pixel-wise selection via cleaning thresholds based on the charge and peak time values, output by the image extraction step. What is typically done is to establish a double charge threshold condition, where a higher value is required for core pixels and a lower one for neighbour ones. If a cluster of pixels satisfies the charge threshold condition and the difference in their arrival times fall below a certain time threshold, those pixels are associated to a real shower and are selected. Again, multiple algorithms to solve this task are supported in `ctapipe`.
After pixels with real signal have been selected, the resulting image for a γ-ray primary particle is essentially an ellipse, whose moments can be computed using the charge of each pixel as a weight. This step is called Hillas parameterization [67] of the shower image and is essential in order to obtain information that is exploitable by subsequent algorithms. For this task `ctapipe` implements general descriptive statistics of the images, morphological features like the number of isolated pixel groups and parameters describing the containment of the shower's image in each camera.
All the steps described before are performed on each camera separately (monoscopic). In order to perform the reconstruction of event properties, or generate DL2 data, information from all telescopes need to be combined to give one common estimate for a recorded shower (stereoscopic) parameters. Given the positions of the telescopes on the ground and the Hillas parameters of the ellipse in the camera, a stereo reconstruction can be performed for each event in order to find the impact point of the shower on the ground, the incoming direction of the source in the sky and the height of the shower maximum h_{max}.

The final product of the MC analysis chain are the Instrument Response Functions,

which are fundamental to transform the list of event reconstructed properties to physical properties of γ-ray sources and to estimate the array performance under the simulated conditions. The instrumental response of a γ-ray telescope strongly depends on the observing conditions and user-defined analysis parameters, which might be optimized for different science cases. In mathematical terms the IRF is the function that allows to link true properties of the gamma-rays (right ascension, α, and declination, δ, of the gamma-ray source and its total energy E) into the observed/reconstructed quantities (α', δ' and E'). In the classical IACT analysis, it is assumed to be the product of three independent components:

$$IRF(\alpha', \delta', E', t|\alpha, \delta, E, t) = A_{eff}(\alpha, \delta, E, t) \cdot PSF(\alpha', \delta'|\alpha, \delta, E, t) \cdot E_{disp}(E'|\alpha, \delta, E, t)$$

where A_{eff} is the effective area, i.e. the detection probability times the observed area for a gamma-ray with given true properties, PSF is the point spread function, and E_{disp} is the energy dispersion, i.e. the migration between the true energy E and reconstructed energy E'.
IRFs can be computed from labeled, reconstructed event lists thanks to a python library called `pyirf`, which supports calculating most IRFs formats defined in Gamma-Astro-Data-Formats (GADF, [47]) and can export these into the FITS-based data format. Additionally, `pyirf` contains functionality to calculate flux sensitivity of γ-ray instruments according to the CTA requirements and the optimization of event selection criteria to obtain the best flux sensitivity. The package is being developed and tested by members of the CTA consortium.

4.4 High level data analysis: `gammapy`

`gammapy` [45] is an open-source Python package for high level analysis of γ-ray astronomy data. Similar to `ctapipe` it is built on `numpy`, `scipy` and `astropy`. It is used as core library for the Science Analysis tools of CTA, recommended by the H.E.S.S. collaboration to be used for Science publications, and is already widely used in the analysis of existing γ-ray instruments, such as MAGIC, VERITAS and HAWC.
The design of the data work flow, illustrated in Figure 4.4 consists of two steps:

- Data reduction: IRFs and data event lists are selected and reduced into data cubes according to the details defined by the user.
- Modeling and fitting: the user can associate a source model to the dataset and give the best estimate of the model parameters, computed through a Poissonian maximum likelihood fitting on the data

In November 2022 the `gammapy` team released the first Long-Term Stable version, v1.0, that offers a maintained and stable package for scientific analyses. Among the updates included in this version a support for energy dependent temporal models is introduced for the simulation (allowing to simulate e.g. GRBs or AGN flares). In 2021 `gammapy` has bee selected as the core library of the open Science Analysis Tool of CTAO [43].

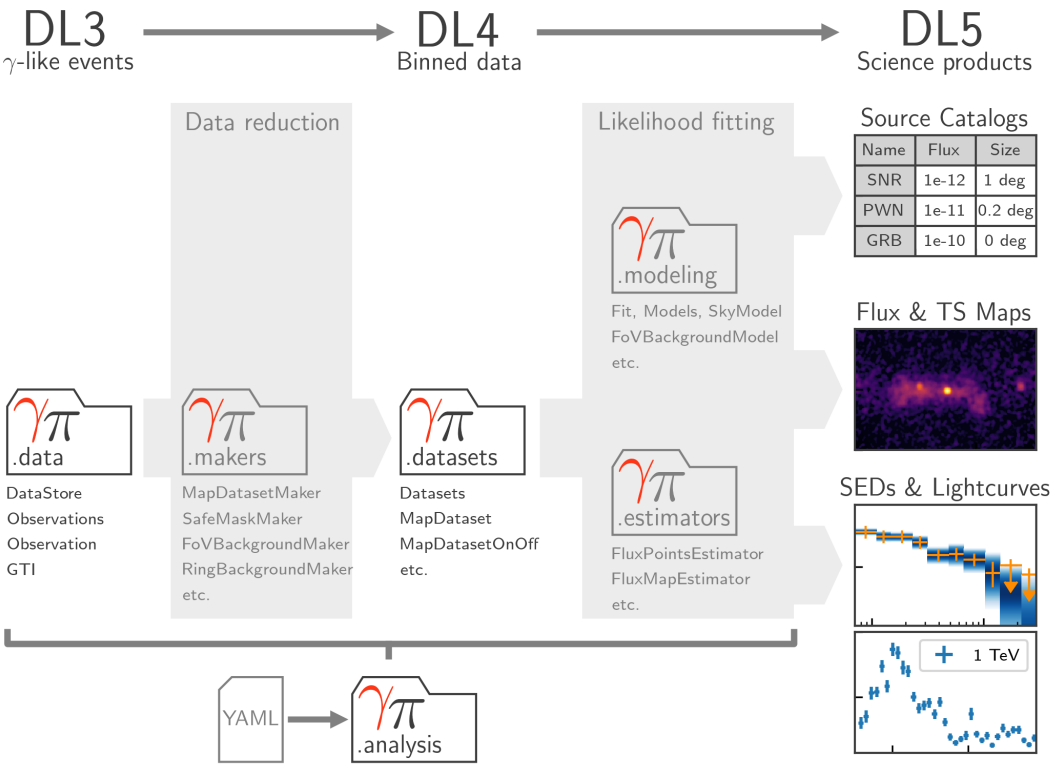

Figure 4.4: Standard analysis flow and the corresponding sub-package structure of `gammapy`. From `gammapy` documentation (https://docs.gammapy.org/1.1/user-guide/).

In this context science tools features and the functionalities needed for some CTAO operations, such as the real time analysis pipeline, are implemented. Being CTAO an open observatory, there is an ongoing project, an open Science Data Challenge (SDC), aimed at preparing the community to use the future data for scientific purposes. Among the objectives of the SDC there is the will to test some CTAO tools (documentation, data dissemination tools, software distribution), to train the CTA consortium and the wider scientific community to use the tool to analyse data, and to explore the CTAO expected performances. A strong feature of `gammapy` is the usage of the common data format `gamma-astro-data-format` (GADF) [46], which permits multi-instrument analyses by supporting joint fit of their data. As the GADF initiative has ended, an evolution in the high-level data format is expected. Recently eleven γ-ray and neutrino experiments have created a new initiative, called Very-high-energy Open Data Format (VODF) [72], aiming to create new standards for VHE astrophysics detectors that respect the FAIR principles [107] and follow as much as possible the International Virtual Observatory Alliance (IVOA)[4] standards. In this context, the internal data model of `gammapy` is being

[4]https://www.ivoa.net/

separated from the read data model with the use of an I/O layer dealing with formats and their versions. The `gammapy` team is continuing to improve the open package by offering even more functionalities.

4.5 Divergent method

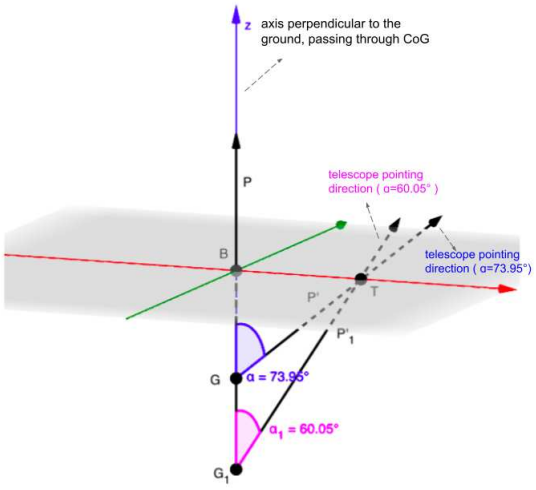

Figure 4.5: Concept used to define the divergent pointing from a parallel one for a telescope. **B** represents the ground position of the array CoG, **T** is the telescope ground position. **G** and **G'** represent the ground point for different divergent configuration. This point is defined in order to control the single telescope pointing direction defined by the lines **P** and **P'**. Adapted from [49].

The key of divergent pointing is to define the pointing direction of each telescope in the simplest way possible. This can be easily done thanks to an algorithm, called "umbrella mode", introduced in order to reduce the number of hyper-parameters needed to describe the system. In Figure 4.5 a simplified scheme is shown, reporting the geometry used to define telescope pointing directions. The current version of the code draws an imaginary line aligned with the telescope pointing direction and connecting each telescope ground position to an axis, perpendicular to the ground, passing through the Center of Gravity (CoG) of the array, labeled with z. These lines are defined so as to meet all in the same point, called ground point, whose position along the z axis determines the pointing direction of single telescopes. To avoid introducing as many variables as the number of telescopes.
Consider for simplicity the CoG, called **B** in the picture, to be located at the origin of a 3D reference system. In the same system **T** represents the position on the ground of one of the telescopes of our array, and we assume it to be at a distance of 1 m from **B**.

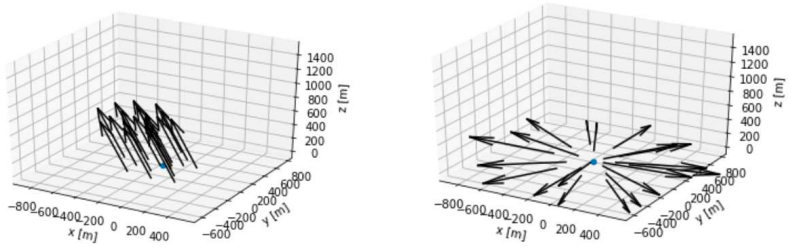

Figure 4.6: Sketch of the array pointing directions for div=0.0 (left) and div=1.0 (right) [49]

The ground point, **G**, can be defined on the z axis, such that the line passing through **G** and **T** forms an angle α with the telescope pointing direction **P**.
Therefore, the distance between **G** and the CoG, is given by

$$|\overrightarrow{GB}| = norm = \frac{1}{\tan(\arcsin(div))} \tag{4.1}$$

This number varies between 1 ($\alpha = 0°$) and 0 ($\alpha = 90°$).
When extending this toy model to the whole array a scale factor f must be introduced, in order to account for the different distances of the telescopes form the system CoG. The generalization of equation (4.1) is:

$$norm = \frac{f}{\tan(\arcsin(div))} \tag{4.2}$$

where, as mentioned, f is the scale factor, defined as the telescope distance from the center at which $div = \alpha/90°$. Each value of div allows to define a value for norm, which sets the position **G**. Thus with a single parameter the pointing of the whole array is defined.
The umbrella mode is implemented into a code available under the CTA-observatory GitHub repository [105][5]. This code takes as an input the list of telescope positions, camera radius and focal length ad defines an Array class which has, among others, a div property that computes, thanks to this umbrella algorithm the pointing direction of each telescope for a given source position. The repository contains the core code of the divergent pointing toy model together with some jupyter notebooks showing how the code works and how to display the system hyper FoV (hFoV) and the average telescope multiplicity.

[5]https://cta-observatory.github.io/divtel/. The latest version of the codeis hosted under irene_tests branch and will be merged to the main after some more checks.

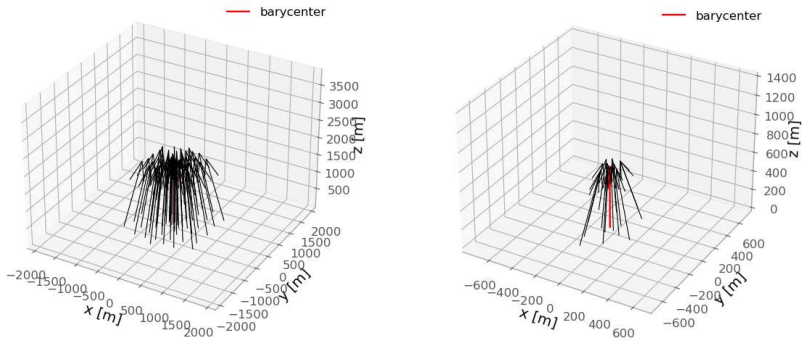

Figure 4.7: Sketch of the Southern array pointing directions for div=-0.02 (left image) and Northern array for div=-0.1 (right image). A negative divergence means a convergent array.

The `divtel` library was used in [49] to select five configurations that enlarged the hFoV of site North Baseline array of a factor 1.5,2,3,4 and 5 respectively. These hFoV values are purely geometric, trigger rates are not taken into account at this level. Even though convergent mode has not been studied in this work, the `divtel` code can be also used to analyse the FoV properties of convergent arrays.

Chapter 5

Array performance in divergent mode

In this section the study on the performance of CTA Southern array is presented. For the first time the site taken into account is the final one for CTA-South and the simulations are based on an updated version of `prod5`. Unlike site North, which was simulated in baseline configuration, we considered the array alpha configuration to which four LST telescopes are added. In this section simulation details will be introduced, together with details on the analysis and the results obtained.

5.1 Simulation details

The first steps to take when simulating the response of a IACTs array is to define the its configuration - number of telescopes and their position on the ground, telescope camera details and telescope pointing directions. Parallel pointing simulations are easier from this point of view: one can simulate the full array configuration, including different positions or different cameras for the same telescope and postpone the choice of the array configuration to the analysis step. This cannot be done when producing simulations for divergent pointing since single telescope pointing directions depend on the position of the array Center of Gravity (CoG), which changes with the specific array configuration taken into account. Nonetheless, for CTAO Southern site, where the telescope positions are more symmetric, some freedom is allowed. One can have small differences in the CoG position if telescopes are added/removed in asymmetric way allowing to simulate a larger number of telescopes with respect to the ones that will actually be analysed.
The array simulated for this study is made up of 87 telescopes, of which a subarray of 60 is taken into account for the analysis: 4 LSTs, 14 MSTs and 42 SSTs whose positions are showed in Figure 5.1. This configuration is close to the so called alpha configuration, with the difference that four LSTs have been added. This is a debatable choice because it allows to lower the energy threshold of the system but having just four LSTs in the array center brings some non-uniformity of the array response across the hFoV. The two arrays, simulated and analysed, being constituted by a different number of telescopes

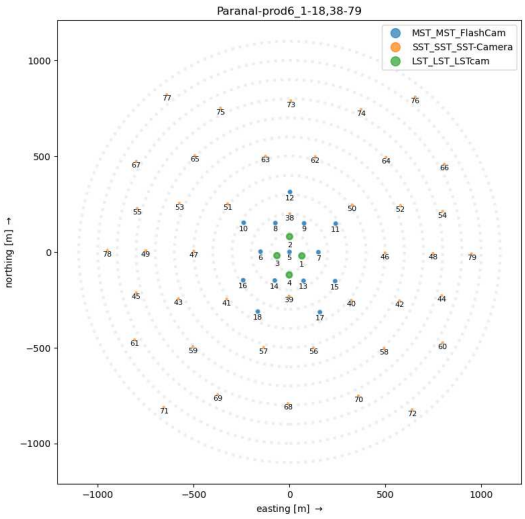

Figure 5.1: Paranal ground position of the telescope subarray taken into account for divergent pointing analysis.

have different CoG positions but the difference is of just 6 m and can thus be neglected. While `CORSIKA` configuration files are the same used for parallel pointing, a custom `sim_telarray` configuration is needed, listing single telescope pointing directions. Both signal (γ) and background files (protons and electrons) are simulated. Since large statistics is needed for the results to be reliable simulations are run on the CTA computing GRID. The energy ranges between 0.003 e 330 TeV for γs and electrons and from 0.004 and 600 TeV for protons. For diffuse simulations a `VIEWCONE` equal to 10 is set.
The `sim_telarray` configuration files can be generated thanks to the `divtel` code. The structure of the divergent algorithm, that computes the pointing directions, is described in the following section. For the first time FlashCam only is simulated for MSTs. This choice helped to boost the proper implementation of FlashCam cleaning and reconstruction in `ctapipe`.
Once the telescopes are selected, pointing directions need to be defined. The pointing direction of the array center, around which the array is diverged (see next section for more details) is located at low zenith, zd=20°, and azimuth 0° (North pointing). The div values implied for this simulation are the same that were selected for site North. Thanks to the `divtel` library the hFoV area and average multiplicity are computed for five configurations. The values obtained are reported in table 5.1. The table reports not only the total area of the hFoV but also the one covered by at least three telescopes (hFoV_{eff}). This is value purely geometric, it represents the region of the sky where the geometrical hFoV of at least three telescopes overlaps. At this level no trigger information are taken into account.

Cfg name	div	hFoV (deg^2)	hFoV$_{eff}$ (deg^2)	m$_{ave}$
parallel	0.0	62.3	62.3	53.4
cfg1.5	0.0022	99.0	89.6	33.5
cfg2	0.0043	141.5	118.3	23.5
cfg3	0.008	232.1	174.7	14.3
cfg4	0.01135	331.2	230.1	10.0
cfg5	0.01453	439.3	285.5	7.6

Table 5.1: Hyper FoV and average multiplicity of the divergent configurations simulated for site south. The first line reports the corresponding values for parallel pointing, as a reference. hFoV$_{eff}$ is the area of the hFoV covered by at least three telescopes.

The area of the hFoV, its shape and average multiplicity cahnge with zenith and the values reported in table 5.1 refer to the array pointing at 20deg in zenith. In Figure 5.2 the hFoV is reported for three of the configurations when pointing at zenith values 20, 30 and 50. As observed in from table 5.1 , the minimum value of multiplicity obtained is greater than 3. This value is employed as a threshold triggering condition: if three or more telescopes trigger the same event, it can be labeled as a detected signal. Keeping this criterion in mind, further analysis may explore additional divergent configurations, setting the limit to the divergence value that yields m_{ave}=3. Given that lower values of altitude correspond to lower values of multiplicity, this threshold should be assessed across various altitude values before determining new configurations.

5.2 Analysis

Data analysis was carried on using a newly developed pipeline entirely based on `ctapipe`. Unlike `protopipe` the new pipeline allows to obtain IRFs for both point-like and diffuse simulations. FlashCam cleaning and reconstruction is introduced and the production of gammaness and energy estimation models is improved.
In order to perform the analysis particle files are split in subgroups:

- 25% of diffuse γs will be used to train the energy model
- another 25% of diffuse γs and 25% of protons are used to train the classification model
- the remaining part of protons and all of the electrons will constitute the background in building the DL2 files. For the signal one can use either the remaining part of the diffuse γs or the point-like γs, according to the kind of analysis needed

Once the files are split they will be transformed from DL0 to DL2. The training datasets are used to train random forests for energy and gammaness estimation and the models are applied to the test datasets. These steps are performed on the CTA analysis grid, only the final DL2 files are downloaded locally and used to estimate the performance.

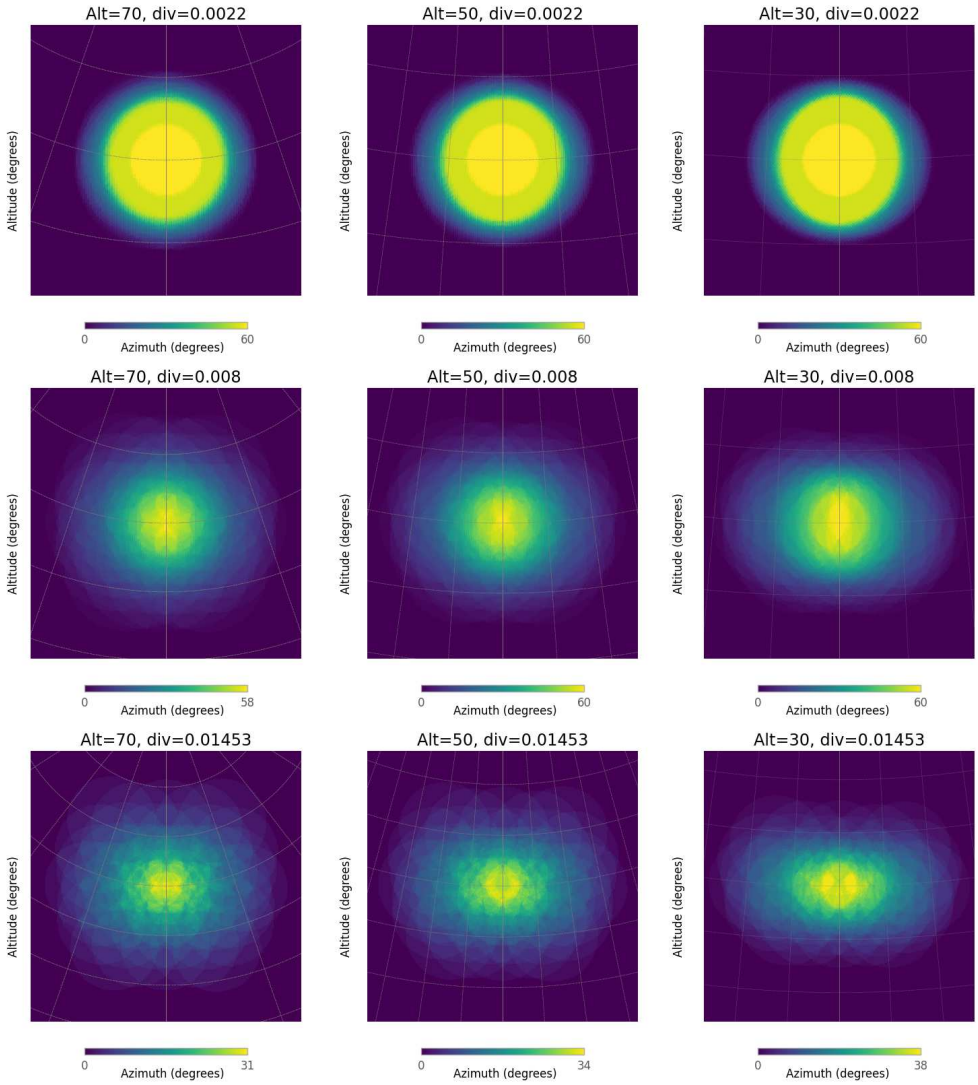

Figure 5.2: Representation of the array hFoV for three values of divergence when pointing at decreasing altitude values. The azimuth is fixed for all configurations at zero. The shape of the hFoV looses circular symmetry when moving from the zenith to the horizon and the effect is more severe for higher divergence values.

Performance plots comprise energy dispersion, angular resolution, energy bias and resolution, and PSF. For point-like performance the procedure is quite straightforward, the IRF can be obtained using the same code applied for parallel pointing. For diffuse performance the situation is more tricky. The code that allows to obtain the IRF for parallel pointing assumes a radial symmetry of the PSF around the hFoV. This condition can't be simply assumed to be true for divergent pointing but some checks must be done. The DL2 output files are produced in HDF5 format, already described in 4.2. The script used to turn h5 format DL2 data into IRFs is available, in a slightly different form in the `pyirf` directory. The original version takes as an input fits files instead of HDF5 ones. The version of `pyirf` used is not the latest (currently v0.10.1), since the branch used is called `faster_optimize_cuts` and relies on an older version of the main branch (v0.7.1dev). From IRF files performance plots can be obtained.
In the following sections I will reported the results obtained for cfg3. The plots for the remaining configurations are shown in AppendixC.

5.2.1 Point-like performance

Concerning point-like γ-rays a preliminary analysis was performed earlier this year using the old `protopipe` pipeline. This analysis underlined some of the criticality of this pipeline, that once reported to the analysis and simulation group, led to the already mentioned change in the pipeline. Specifically `protopipe` used a wrong strategy to generate the models for particle classification and energy regression. Since point-like γ-ray simulations were used to train these models the particle classification resulted unrealistically good. The new pipeline allows to use the correct strategy: the algorithm is trained with diffuse simulations ad than used on point-like ones. This leads to a more realistic result. The γ-hadron cut values obtained with both strategies are reported in Figure 5.3. The first plot corresponds to `protopipe` results, and shows values really close to unity. The same analysis showed a criticality in the angular resolution, defined as the minimum angle at which the array can resolve two separate sources. Since FlashCam cleaning was not correctly implemented in the old pipeline, the first results obtained (left picture in Figure 5.4) showed an angular resolution completely inconsistent with CTA requirements. The latest version of `ctapipe` FlashCam cleaning is correctly implemented, giving way better results for angular resolution (right plot in Figure 5.4) and confirming the hypothesis made to explain `protopipe` results. Nonetheless a worsening in the angular resolution can be noticed at higher energies. This is most likely related to a too high degree of divergence of the SST telescopes. A possible solution, already proposed in [102], could be to consider a pointing configuration with divergent MSTs (and LSTs) and convergent SSTs. This condition can be fixed either introducing different values of divergence for some sub-grups of telescopes, e.g. making the outer telescopes less divergent or even convergent. Another possibility is to change the way single telescope pointings are defined, as introduced in Section **??**.
Energy dispersion and energy resolution and bias, shown in Figure 5.5, provide an estimate of the goodness of the energy reconstruction capabilities of the system. Energy dispersion is the ratio of the reconstructed energy over the true energy as a func-

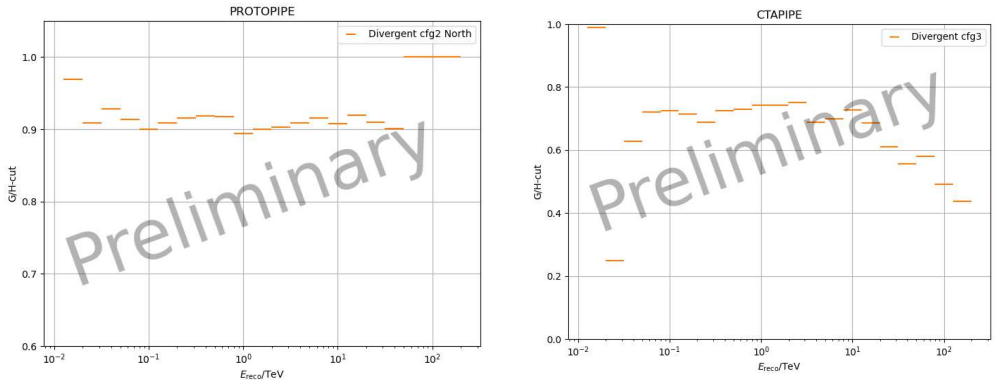

Figure 5.3: Gammaness cut obtained with `protopipe` for cfg2 at Northern site (**left**) and gammaness cut for Southern site cfg3 obtained with `ctapipe` (**right**). The results obtained using `protopipe` are unrealistically good due to the wrong model training strategy applied.

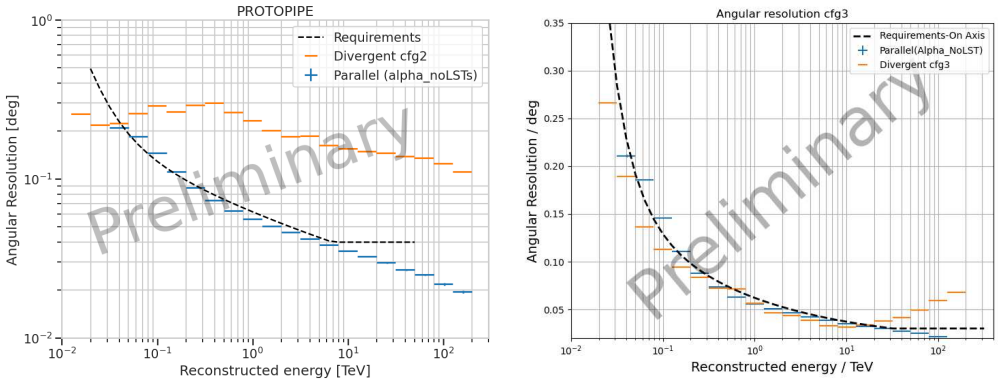

Figure 5.4: **Left**: angular resolution obtained with `protopipe` for cfg2 (Paranal). **Right**: angular resolution for cfg3 (Paranal) obtained with `ctapipe`.

tion of the true energy. Energy resolution is defined as the value of the quantity $|E_R - E_T|/E_T = |\Delta E|/E_T$ within which 68% of the reconstructed gamma-ray events are contained, with E_T the true energy and E_R the reconstructed energy. Energy bias is computed as the median of $|\Delta E|/E_T$ and gives a measure of how much the computed values differ from the median. Both resolution and bias are computed as a function of the true energy. The array effective area is defined as the ratio of reconstructed γ-rays (after event selection cuts) over the number of simulated ones, multiplied by the area (orthogonal to the incident direction) over which events have been simulated. It is computed as a function of the true energy. The behaviour of the array effective area in divergent mode, shown in Figure 5.6 left, seems to be consistent with the parallel

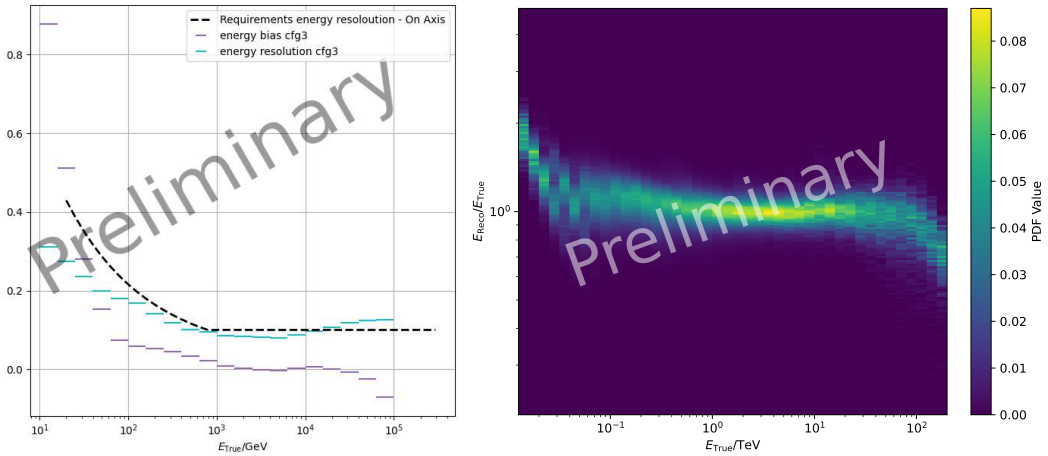

Figure 5.5: **Left**: Energy bias and resolution for cfg3. The requirements refer to energy resolution only. **Right**: Energy dispersion relation for divergent pointing configuration cfg3.

configuration. All the quality cuts are applied in the computation and this implicates a decrease in the effective area, especially for low and high energies. At low energies, this could be due to the cut on image Size, while for high energies the number of events passing the cuts is limited mostly by the leakage cut as the shower images are often not fully contained within the camera FoV.

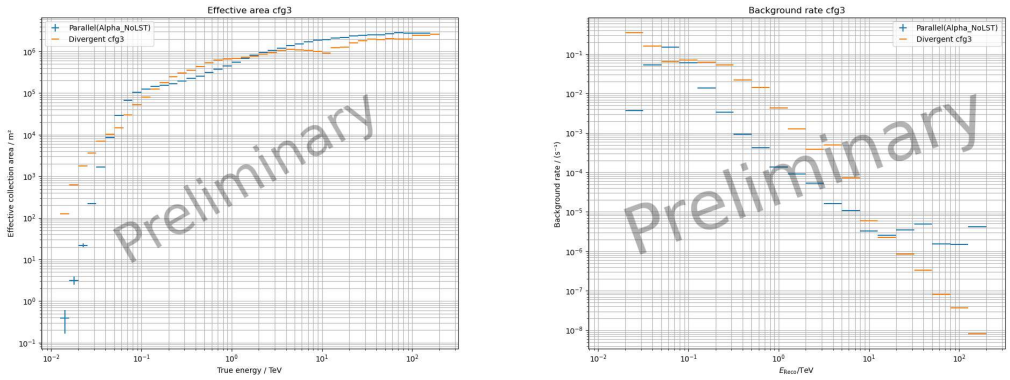

Figure 5.6: **Left**: Effective area for divergent pointing configuration cfg3. The comparison is made with CTA requirements and with parallel pointing Southern array in the alpha configuration. **Right**: Background rate for divergent pointing configuration cfg3.

The sensitivity of Cherenkov telescopes is defined as the minimum flux detectable with n sigma significance in a certain time. As a standard n = 5 is used. The sensitivity is calculated according to the Li&Ma likelihood ratio test [76]. Figure 5.7 shows the

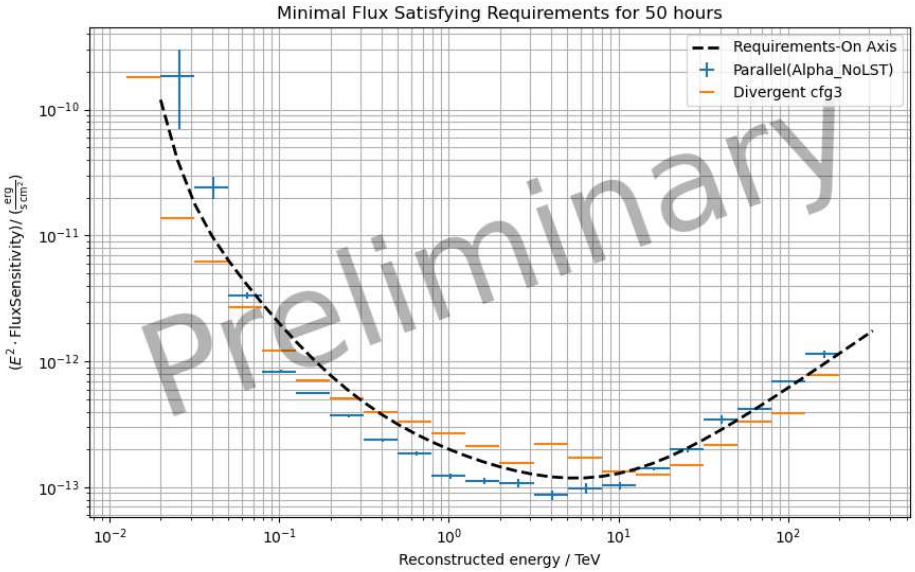

Figure 5.7: Sensitivity to an on-axis point-like γ-ray source for divergent pointing cfg3.

sensitivity for the considered configuration, compared with CTA requirements. As a reference, on the same plot, the sensitivity of parallel pointing for Paranal site is reported. This is the public `prod5` sensitivity for alpha configuration. This does not include LSTs. For this reason divergent pointing shows a better sensitivity with respect to parallel one at low energy. Moreover the parallel simulations are performed using NectarCam for MSTs and are analysed with an older version of `ctapipe`. For a fair comparison the same camera (FlashCam) and software version should be used, this analysis is currently running. The sensitivity shown is in good agreement with the requirements. As mentioned this is expected since the source is located in the central region of the hFoV, where the telescope multiplicity is higher and all telescope classes are observing. The right plot in Figure 5.6 shows the background rate, calculated as the number of background-like events per second, reconstructed energy and solid angle after selection cuts. The plot shows a level of background shown for divergent pointing simulations is inconsistent with the behaviour shown by parallel simulations. This condition is currently under investigation. In AppendixC the same plots for all of the other configurations are reported. The trends are the same observed for cfg3 reported here. The worsening in the performance with growing value of divergence that can be expected is not observed for point-like on-axis simulations. The reason is, as stated before, that the central region of the hFoV shows the larger coverage in terms of telescopes and the lower divergence of the single-telescope pointing direction. This condition ensures the best reconstruction capabilities from the system. The same is of course not true when the source is located in the external parts of the hFoV, which might even not be covered by the LSTs.

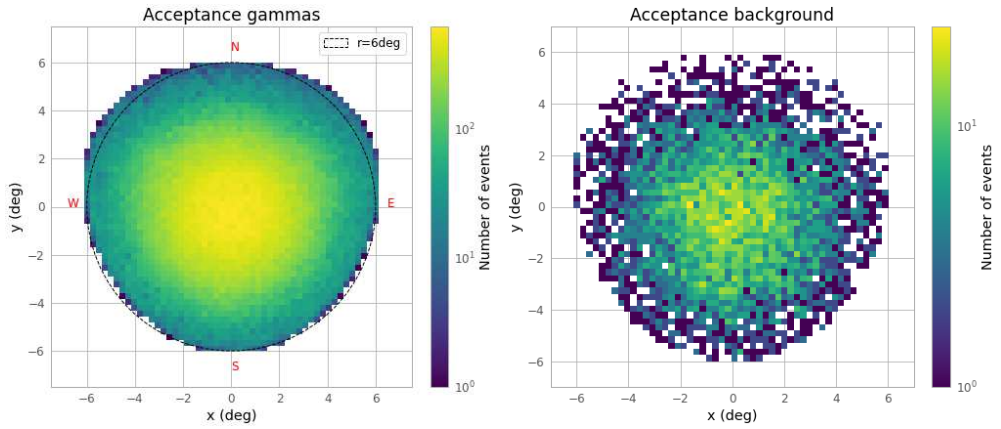

Figure 5.8: Acceptance maps of γs (left) and background (right) for divergent cfg3. The acceptance is computed up to a distance of 6deg from the center of the hFoV, distance which is marked with a circle in the γ-rays' plot. The same plot also reports four letters marking the directions along which the symmetry of the hFoV is checked.

The performance thus obtained is promising but presents a limitation. Due to the huge time and space required for the simulations only an 'on-axis' source has been considered. For such a source the performance is expected to be good, since the central region of the hFoV is covered by at least LSTs and MSTs with the highest multiplicity, allowing the best reconstruction capabilities, both in energy and position. In the future it will be needed to test the performance of this pointing strategy towards off-axis sources. This requires a large simulation campaign, which is not affordable at the moment. A solution to this problem would be to find a way to estimate the array performance skipping the `CORSIKA/sim_telarray` step, e.g. through Neural Network algorithms.

5.2.2 Diffuse performance

Before proceeding with the estimation of the array performance, it is necessary to conduct symmetry tests. Energy reconstruction, PSF and acceptance are plot with growing distance from the center of the hFoV along different directions. These directions, labeled N, S, E and W are shown in the acceptance plot of each configuration. Acceptance for γ-rays and background is shown in Figure 5.8. A circle with 6 deg radius is plot as a reference. The plots are symmetric, and look the same as for parallel pointing. Figure 5.14, at the end of this section, shows the energy dispersion evolution, along the aforementioned directions. Each line represents one of the directions, while each column is a different distance from the hFoV. The plot shows a symmetric situation in terms of energy dispersion. Less symmetry can be detected in PSF from Figure 5.15, which shows the evolution of the PSF with distance from the center of the hFoV along the four directions. Despite PSF, the behaviour is considered symmetric and IRFs are obtained with the same script used for the parallel production. The results obtained using these scripts are reported in the rest of this section.

The energy dispersion, obtained assuming circular symmetry is shown in 5.11. This time a finer grid in angular distance from the center of hFoV is used. An increase in the energy lower threshold is observed for growing distance from the center. The energy bias ad resolution are also plot for the same hFoV bins, see Figure 5.10. Angular resolution at different distances from the center of the hFoV is shown in Figure 5.9. We could recognize a worsening in the angular resolution with increasing distance from the center of the hFoV, especially at energies around 1 TeV. Sensitivity in the different energy bins is reported in Figure 5.12. This worsening might be even more severe in the outer parts, the ones currently not analysed. The background rate per hFoV bin is also shown in Figure 5.13. The first bin shows the same behaviour observed for point-like simulations, while the others are more consistent with parallel pointing results. Both for this plot and the sensitivity one the comparison with parallel pointing is not fair, since the results taken into account are not referred to a specific bin in hFoV distance but are unique.
All of the IRFs obtained using this method are gammapy readable and can be used to simulate source observation in divergent mode. At the moment only software validation tests have been performed, more detailed checks on the obtained performance are needed before proceeding.

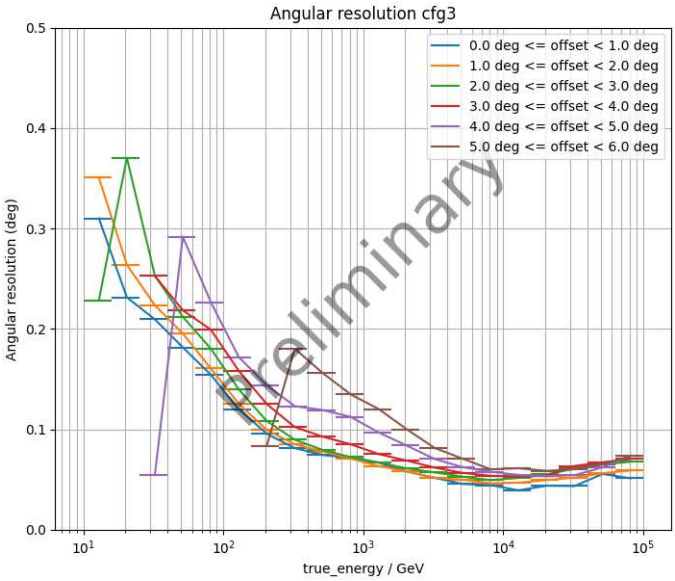

Figure 5.9: Angular resolution at different distances from the center of the hFoV for divergent pointing configuration cfg3.

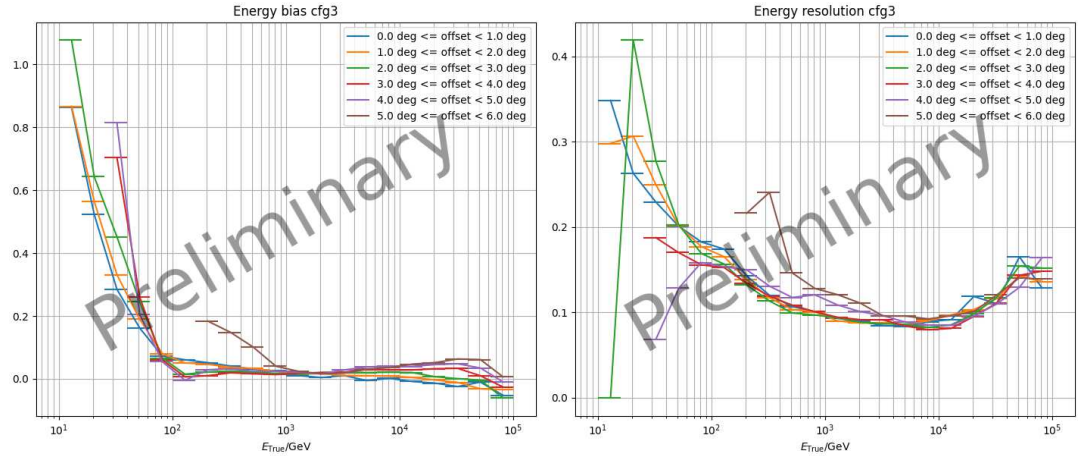

Figure 5.10: Energy bias (**left**) and resolution (**right**) for cfg3 at different distances from hFoV center.

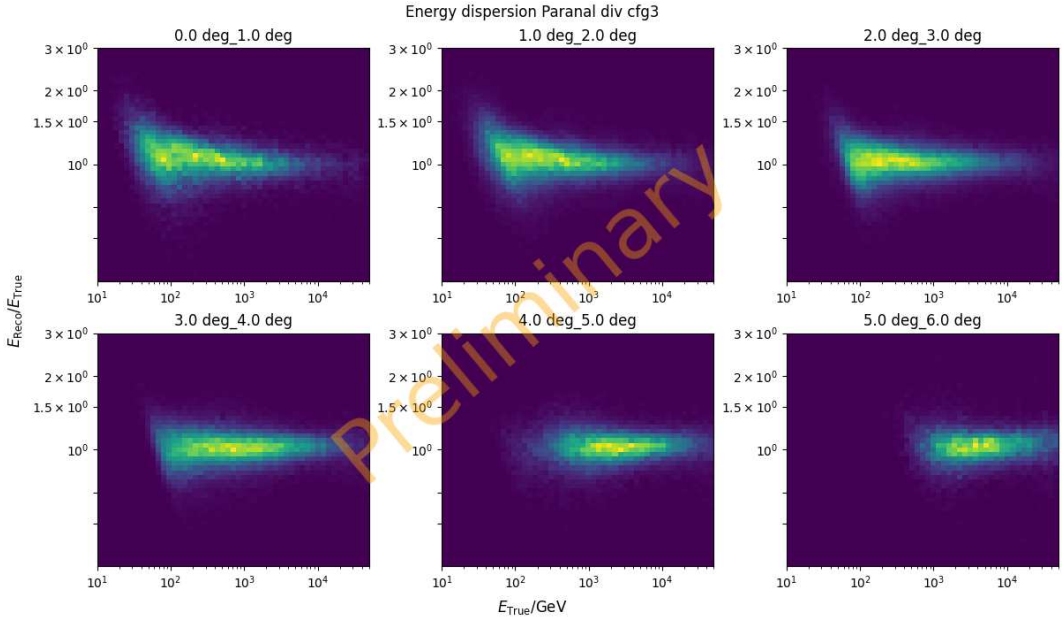

Figure 5.11: Energy dispersion for cfg3 at different distances from hFoV center.

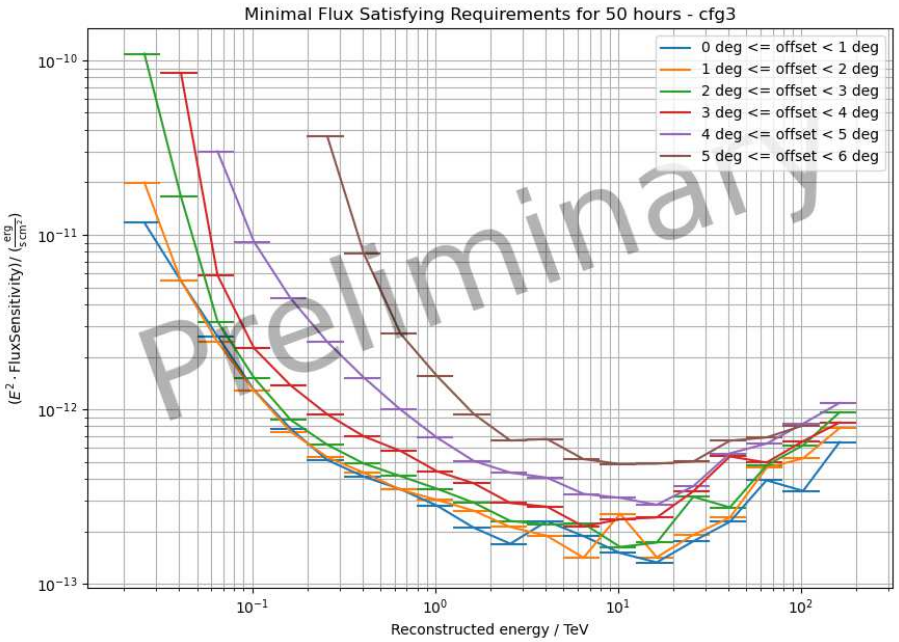

Figure 5.12: Sensitivity curves for cfg3 in different bins of distance from the center of the hFoV.

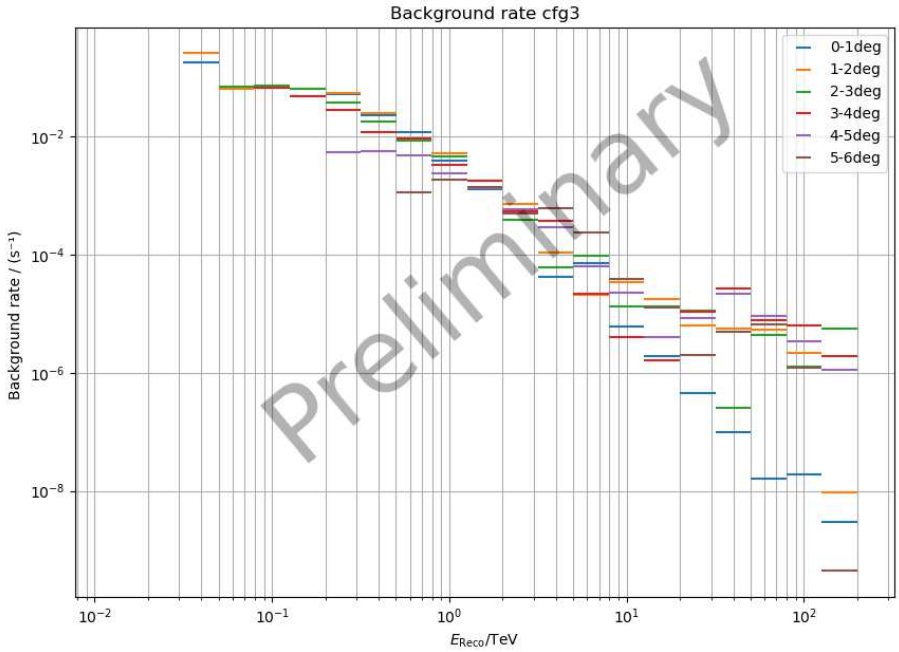

Figure 5.13: Background rate for cfg3 computed in different distance bins form the center of the hFoV.

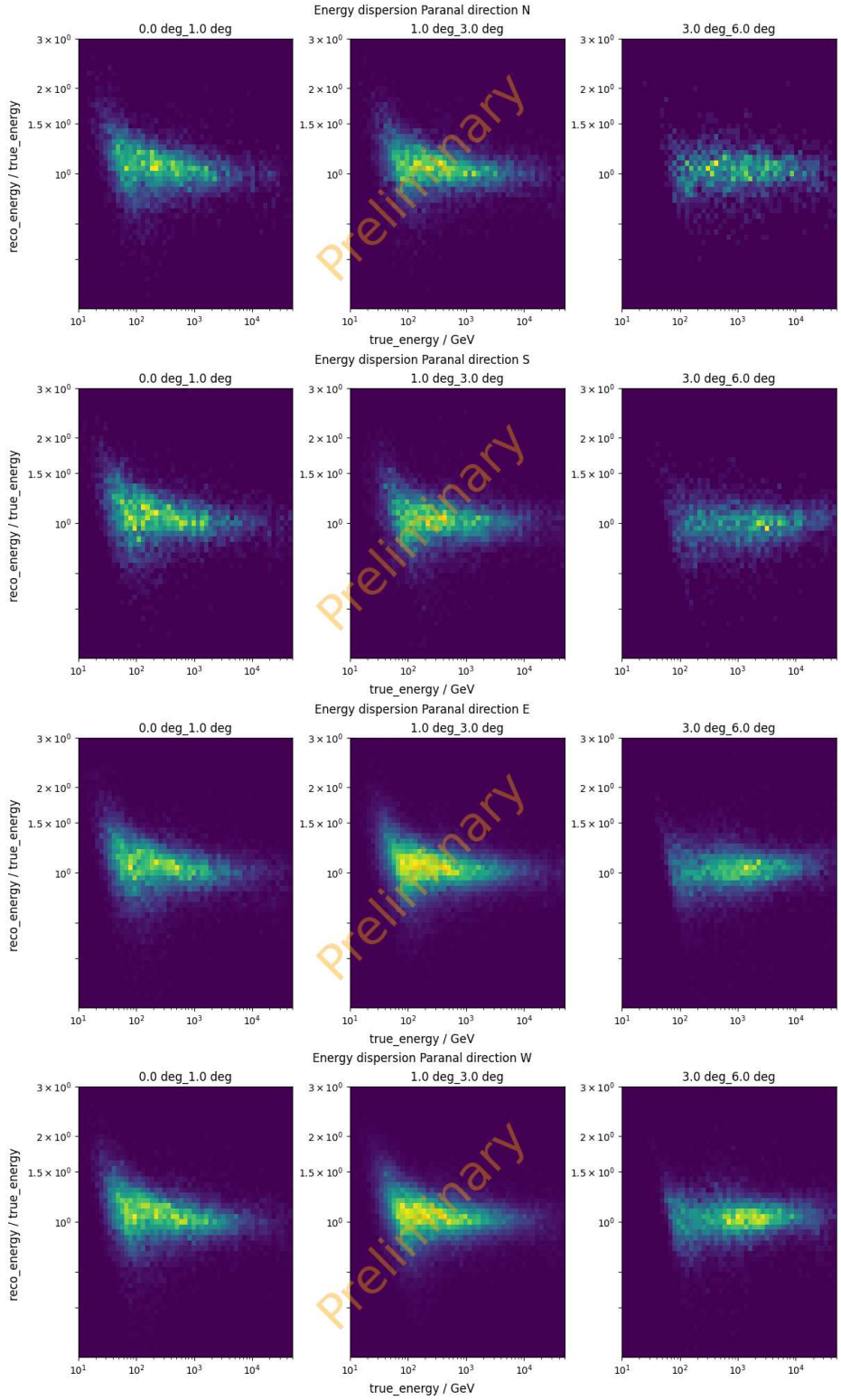

Figure 5.14: Evolution of energy dispersion with growing distance from the center of the hFoV for divergent cfg3. Each line refers to one of the directions reported in Figure 5.8.

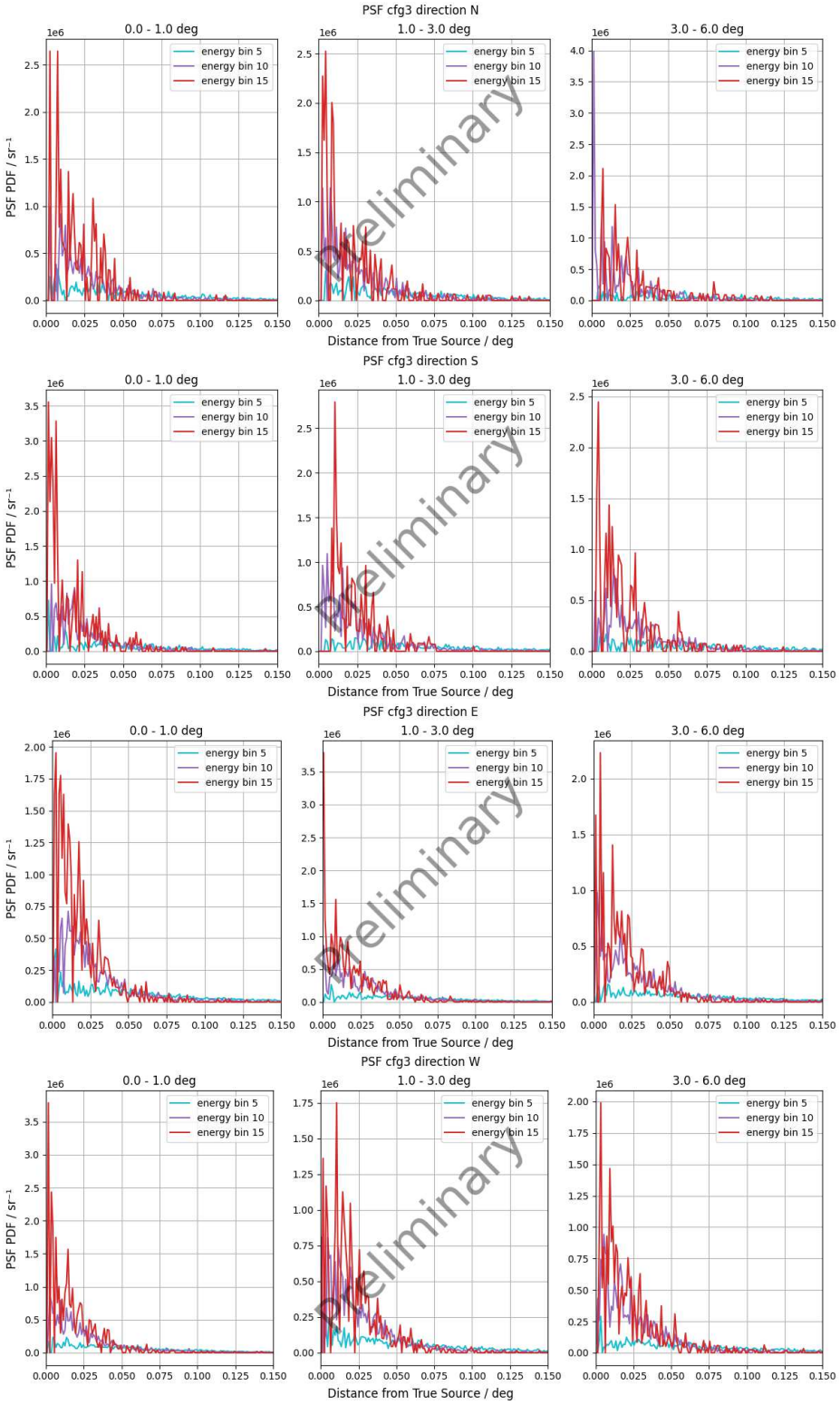

Figure 5.15: Evolution of PSF with growing distance from the center of the hFoV for divergent pointing cfg3. Each line refers to one of the directions reported in Figure 5.8.

Chapter 6

Implementing divergent pointing in the telescope drive system

This chapter provides insights into the first steps towards implementation of divergent pointing in the telescope drive system by the Array Control And Data Acquisition (ACADA) group. A study is conducted to analyze the variations in the hFoV shape while the array tracks an object in the sky. The study focuses on understanding how the hFoV geometry and multiplicity evolve over time, determining how often it is safe to repoint the array, and identifying critical positions where multiplicity is drastically reduced.

6.1 Field of view evolution

The studies discussed in the previous chapters were performed in AltAz coordinate systems. To allow a proper implementation of the divergent pointing mode by the ACADA group, the constraints provided by the telescopes drive system shall be taken into account. Each single telescope could track a single sky position in RaDec. The object of this study is to analyse the geometrical evolution of the array hFoV while tracking a position in the Sky, aiming to answer the following questions:

- How do the hFoV geometry and multiplicity evolve with time?
- How often is it safe to repoint the array? What is the effect of repointing on hFoV?
- Are there any critical positions (in RaDec coords), where multiplicity is drastically reduced in time?

To answer this question I wrote a short python code. The `divtel` code, introduced in 4.5, computes telescope pointing directions in horizontal coordinates, on the other hand tracking is handled in equatorial (Ra,Dec) coordinates by drive system. The choice to track a list of known stars makes it easier to compute their position in a horizontal system after each time interval. The number and position of stars is chosen in a way that

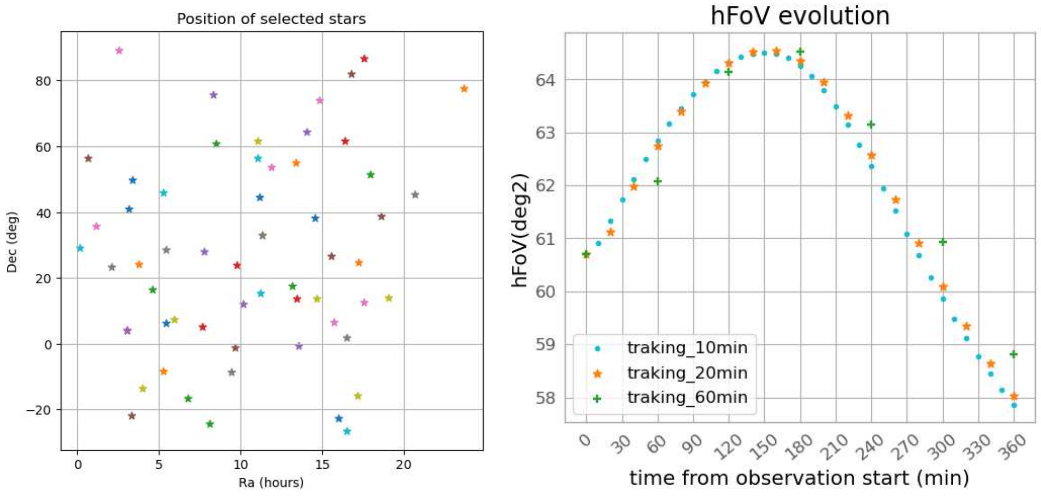

Figure 6.1: **Left**:Plot of the position, in equatorial coordinates, of the list of stars used for site North. **Right**: Evolution of the array hFoV geometrical dimension when recomputed after tracking the same source for time intervals of different length

allows to probe as many positions as possible. An example of the stars selected for site North is shown in Figure 6.1 The code is programmed to calculate the AltAz coordinates for each of the selected stars and start tracking their corresponding positions as soon as they become visible, i.e., when their altitude exceeds 24 degrees. The tracking process continues as long as the star is deemed visible, even during daytime. This inclusivity during day-time is intentional, as the primary focus is on observing the behavior of the array's hFoV, which remains independent of the specific time of day or the time of the year. The code computes the hFoV for the array in divergent mode, aligning with the position of the tracked star. Subsequently, the position of the star is recalculated in horizontal coordinates after a time interval of Δt. Throughout this interval, each telescope tracks the sky position assigned to it initially by the `divtel` code, which is provided in AltAz coordinates and converted into Equatorial coordinates. This systematic approach enables the assessment of how the hFoV evolves over time during the tracking of different celestial objects. At the end of the tracking phase the hFoV is re-computed taking into consideration two different conditions:

- The final position of the telescopes resulting from the tracking process
- The array is re-pointed, with the same divergence, at the new star position (in horizontal coordinates)

These hFoV are then compared to each other and to the initial one. As a preliminary test, different values were used for Δt. These tests showed that repointing the array every 20 minutes does not significantly affect the hFoV and this value has been applied for the following phase.

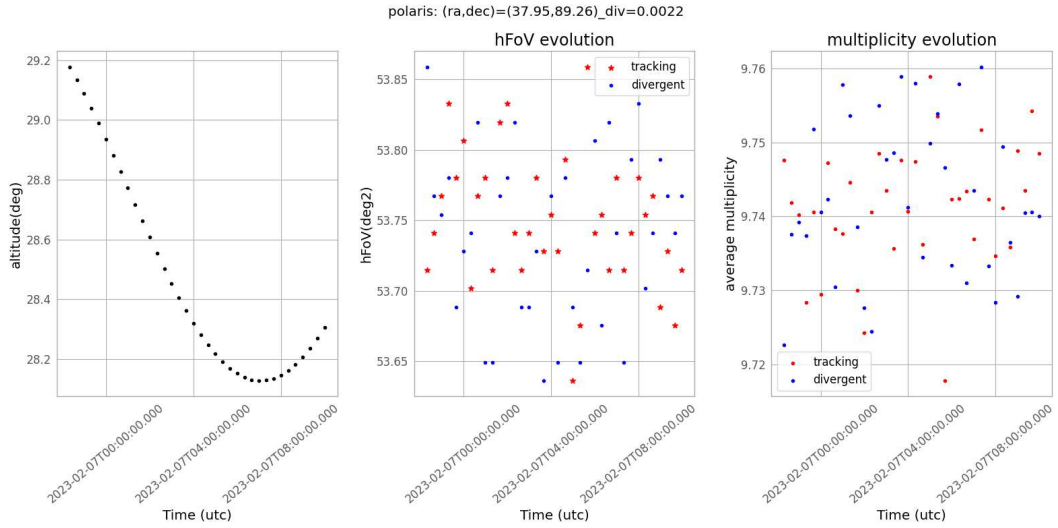

Figure 6.2: **Left**: Evolution of Polaris altitude during the night.**Center**: evolution of the hFoV area while tracking the source. **Right**: evolution of average multiplicity while tracking. The divergence applied to the array in this case is eqaul to 0.0022

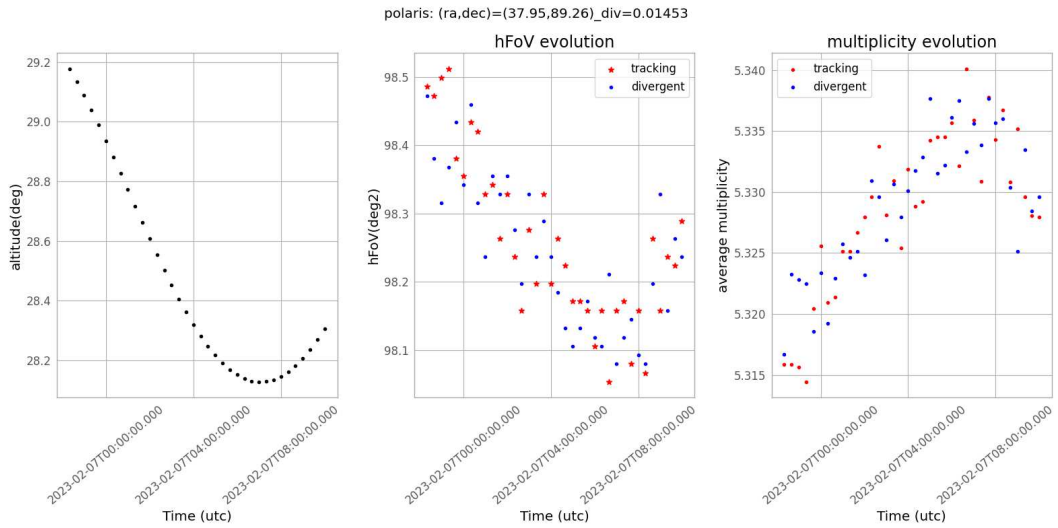

Figure 6.3: **Left**: Evolution of Polaris altitude during the night. **Center**: evolution of the hFoV area while tracking the source. **Right**: evolution of average multiplicity while tracking. The divergence applied to the array in this case is eqaul to 0.01453

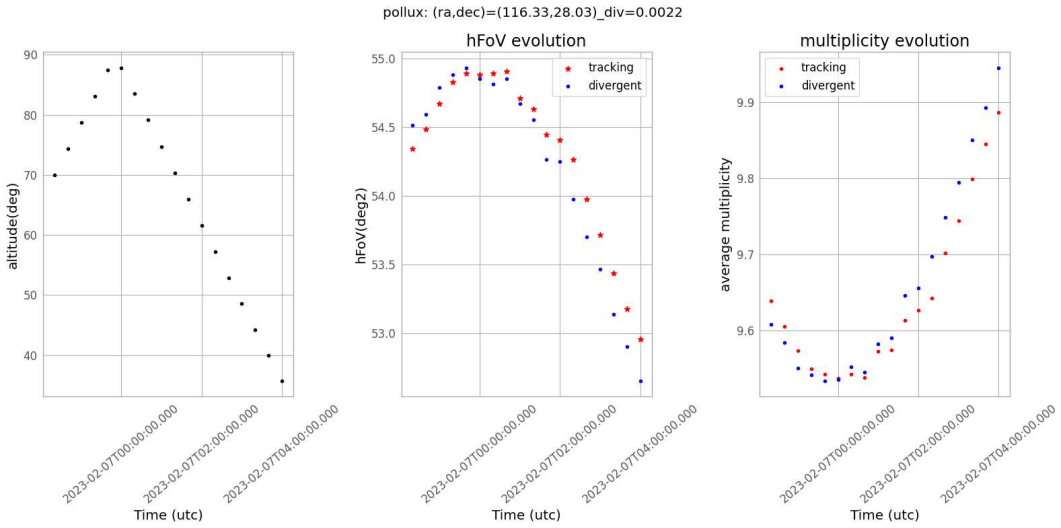

Figure 6.4: **Left**: Evolution of Pollux altitude during the night. **Center**: evolution of the hFoV area while tracking the source. **Right**: evolution of average multiplicity while tracking.

The presented plots illustrate the dynamic changes in the hFoV and average multiplicity while the telescope array tracks celestial objects such as Polaris, Pollux, and Adhara. The behaviour of the Northern array while tracking Polaris is reported in Figure 6.2 for cfg1.5 and Figure 6.3 for cfg5. Polaris, being nearly stationary in the sky throughout the night, serves as a unique case on the celestial sphere. The plots show that the hFoV shape remains relatively stable throughout the tracking process. The hFoV's response across various altitude values can be examined through the example of Pollux, Figure 6.4. This star, during the selected night, ascends at a low altitude and reaches culmination near 90 degrees. The changes in hFoV and multiplicity consistently correlate with the two employed methods for their computation along the trajectory of the monitored star. The same kind of analysis can be performed for the Southern site, where Adhara is tracked (see Figure 6.5). These findings significantly contribute to our understanding of the hFoV's evolution during divergent pointing. Particularly, they shed light on how different stars' apparent motions impact the observational capabilities of the array, offering crucial insights for optimizing observational strategies and enhancing the overall performance of CTA.

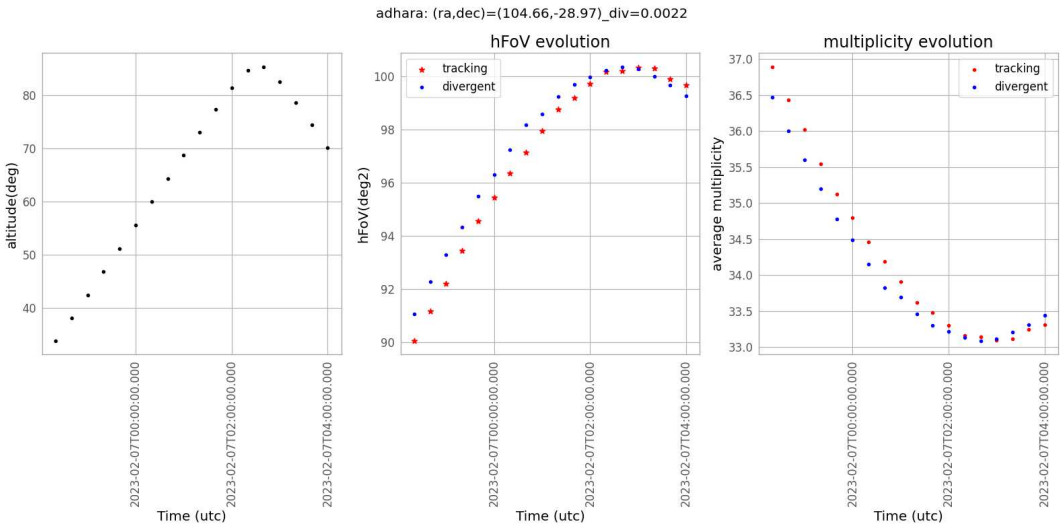

Figure 6.5: **Left**: Evolution of Adhara altitude during the night. **Center**: evolution of the hFoV area while tracking the source. **Right**: evolution of average multiplicity while tracking.

Chapter 7

Discussion

This document outlined the progress made over the past three years in computing the response of the CTAO Southern array in divergent mode. Updated simulations were generated and analyzed using a new data analysis pipeline, which shows promising results. However, a fair comparison with standard simulations is still pending and will be conducted in the coming months. The reference parallel simulations considered here only took into account point-like, on-axis sources. Moreover LSTs are absent in the subarray and the MST camera simulated is NectarCam instead of FlashCam. Once the feasibility of this method is established, various challenges must be addressed. I will try to outline here, point by point, the open questions on divergent pointing that are still to be addressed.

To wobble or not to wobble
IACTs generally observe in the so-called wobble mode [55]: the observed source is not pointed directly, but two to four opposite positions with a certain offset from the source are tracked alternately the same amount of time. Observations in divergent mode require careful consideration of wobbling and how to estimate the background. The reason why the wobble strategy is applied is to prevent possible camera asymmetries in the response to affect the data analysis. When applying the divergent mode the source distance from the camera center is different for each telescope. Assuming wobbling is still needed, one must understand how to apply wobbling: is it better to compute a distance and a rotation angle with respect to the axis corresponding to the array CoG or should this be applied on a single telescope basis?

Trigger condition
The stereo trigger is not appropriate for divergent pointing observations. Since each telescope points to a different direction a software trigger strategy is necessary. This requires to carefully determine the time lag with which the same signal is expected to hit different telescopes.

Real-Time Analysis (RTA)
RTA is crucial for spotting signals as soon as they are triggered, a condition that

is of fundamental importance for transient sources. However, when applied to divergent pointing, the strategy must be able to detect signals across the hFoV combining in the proper way single telescope's FoV.

Need for massive simulations

As mentioned earlier, implementing this strategy demands significant computational resources in terms of both processing time and storage space. Covering a wide range of values in altitude and azimuth for all configurations is currently impractical. The challenge is further compounded by the need to explore additional configurations beyond the ones already analyzed, considering the obtained values of average multiplicity which are far from the threshold value (m_{ave}=3)

Apply mixed divergence values

When going to larger values of divergence the SSTs tend to be more and more spread, with the peak of multiplicity moving away from the center of the array, see e.g. Figure 7.1.

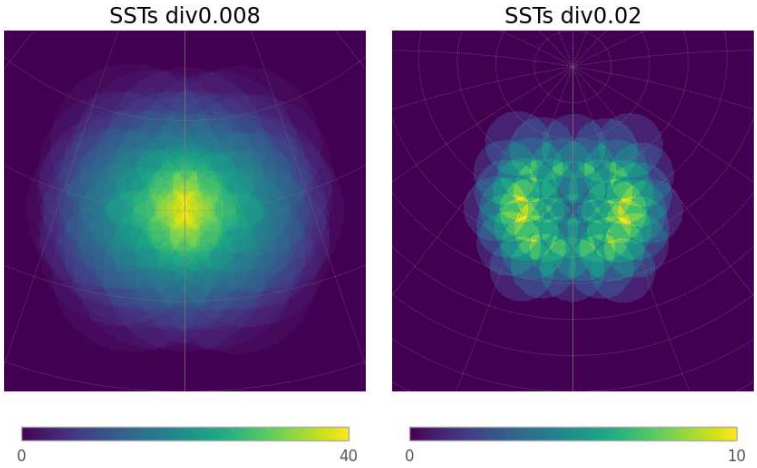

Figure 7.1: Example of SSTs FoV in divergent mode for two different values of divergence, 0.008 (**left**) and 0.02 (**right**)

Some uniformity can be restored applying different values of divergence to different subarrays. This possibility was already considered in one of the first works on divergent pointing [102]. Applying a lower value of divergence to the outer groups of telescopes would benefit the reconstruction capabilities of the array while keeping the same symmetry conditions. For this purpose the code has been slightly modified to allow applying different values of divergence to selected groups of telescopes. Convergent values (negative divergence) are also possible. More studies are to be performed on these configurations.

Some of the aforementioned questions are currently addressed also for parallel mode and several groups in CTAO are currently working on it. A stronger interaction with

these groups will be established in the future, to implement divergent mode observations adequately.

Chapter 8

Conclusions

In recent years an innovative observation strategy, known as the *divergent mode*, was proposed for the Imaging Cherenkov Telescopes, in particular for the Cherenkov Telescope Array Observatory (CTAO), as an alternative to the traditional *parallel pointing*. The concept behind this strategy is straightforward: the individual telescopes in the array are then tilted outward from the direction to which the center of the array is pointed. While this strategy offers the advantage of expanding the total instantaneous Field of View (FoV) of the array, it comes at the cost of a reduction in the overall array performance. The primary objective of studies conducted in this area is to strike a balance between the dimension of the FoV and the performance of the telescope array. The work presented in this thesis focused on the performance of CTAO Southern array in divergent mode. In recent years the performance of site North was already presented but a deep study of the Southern site, implying updated simulation configurations, both in terms of array configuration and telescope structures was still missing. This work analysed the array in a modified version of the so called Alpha configuration (4LSTs are added). The divergent configurations analysed are five, whose divergence values allow to cover all the values of average multiplicity of interest. The effective hyper Field of View (hFoV) covered with these configurations spans from 89 deg^2 to 285 deg^2, and the corresponding average multiplicity goes from 33.5 to 7.6. Since the value of multiplicity obtained for the most divergetn configuration is still greater than the one we use as a threshold (m_{ave}=3) more configurations will be analysed in the future. All these configurations have a common feature to which more attention will be given from now on: the outer Small Sized Telescopes (SSTs) point to a direction that is too much bent in the outwards direction with respect to the direction of the array Center of Gravity (CoG). This condition, that worsens with growing values of divergence (div), can be mitigated if a lower value of div is applied to those telescopes.
Thanks to this study it was also possible to help validating the new data analysis pipeline, which substituted the previous one. The results obtained show that the pipeline correctly handles divergent pointing simulations and the obtained performance is promising and allows to go further with the analysis of this mode and its applications.
In order to determine which configurations are more suitable to perform the different

science tasks considered `gammapy` can be used. The IRFs produced for this study are already compatible with `gammapy`, which can be used to simulate the observation of real sources in divergent mode. Once the configurations are determined an important task will also be to define the proper way to combine different pointings.
This study highlighted some open points in the implementation of divergent pointing strategy. All of these issues, listed in Chapter 7, will be adressed and discussed keeping close contact with the working groups taking care of the different topics, to make sure that the implementation will be as smooth as possible. The acquisition of real data in divergent mode will soon be possible either with the array composed by the two MAGIC telescopes and LST-1 or the array of four LSTs, whose construction started in the past months. The study conducted for this proposal showed that `magic-cta-pipe` can handle divergent pointing simulations and that can be used for data analysis in case the test will be realised with a mixed (MAGIC-LSTs) array.

Appendix A

Contributions to the LST collaboration

The first Large-Sized Telescope (LST-1) was built by the LST Collaboration at ORM on the Canary island of La Palma ($\sim$100 m away from the MAGIC telescopes). Inaugurated in October 2018 it is currently under commissioning. During this phase the telescope subsystems are tested while the first astronomical observations are carried out. Once the commissioning will be over, and the acceptance review successfully passed, the LST-1 will become the first telescope of the CTA Observatory.
As part of its commissioning program, the LST Collaboration has already taken more than 250 hours of γ-ray data while the telescope was pointing at bright, known VHE emitting sources. A large number of hours are devoted to Crab Nebula observations, being this source considered a standard candle in γ-ray astronomy. These data have been used to tune the parameters of the Monte Carlo simulations to the characteristics of the telescope and to estimate the key performance parameters such as angular resolution, energy resolution and sensitivity. Figure A.1 shows the spectral energy distribution of the Crab Nebula obtained from LST-1 data collected between November 2020 and March 2022, more detailed results obtained from Crab Nebula data are reported in [41].
Taking advantage of the short distance separating LST-1 from the MAGIC telescopes LST-1 has been cross-calibrated with the two MAGIC telescopes. Joint observations of established γ-ray sources are performed as part of the commissioning of LST-1. Showers brightness, estimated energies of γ-rays, and other parameters can be compared event by event in order to cross-calibrate the telescopes. A combined analysis of the events triggering the three telescopes, allows to reconstruct the shower geometry more accurately, leading to better energy and angular resolutions, and a better discrimination of the background showers initiated by cosmic rays.
Several other known bright γ-ray sources were observed and detected by the LST-1, and the first ATel has been circulated (ATel #147835) to announce the detection of the flare of BL Lac source. This achievement shows the community that the LST collaboration is already capable of releasing results within one day from the data taking.
Transient phenomena are listed among the core program tasks of the LST sub-system

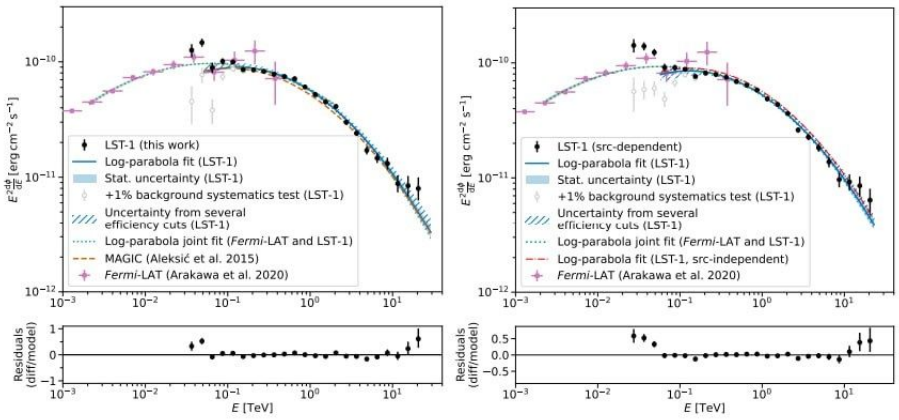

Figure A.1: Spectral energy distribution of the Crab Nebula obtained from LST-1 data collected between November 2020 and March 2022 (from [41]). **Left**: results using source-independent analysis. **Right**: results using source-dependent analysis.

and a prototype transient handler system that receives, in real-time, science alerts from the Gamma-ray Coordination Network (GCN), was installed on the LST-1. Thanks to this system, LST-1 was able to already observe one GRB within 15 minutes from the alert [4].
As a part of my PhD duties I took part in some tests aimed to certificate that the performance of one of the LST-1 subsystems, the camera Calibration Box (CaliBox), is consistent with the requirements reported in the Technical Design Report (TDR [81]) document issued by the LST collaboration. I took some shifts as Burst Advocate (BA) as part of the LST-1 transient group. In this section I will report the results of the tests performed on the CaliBox and the data analysis of the GRBs observed during the BA shifts.

A.1 Camera Calibration Box

The CaliBox is the device aimed at calibrating the camera PMTs. The LSTs camera is composed of an array of 1855 photomultiplier (PMTs), organized in 265 modules of 7 pixels each with a quantum efficiency (QE) reaching 40% at 350 nm wavelength [99]. The PMT signals are sampled thanks to the Domino Ring Sampler version 4 chips (DRS4[1]) and digitized by an analog-to-digital converter (ADC). Fast sampling is essential to achieve the low energy threshold by reducing contamination of night sky background (NSB) light which enters each pixel with a rate of $\sim$ 250 MHz [83]. The LST camera external structure has a square shape with the edge of about 3 m. The photo-sensitive area has a hexagonal shape and the field of view is about 4.5 degree in diameter. In order

[1] "https://www.psi.ch/en/drs"

to cover a wide dynamical range (1-3000 phototelectrons - p.e.) the camera readout has two channels with different amplification for high gain (HG) and low gain (LG). During regular operations the camera acquires raw waveform data (R0) that must be corrected by several DRS4 systematic effects (offset of individual capacitors, dependence of the offset on the time since the last reading of the capacitor) and converted from integrated charge in ADC counts to the number of p.e. produced by light pulses in each PMT, also called absolute charge calibration.

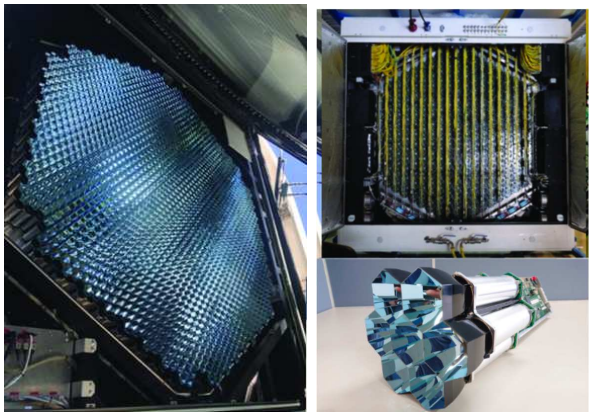

Figure A.2: Pictures of the LST-1 camera front plane (**left**), backplane and a single PMT module (**right**).

Both DRS4 correction and pixel calibration are based on Pedestal and Flat-Field Events. The former are simply events triggered without signal (closed shutter), the latter are produced by the CaliBox. The CaliBox is installed at the center of the LST mirror dish and mechanically consists of an aluminum structure composed by a thick plate surmounted by two connected boxes all protected by an external shell. The two inner boxes host the optics, composed by a 1 μJ Q-Switch 355 nm laser, two filter wheels, an Ulbricht sphere and a laser controller. An internal weather sensor is placed next to the laser head in order to monitor the internal relative conditions (pressure, humidity and temperature). Inside the shell are placed the power supply system, an external weather sensor, a trigger interface board and the mini PC to pilot the CaliBox, via OPC-UA Server protocol[2].
The filter wheels have six positions each, one of which is left empty while the others host five UV Neutral Density filters, resulting in a total of 35 filter combinations that allow us to cover a wide range of photon densities (from 1 to 10^5 photons per camera pixel).
The first CaliBox, currently installed on LST-1, together with other two CaliBoxes, has been developed, built and tested by INFN (*Istituto Nazionale di Fisica Nucleare*). In

[2]The OPC Unified Architecture (UA) is a platform independent service-oriented architecture that integrates all the functionality of the individual OPC Classic specifications into one extensible framework, for more details see https://opcfoundation.org/

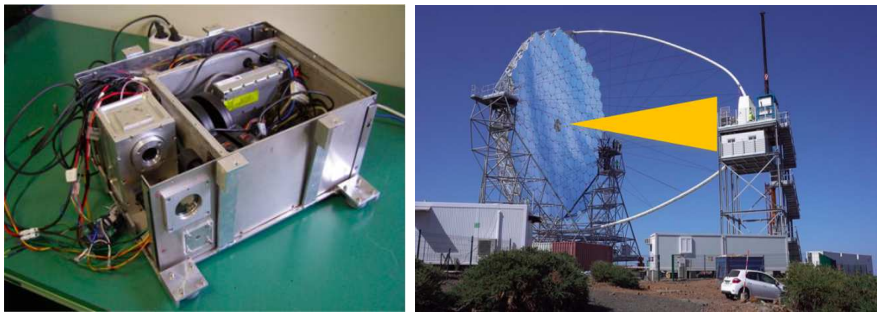

Figure A.3: **Left**: picture of the LST-1 CaliBox showing internal boxes and external shell [90]. **Right**: Sketch of the CaliBox light cone on LST-1.

order to make sure that the CaliBoxes built in our laboratories satisfy the TDR it is mandatory to test them before shipment to the telescopes' site. The performance tests are meant to validate the uniformity of the light beam, the stability of the laser intensity, the dynamic photon range and the sealing of the Ingress Protection level. I took part in the uniformity and photon dynamic range test, preparing the experimental setup and building my own python data analysis pipeline for the Calibox Spare, built and tested at the laboratory of *Dipartimento di Matematica Fisica e Informatica - DMIF* at Udine University.

A.1.1 Uniformity test

The aim of the uniformity test is to make sure that the emitted light will be able to uniformly illuminate the surface region of the telescope camera PMTs ∼28 m away from the mirror disk center, where the CaliBox is installed.
The laboratory used for this task is endowed with an optical table, equipped with a vertical (x, y) structure along which couple of Sensl 3x3 mm^2 Silicon-Photomultiplier (SiPM) can be moved. The optical table was covered with black fabric in order to avoid unwanted photon reflections that can be caused by the room furniture or walls. For this experimental setup the ClaiBox is placed 5 m away from the vertical frame.
A preliminary check on the signal shape and intensity is performed using an oscilloscope: this procedure is fundamental to prevent SiPM signal saturation and check possible device misalignment. The readout system is a triggered DRS4 evaluation board whose output is saved on a laptop.
The procedure described hereafter is the one I followed to cross-check the uniformity of the CaliBox Spare of LST-1. The signal was sampled on a 2D grid, (25 cm × 25 cm)[3] of 49 points as showed in Figure A.4, where the decided sensor spacing on the (x, y) screen guarantee a flux variation lower than 1%. For my data-taking I set the laser shooting frequency to 2 kHz and the DRS4 triggers threshold to -40 mV, to avoid

[3]This dimention is set in order to intercept all the laser light in an opening angle sufficient to cover teh entire camera PMT size surface 28 m away from the CaliBox

baseline noise level (measured during a set of test runs). Figure A.5 left reports the entire run acquisition window by the DRS4 (external trigger mode), where one run corresponds to 1000 singular sampled events (see Figure A.5 right). The final goal is to determine

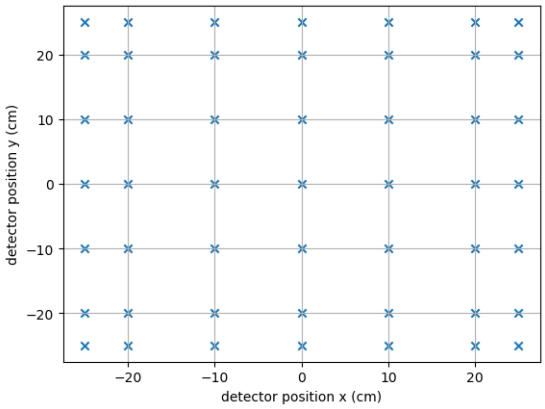

Figure A.4: Grid of points where the CaliBox signal has been sampled.

the number of photons hitting the sensor surface, which is proportional to the integral of the sampled signal pulse shape. Signal cleaning and integration is performed thanks to a simple code I wrote in Python language.

In the list below the steps performed by the analysis pipeline are summarized:

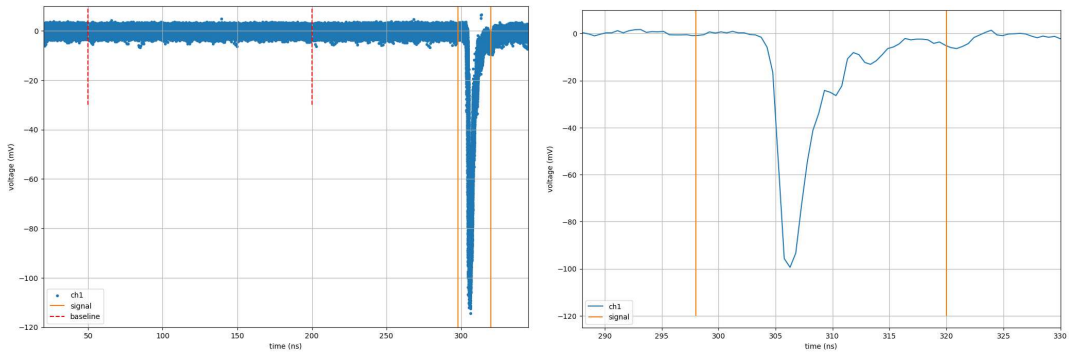

Figure A.5: **Left**: Data run example corresponding to 1000 laser pulse acquisition: in red the baseline time selection (50 - 200 ns), in orange the pulse integration window. **Right** Detail of a single laser pulse event.

- **Data preparation**
  Figure A.5 (left) reports a complete run, composed by 1000 laser pulses sampled in the same time window by the DRS4. Due to the signal baseline offset jitter two time intervals are selected: one related to the background and the other one for the selection of the time integration window. In order to properly individuate the

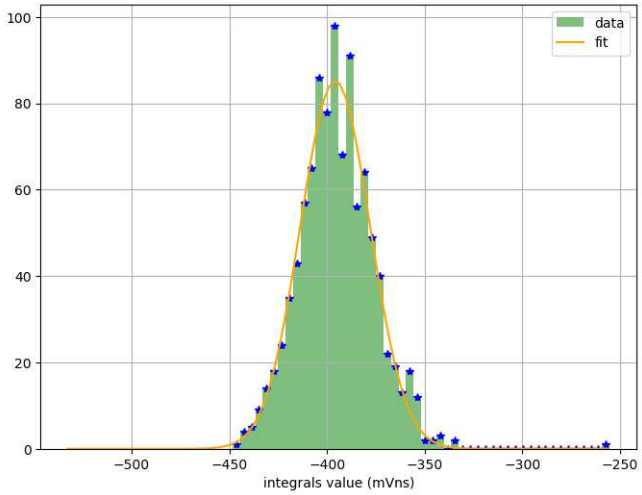

Figure A.6: Histogram representation of the 1000 pulse integrals in a run fitted with a Gaussian function. The mean distribution value $< I_p >$ is taken as the run reference value.

baseline value for each pulse, without loosing computational time, the mean value of the signal is computed in the time range between 50 and 200 ns. The value thus obtained is used to rescale each signal.

- **Signal integration**
  In this phase all the 1000 rescaled signals are integrated inside the selected time window (see orange lines in Figure A.5) using the Simpson's method implemented in `scipy.optimize`. To properly represent the mean pulse integral value, $< I_p >$, for each run, a Gaussian function fit is applied to the histogram exploring the 1000 pulse integral value dispersion. These first two procedures are repeated for all the data runs (i.e. the 49 different sensor positions on the screen).

- **Result**:
  As a first order approximation the CaliBox can be considered to be perfectly aligned with the center of the screen and not tilted with respect to a plane parallel to the wave front, this condition is also verified during the first setup tests. The value corresponding to the position (0,0) on the screen is taken as the $< I_p >$ reference value. The uniformity request is than satisfied if all the got $< I_p >$ values, representing the 49 different positions of the sensor on the screen, will not differ from the reference one for more than a 2%[4].

This same setup is also used to make sure that the area uniformly illuminated by CaliBox, at a distance of 28 m, does exceed the camera frame surface: this is essential to avoid flashing other telescopes.

[4]This value corresponds to the TDR requests regarding signal uniformity.

A.1.2 Dynamic range test

The purpose of this measure is to determine the selectable number of $photons/cm^2$ emitted from the CaliBox. This number can be derived by taking into account the statistical properties, for different filter combinations (runs, of the $< I_p >$ values distribution. In a regime where the number of emitted photons is low $< I_p >$ values dispersion is expected to follow the Poissonian distribution, thus the following relation holds [54]:

$$\sigma^2 = k < I_p > + O(< I_p >^2) + const \tag{A.1}$$

where σ^2 is the $< I_p >$ standard deviation, k is the parameter of interest, $O(< I_p >^2)$ takes into account possible intrinsic variations of the light source and *const* term is given by the electronic noise.
For this photon flux measure the intensity of the CaliBox signal was measured with Photomultiplier tube (PMT - Hamamatsu-H5783-04[5]) at a distance of ∼2 m from the CaliBox.
To determine the CaliBox photons' dynamic range, the measurement has to be repeated

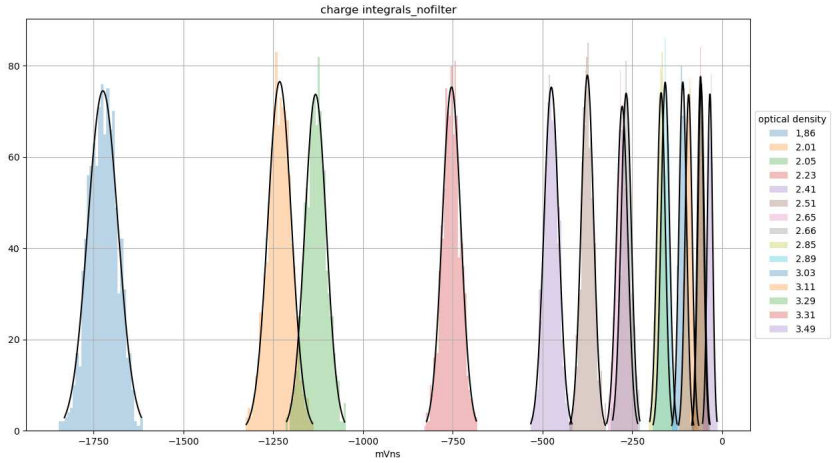

Figure A.7: Histogram I_p representation for differnt filter combinations. Each dataset is first fitted with a Gaussian function. I'ts worth noticing how the mean pulse integral value decreases with growing optical density, defined as $OD = -log_{10}(\mathrm{T}/100\%)$ where T is the transmittance.

for different filter combinations. The $< I_p >$ values with the relative variance, obtained using different filter combinations, are reported in a σ^2 vs $< I_p >$ plot fitting a linear function to hte data. The linear term in the fit is mainly proportional to the PMT gain and allows to determine, starting from the $< I_p >$ value, the number of photoelectrons (n_{pe}) generated in the detector:

$$n_{pe} = \frac{< I_p >}{k}. \tag{A.2}$$

[5]http://pdf.datasheetcatalog.com/datasheet/hamamatsu/H6780-03.pdf

Once the number of photoelectrons is determined, the corresponding number of photons hitting the sensor can be obtained by means of the detector Quantum Efficiency (QE). This quantity is defined as the number of photoelectrons generated per incident photon on a photosensitive device effective area

$$QE = \frac{n_{pe}}{n_{\gamma}} \tag{A.3}$$

and can be found on the technical data-sheets of the detector. The number of $photons/cm^2$ for each laser shot expected at 28 m from the light source can than be estimated:

$$\phi_{camera} = \phi_{PMT} \frac{d^2_{PMT}}{d^2_{camera}} \tag{A.4}$$

where ϕ_{camera} is the flux that hits the camera surface at the distance $d_{camera} = 28$ m and ϕ_{PMT} is the flux that hits the PMT at the distance d_{PMT}.

A.2 Chasing GRBs with LST-1

Thanks to their fast slewing and large effective area the Large Size Telescopes (LSTs) will be the instruments best suited to significantly impact on short timescale transients follow-up. The observations of the early emission phase of a wide range of transient events with good sensitivity below 100 GeV will allow to open new opportunities for time-domain astrophysics in an energy range not affected by selective absorption processes typical of other wavelengths. The LST-1 can respond to external triggers thanks to a specific Transient Handler (TH) [4] system receiving the external trigger provided by the Gamma-ray Coordinates Network (GCN) [6]. When an alert is received by the GCN, the TH parses the alert and builds a human-readable text with the relevant information, which is then distributed to different mailing lists. The Burst Advocate (BA) main responsibilities are helping shifters with the observation of transient alerts (GRBs, high energy neutrinos, GWs, FRBs, etc.) and setting up an observation strategy. The BA operates mainly at night, when is called by the shifters. However, it may happen that the BA is the person contacting the shifters in the case of alerts received before or close to the start of observations. Most of the alerts come form GRBs and the BA is expected to perform a fast analysis of the data collected from the alert looking for a possible signal. In the following section I will briefly introduce GRBs and the LST-1 data analysis pipeline, and will report on some of the analysis I performed during shifts as a BA. I chose the analysis of an event observed in dark NSB conditions and one in moon conditions.

[6] https://gcn.nasa.gov

A.2.1 Brief history of GRBs

The name Gamma Ray Burst perfectly describes the temporal and energetic behaviour that characterized GRBs at the time of their discovery. Between 1967 and 1972 sixteen brief bursts of photons in the γ ray energy range 0.2-1.5 MeV were observed by the Vela surveillance satellites. This discovery was first announced in 1973 [73], the delay was due to the need to establish with high confidence that the origin of these bursts was not terrestrial. These first events showed variable duration, from fractions of seconds to minutes, during which GRBs were the most luminous sources of the sky. For two decades scientists studied these sources with both satellite and Earth based instruments with poor results. The breakthrough came in 1990 thanks to the Burst And Transient Source Experiment (BATSE) instrument, onboard the Compton Gamma-Ray Observatory (CGRO). This detector, specifically designed to detect and locate γ-ray bursts, detected 2704 GRBs during the 1990s. These observations allowed astronomers to es-

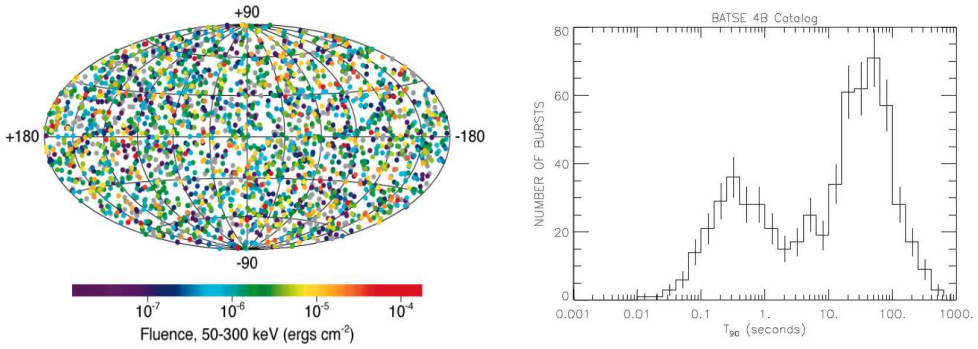

Figure A.8: **Left**: Distribution over the sky of the 2704 GRBs observed by the BATSE experiment onboard the CGRO. **Right**: Distribution of γ-ray bursts observed by BATSE showing the bimodality between long and short bursts.

tablish some of the properties of the events. Among their most important properties is the isotropic distribution of the GRB incoming directions, shown in the left plot of Figure A.8, and a bimodality in the distribution of their duration, shown in the right plot of Figure A.8. This quantity is described by a parameter called T_{90}, defined as the time interval needed to collect 5% to 95% of the burst counts in the BATSE energy band (50-300 keV). Bursts with $T_{90} < 2$ s are called short GRBs, while the ones with longer duration are called long. This bimodality in the emission was later discovered to be associated to a difference in the progenitors of GRBs, with long bursts originating form the collapse of massive stars and short ones form the coalescence of binary systems of compact objects. Nonetheless, the distinction is not so sharp.
Today we know that this burst in the hard-X-ray/soft-γ-ray band is just the first phase of the GRB emission, also called *prompt emission*. It is dominated by emission in the keV-MeV energy range, lasting from fractions of a second to several minutes, and reaching isotropic equivalent peak luminosities (E_p) in the range L$\sim 10^{49} - 10^{53}$ erg s^{-1}. The

spectral shape of this phase of emission is described by an empirical function introduced by Band et al. [24]. The GRB non-thermal spectrum is usually fitted by two power-law functions smoothly connected at a break energy:

$$N(E) = A \begin{cases} \left(\frac{E}{100\,keV}\right)^{\alpha} e^{-\frac{E}{E_0}}, & E < (\alpha-\beta)E_0 \\ \left[\frac{(\alpha-\beta)E_0}{100\,keV}\right]^{(\alpha-\beta)} \left(\frac{E}{100\,keV}\right)^{\beta} e^{\beta-\alpha}, & E \geq (\alpha-\beta)E_0 \end{cases} \tag{A.5}$$

where N(E)dE is the number of photons in the energy bin dE, while the unknown parameters are the low-energy (α) and high-energy (β) spectral slopes, E_0 the break energy and A the normalization factor. The energy power spectrum (νF_ν, where F_ν is the flux density spectrum) is usually represented as $E^2N(E)$. The typical spectral energy distribution (SED) is a peaked function with $E_{peak} = (2+\alpha)E_0$.
The prompt emission is followed by a second emission phase, called the *afterglow*, detected on a very wide range of frequencies, from γ-rays to the radio band. The afterglow flux decays smoothly as a power-law in time for weeks or months, and the typical frequency of the radiation moves in time from the X-ray to the radio band. An afterglow was observed for the first time in 1997, following the prompt emission of the long GRB 970228 [39]. This discovery has been possible thanks to the Italian-Dutch satellite BeppoSAX. Afterglow observations, first in the X-rays and later in the optical and radio band, allowed to determine the precise position of the bursts confirming their extragalactic origin. In 1998 a supernova-γ-ray burst association was suggested by the coincidence of the SN 1998bw with the GRB 980425 event [57]. This association was firmly established for GRB 030329 observed on March 29th 2003 which was observed optically and showed that the characteristic broad lines of an extremely energetic supernova were observed within days of the event [68].
Through the years several X-ray and γ-ray instruments were lunched in the to explore X-ray and γ-ray band, such as the INTErnational Gamma-Ray Astrophysics Laboratory (INTEGRAL) in 2002, the Neil Gehrels Swift Observatory (Swift) in 2004, the Astro-Rivelatore Gamma a Immagini Leggero (AGILE) in 2007, and the Fermi Gamma-ray Space Telescope (Fermi) in 2008. A great boost in GRB observations was achieved thanks to these instruments, a great example is teh detection, in 2017 by Fermi and INTEGRAL, of a short GRB temporally coincident with a GW event (GW170817) [2][1]. The GW signal turned out to be generated from a binary system of merging neutron stars, with a probability of the near-simultaneous temporal and spatial observation of GRB 170817A and GW 170817 occurring by chance is 5.0×10^{-8}. Therefore, binary neutron star mergers could be confirmed as a progenitor of short GRBs.

VHE emission is also predicted by GRB theoretical models and the data collected by the Fermi Large Area Telescope (Fermi-LAT) demonstrated that GRBs can produce photons at energies well above 10 GeV and that they should be intrinsically able to radiate above 100 GeV. These sources are thus among the primary targets for ground based γ-ray observatories. In 2019, after 15 years of observations, the first GRB afterglow in the VHE band was observed by the MAGIC telescopes. After this first observation several other detections have been claimed by MAGIC [82] [7] [30] [31], H.E.S.S.[3] [44]

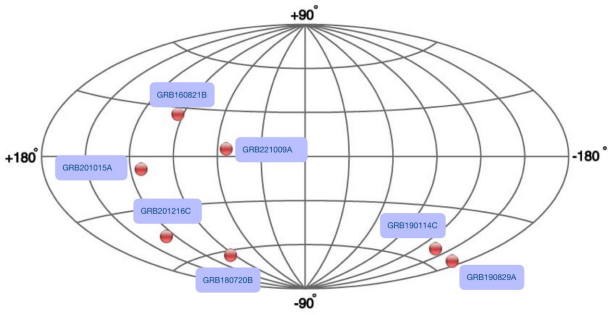

Figure A.9: Sky map of GRBs observed at VHE by ground based γ-ray detectors.

and more recently by LHAASO [69]. Studying the TeV spectra and light curves offers new observables to narrow down the enigmatic aspects of the afterglow physics. These observations are expected to have a substantial impact on our current comprehension of the surroundings where GRBs explode which, in turn, will shed light on the nature of their origins. A contribution to the understanding of the physics of ultra-relativistic shocks, and of the properties of the jet is also expected.

A.2.2 LST-1 analysis chain

`cta-lstchain` is the analysis library for the observed and simulated LST-1 data. The pipeline is heavily based on `ctapipe` and follows the data analysis scheme described in the previous sections to obtain lists of candidate γ-ray events from raw data files. Data are organized according to the standard data levels already introduced

- R0 : Uncalibrated RAW waveforms from the camera
- R1 : Calibrated waveforms from the camera
- DL1a : Integrated charge and peak position of the waveform
- DL1b : Image parameters (width, length, intensity, etc.)
- DL2 : Event parameters (energy, direction, time, etc.)
- DL3 : Lists of reconstructed events after event selection with corresponding IRFs (A_{eff}, energy dispersion, PSF, etc.)

A simplified version of the LST-1 data analysis pipeline is shown in Figure A.10, together with the different tools used for each step. The steps marked with `lstchain` must be run by the analysers using the corresponding `lstchain` command.

`lstmcpipe`
: `lstmcpipe` handles the analysis of MC data on the cluster at La Palma. It produces the trained models and the MC DL2 files required for data analysis. Both train and test MC samples are available on the on-site computing infrastructure.

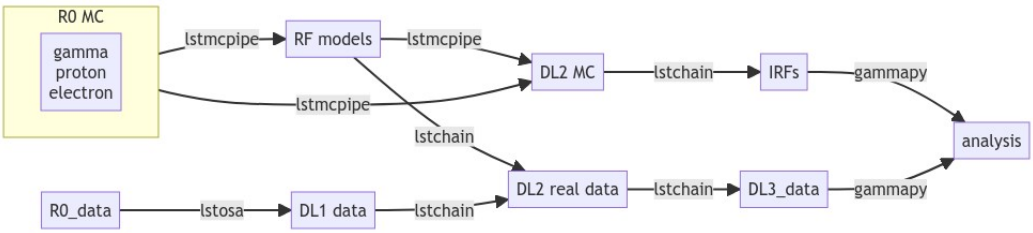

Figure A.10: Simplified version of the LST-1 data analysis pipeline and the different tools used for each step.

γ-rays and protons are simulated in a wide range of telescope pointing directions, up to $\simeq 70°$ zenith distance. These directions are chosen in two different grids of pointings, one for the training MC and one for the test MC. The training MCs are generated using pointings that follow "declination lines", which essentially trace the path followed by all sources at a specific declination when observed from the LST-1 site. The test MCs are simulated in a grid of zenith and azimuth values. A more detailed description of the MC samples available and of the pipeline can be found in [41].
The NSB assumed in the LST-1 simulations is the one of a "dark" sky field; however practical observations take place under a broad spectrum of NSB conditions, including moderate moonlight levels or twilight conditions. The approach adopted in order to have matching NSB levels between data and simulations, consists in adding some random Poissonian noise to the MC events during the analysis chain, right before the image cleaning step.

lstosa

`lstosa` is a fast LST On-Site Analysis chain, aimed at performing a reduction of the raw data at the LST-1 site, so that the low and intermediate analysis products are available to the LST Collaboration and delivered by internet to the CTA data centers [87] [97]. The pipeline also performs data quality checks to debug potential problems. To ensure reproducibility `lstosa` tracks the provenance of the analysis products. DL1 files required for data analysis are automatically produced by `lstosa` and analysers should not need to use this package directly (it is maintained and handled by LST Onsite analysis team).

lstchain

The DL1 files to be used depend on the source you want to analyse. Unless one has a good reason, the latest version of the DL1 files should be used. The list of available trained RF models can be found in the lstmcpipe documentation and production list, along with a description of each production. The choice of the RF to use is related to the source position: the closest declination line should be used, and the NSB level of the data. For dark observations the RFs already available are fine, whereas for moon or twilight observations one must estimate the

NSB level of the input files. This is done by changing the config file of the RF models and producing new DL1 files and training new RF models. To produce a config file tuned to the data you want to analyse, you may run `lstchain_tune_nsb` function that will produce a tuned_nsb_config.json file. Following the training phase, the random forest models are applied to the Monte Carlo (MC) data for each of the test sample pointing nodes. This application is carried out to compute the Instrument Response Functions (IRFs). Additionally, the same models are used with real DL1 data to derive DL2 data. The low-level data analysis can be conducted in two distinct manners: source-dependent and source-independent. In the source-dependent analysis, prior knowledge of the true source position is utilized during event reconstruction. On the other hand, the source-independent approach assumes no prior information about the source position. The IRFs are computed with the `pyirf` package and used to evaluate the performance of the LST-1. Starting from DL3 files ,generated from given data DL2 file and IRF files, the high level data analysis is performed through `gammapy`.

A.2.3 GRB analysis

As member of the transient working group of the LST collaboration, I performed several GRB analysis during my Burst Advocate shifts. In this section I will give an overview of the properties of the GRBs I analysed and I will show some results for GRB221221A, automatically repointed for the first time and observed under dark conditions, GRB230414B, again observed under dark conditions and the only one with known redshift, and GRB230723B, observed under moon conditions.

GRB221221A

This event is a long GRB triggered by Fermi GBM at 22:39:33 UTC on December 21^{st} 2022[7]. At 23:04 UTC the automatic procedure started automatic data taking under dark conditions. Being an event triggered by GBM the errorbox is quite large (radius=2.7 deg), nonetheless the observation is performed in standard wobble mode around the alert coordinates. During data analysis it became clear that the telescope control Unit (TCU) applied a wrong wobble offset (0.8 deg instead of 0.4 deg) to the source. This does not make any difference in the data analysis. The observations happen in dark conditions (the moon, grey line, rises after the end of the observation window - marked by the yellow vertical lines), meaning that it is safe to use the RFs already available to go from DL1 data, produced by `lstosa`, to DL2. The presence of a source can be checked already at DL2 level, with a θ^2 plot, where θ is the angular distance between the source position (known from the alert) and the position of the source reconstructed from the data. Usually a check of the θsquared plot is sufficient to establish if any signal from the source is present. For this event, due to the large error associated with the source position, it is necessary to search for hot-spots in the counts map. Figure A.11 right shows that the closest declination line is the one corresponding to dec=61.66 deg. Figure

[7]https://gcn.gsfc.nasa.gov/other/693355175.fermi

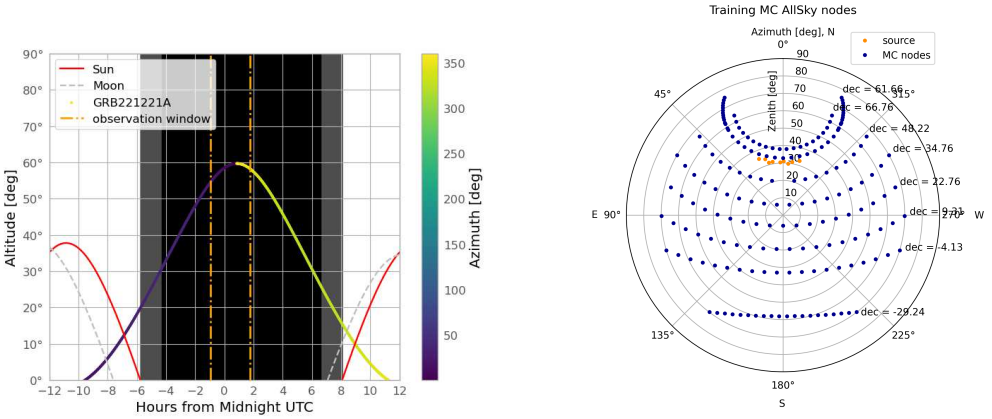

Figure A.11: **Left**: Visibility of GRB221221A from LST-1 site during the night between December 21^{st} and December 22^{nd}, 2022. **Rigth**: Path of the source in the sky during observations and training nodes available.

A.12 shows both the θ-squared plot with respect to the GBM source position and the sky map obtained from fast analysis. Both plots show no sources, neither in the declared position, nor across the FoV.

GRB230414B

This event is a long GRB ($T_{90} = 25.98 \pm 8.86$ s) triggered by Swift-BAT at 16:15:16 UTC on April 14^{th} 2023[8].

LST-1 started observations at 22:00 UTC on the same day, with a delay of 5h 45min min and observed the source for a total time of 3.4h. The source has been observed by a large number of instruments in several wavelengths and the Gran Telescopio de Canarias (GTC) estimated its redshift to be 3.56[9]. As shown in the right plot of Figure A.13, the Training MC that lies closest to the GRB data is the one along the declination line dec_48.22. The plot on the left, in the same figure, shows the altitude evolution of the GRB position as seen from the ORM during the night between April 14^{th} and April 15^{th}, 2023. The observations happen in dark conditions (the moon, grey line, rises after the end of the observation window - marked by the yellow vertical lines), meaning that it is safe to use the RFs already available to go from DL1 data, produced by `lstosa`, to DL2. Since this source was well localized it is sufficient to have a look at the θ-squared plot, reported in Figure A.14 left. From the plot can be seen that no signal was detected.

GRB230723B

The GRB230723B is again a long GRB triggered by Swift-BAT. The trigger came on July 23^{rd}, 2023, in the morning (T_0=11:42:45 UTC). No redshift is available for this GRB. The visibility window for LST-1 started around 21:30 UTC and the

[8]https://gcn.gsfc.nasa.gov/other/1164180.swift
[9]https://gcn.gsfc.nasa.gov/gcn3/33629.gcn3

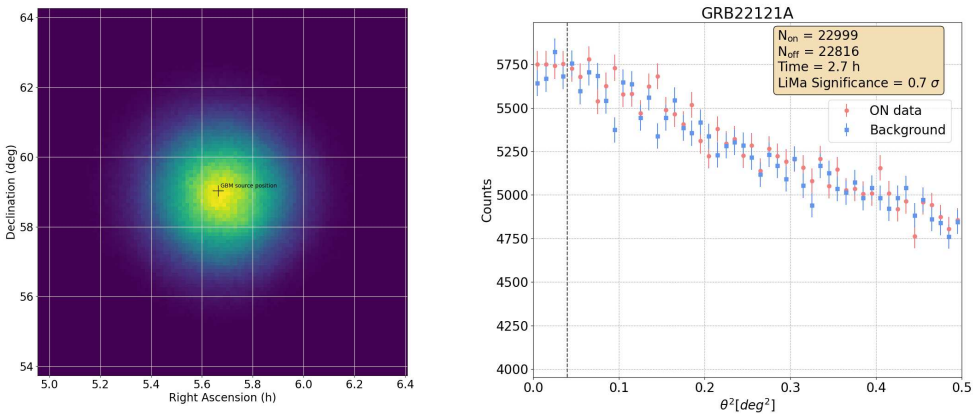

Figure A.12: Sky Map (left) and θ-squared (right) plot for GRB221221A. θ-square is computed with respect to the source position given by GBM.

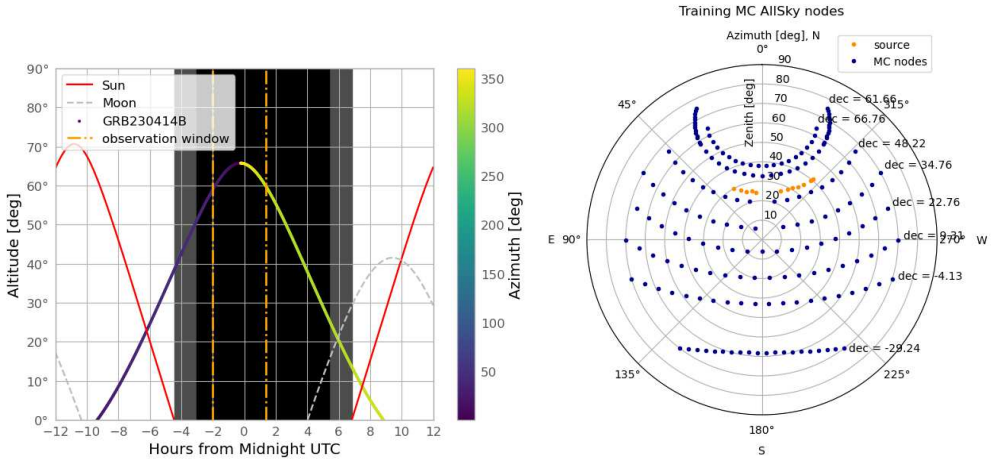

Figure A.13: **Left**: Visibility of GRB230414B from LST-1 site during the night between April 14 and April 15, 2023. **Right**: Path of the source in the sky during observations and training nodes available.

GRB was observed for 3.2h with a delay of 10h from T_0. Unfortunately the NSB conditions were not optimal, due to the presence of the moon, as shown in the right panel of Figure A.15. This required a tuning of the MC Training sample, corresponding to the declination line dec=-4.13, to the NSB level of the real data. The noise levels to be added have been computed run by run. The NSB levels thus computed have been applied to the MC DL1 data corresponding to the closest node to each run. This step is performed thanks to `lstchain.scripts.lstchain_dl1ab`. These MC files are then used to generate RF models for energy regression, particle

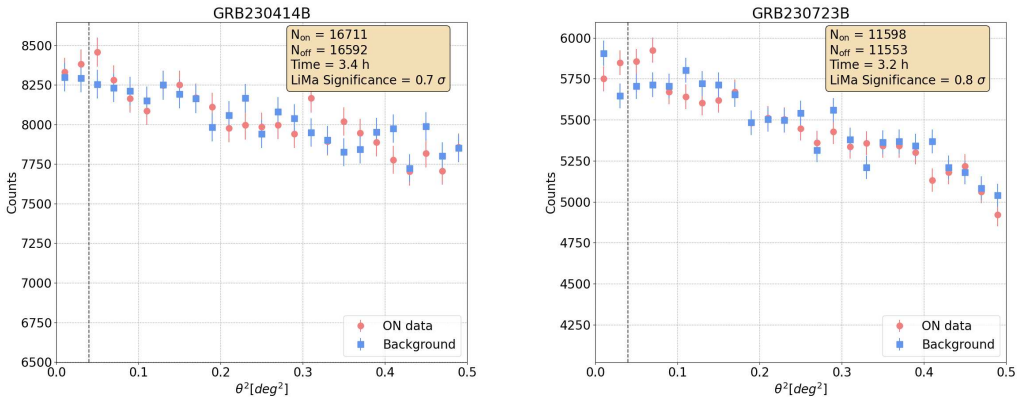

Figure A.14: **Left**: θ^2 plot for GRB230414B obtained from DL2 data. **Right**:θ^2 plot for GRB230723B obtained from DL2 data.

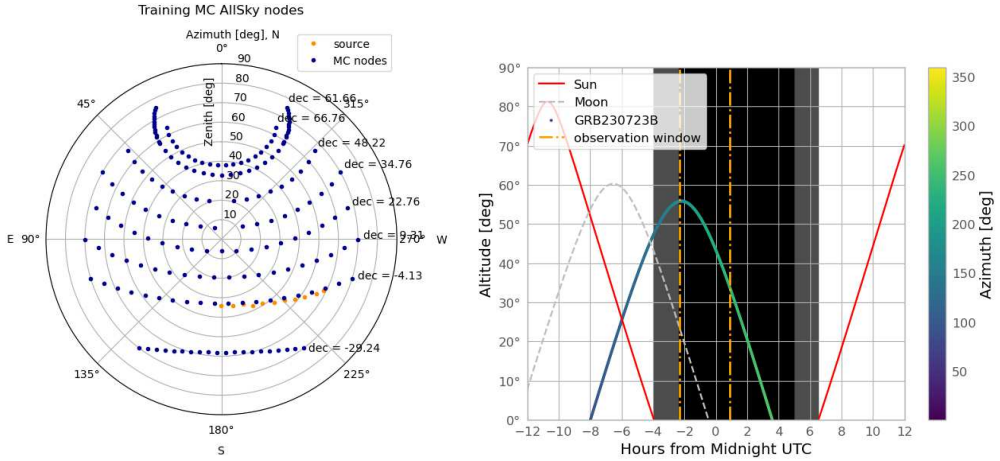

Figure A.15: **Left**: Path of the source in the sky during observations and training nodes available. **Right**: Visibility of GRB230723B from LST-1 site during the night between July 23 and July 24, 2023.

classification and disp parameter estimation. These models are applied to OSA DL1 data corresponding to the GRB and a preliminary θ-squared plot is produced. Unfortunately also for this GRB there is no signal, as can be seen in the right plot of Figure A.14 right. There is no need to go further with the analysis.

Appendix B

A proposal to test divergent pointing mode

The MAGIC call for observing cycle 18 proposals closed in October 2022. Together with a group of people working on divergent pointing and involved in both MAGIC and LST collaborations, we submitted a technical proposal aimed at testing divergent pointing with a real array of telescopes, namely the two MAGIC telescopes and LST-1.

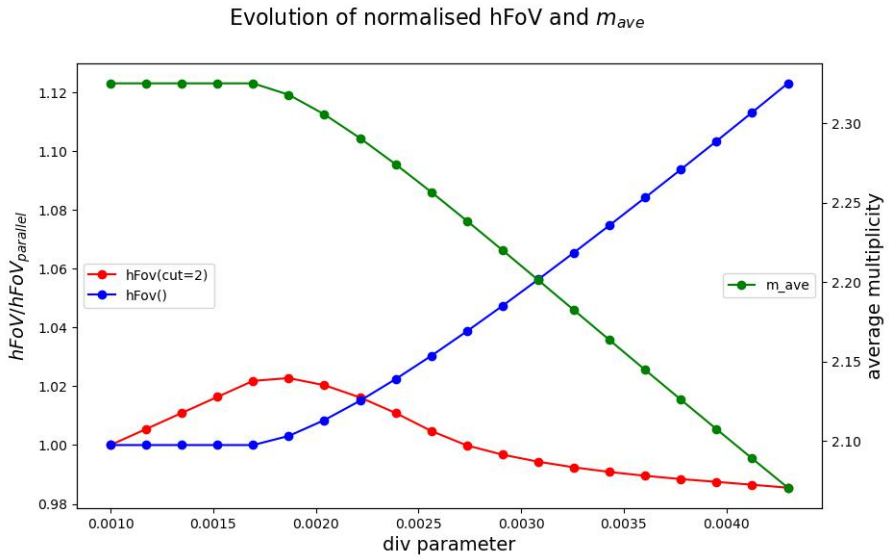

Figure B.1: Evolution of hFoV area (with respect to the parallel condition) and multiplicity with growing values of divergence. The blue line represents the total (geometric) hFoV, the red line takes into account only the area of the hFoV covered by at least two telescopes.

The idea was to perform a few hours of observations, either in dark or light moon conditions, pointing each MAGIC telescope and the LST-1 in a direction determined by

the divtel code. The source around which the array is diverged is the Crab Nebula. The final goal is to establish, using some real data, the validity of the method, while shedding light on the potential technical issues that will be faced when implementing divergent pointing for CTA. To choose the divergent configuration the dimension of the FoV and the average multiplicity are analysed for a set of values of div, going from div=0 and div=0.45. The maximum value is the one that gives a value of m_{ave}=2, which is the minimum requirement to label an event as triggered. Figure B.1 shows the evolution, with respect to the div parameter, of the hFoV area relative to the value obtained in parallel mode and average multiplicity. The blue line refers to the global (geometrical) hFoV, while the red line refers to the hFoV covered by at least 2 telescopes. The latter is the relevant parameter in determining the value of divergence to apply to the system. The value of div selected is the one that maximizes the area of the hFoV covered by at least two telescopes (div=0.00186). I run the simulations on the LST-1 computing container, using `CORSIKA`/sim_telarray version 77100. The analysis was performed using the `magic-cta-pipe` software, developed for joint magic-lst1 analysis. In the next section the text of the proposal is reported as presented to the MAGIC collaboration.

B.1 Observations of the Crab Nebula with MAGIC and LST-1 in divergent mode

Scientific justification for the proposal (THREE pages maximum, text in pages 2 and 3, references and figures in page 4):

The goal of this proposal is to perform the **first observations of a source using divergent pointing**[50][60]. The aim of this first test is purely technical: we want to establish if divergent pointing is working as it should (e.g. from the trigger point of view), if the software is able to handle such a pointing mode and to establish the technical challenges related to it.
One of the advantages of the future generation of Imaging Atmospheric Cherenkov Telescopes (IACTs), represented by the Cherenkov Telescope Array (CTA), is the large number of high-performance telescopes that will constitute the array. This will allow for the use of pointing modes different from the nominal one (currently used by all IACT arrays), referred to as "parallel mode", where all telescopes point to the same position in the sky. Using standard pointing strategies, the total field of view (FoV) of an array is highly limited by the FoV of the individual telescopes. The current generation IACTs can provide sky-coverage of 5-10 deg^2, which is very small as compared to the current generation gravitational wave (GW) sky-localization (of the order of 100-1000 deg^2).

One of the strategies of observation in order to cover the sky-localization of the GW events is by making tiling observations with narrow FoV [25, 92]. However, the rapidly decaying emission of the transient makes it difficult to observe these events with relatively narrow FoV of the current and even future generation facilities (i.e. CTA-LST). A significant increase in the possibility of detection of the GW counterparts in the VHE band is expected with the help of this strategy. The timeline of the LIGO-Virgo-KAGRA O4 and O5 runs[a] are scheduled in 2023 (March) and beginning of 2026, respectively. Thus a larger FoV obtained from **operational Divergent pointing will perfectly complement the LIGO-Virgo-KAGRA runs**.
In addition, the future generation of gravitational wave detectors such as Einstein Telescope (ET) and Cosmic Explorer (CE) are planned around 2030-2035 which can be synchronized with the full array operation of CTA. ET (and a network of ET and CE) will localize most of the GW signals with an accuracy of the order of 100 deg^2 [96] for close-by events (within redshift of 1-1.5.). Hence it is very timely to start to search for alternative technical observation strategies for maximizing the FoV of IACTs, in order to be able to maximize the detection rate of the EM counterparts of GW events. The alternative pointing mode we propose is the so-called divergent pointing. The idea on which it is based is the following: telescopes are inclined into the outward direction by an angle increasing with the telescope distance from the array center, allowing it to enlarge the overall FoV of the array (also referred as Hyper-FoV, hFoV). This gain in FoV comes with both advantages and drawbacks.
The direct **advantage** of an enlarged hFoV is the reduction of the time needed to cover large areas of the sky such as the one to be covered when performing sky surveys or when searching for electromagnetic counterparts in the multimessenger framework (such as GW events or neutrino events). This kind of observation will benefit as well the search for transient events, enhancing the probability of serendipitously detecting them inside the field of view while the array is operating in survey mode. The **drawback** is a worsening in the overall performance. Thus the value of the divergence to be applied to the system is chosen in a way that allows to maximize the size of the FoV while maintaining a certain average telescope multiplicity (number of telescopes looking at the same region of the sky), and, therefore, sensitivity. **MC simulations are also used to determine the performance of our array in divergent mode and determine if the sensitivity is still sufficient for our scientific purposes**.
Up to now, divergent pointing has been studied only through MC simulations. **We would like to test, for the first time, the divergent pointing on a real array of telescopes making it one of the pioneering works for alternative strategy of following-up of the transient events.**

[a] https://www.ligo.caltech.edu/news/ligo20220617

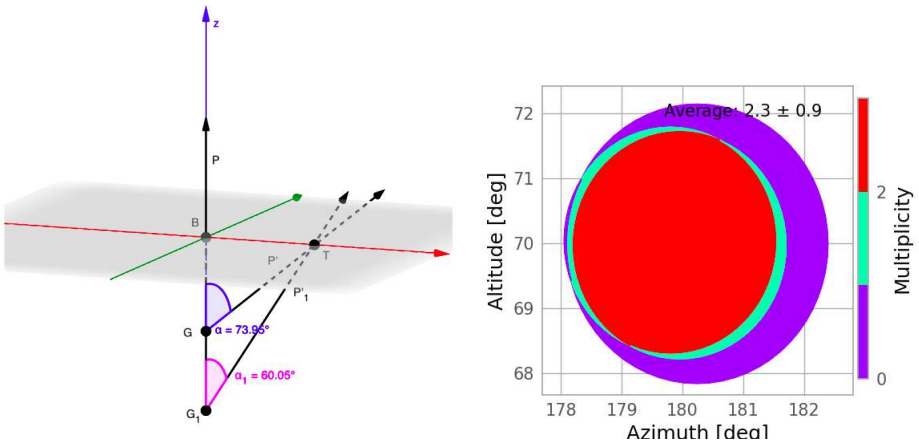

Figure B.2: **Left:** Graphic representation of divergent pointing concept. **Right:** Hyper Field of View of MAGIC + LST1 in divergent configuration (div=0.00186).

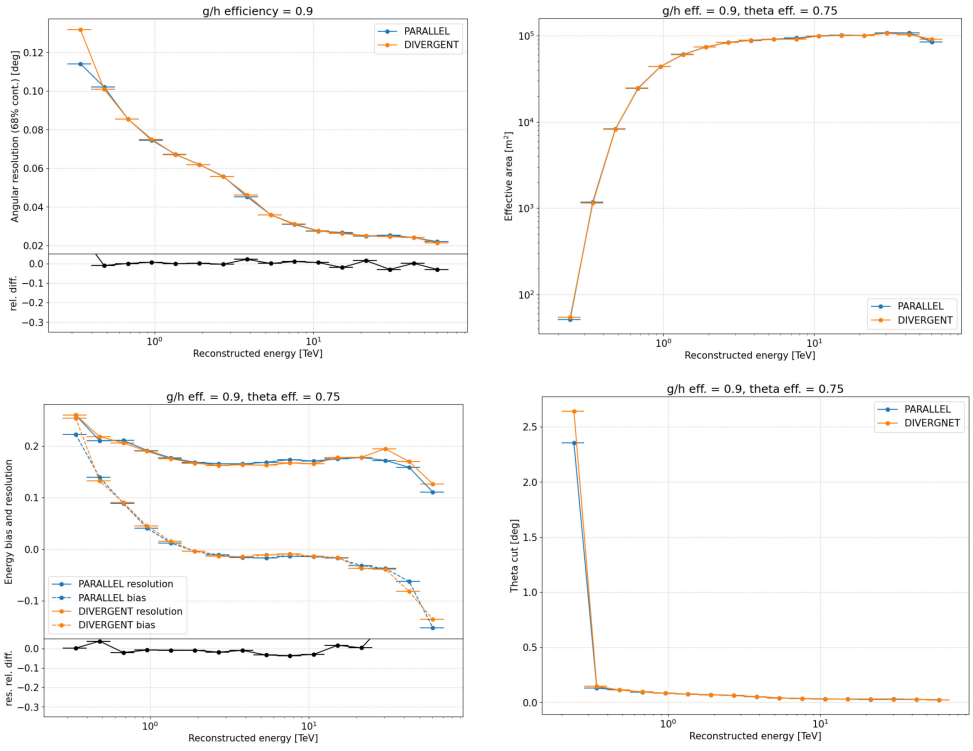

Figure B.3: Comparing MAGIC + LST-1 performance in parallel and in divergent modes (div=0.00186).

A simple model has been introduced in order to reduce the hyper-parameters needed to define the pointing direction of each telescope. This is called **"umbrella mode"** and is schematically represented in the pictures below [49]. The image shows the position of a telescope on the ground, T, the array center of gravity, B, and the position of a point, G, that defines the array divergence. The divergence angle, α, whose value should be defined for each telescope, increases with the distance from the array center. In order to control the divergence with a single parameter for the whole array, we defined $div = \sin(\alpha)$. The parameter div can move from 0 (parallel pointing) to 1 (maximal divergence). Given the value of div and the position of each telescope on the ground, the pointing direction of each telescope is defined. The value of divergence to apply to the system has been selected in order to (slightly) enlarge the hFoV maximizing the value of the effective hFoV (defined as the portion of the hFoV covered by at least 2 telescopes).
MC simulations have been performed using `CORSIKA` and Sim_telarray which have then been analyzed with magic-cta-pipe. The outcome of the simulations showed that, as expected, the performance of the array in this configuration is not significantly different from the one we achieve in parallel conditions. The div value is applied starting from a condition, where the telescopes point the source in on-mode, but none of the telescopes will, in the final position have the source exactly at the center of the camera. Applying a small value of divergence allows to keep the source at a maximum distance from the center that is lower than the standard wobble offset, thus preventing us from falling into a region of the MAGIC camera where the response is degraded.

Technical description of the MAGIC observations, including an explanation of the requested time criticality for these observations (in case it is different from 0):

For the divergent observations, a list of pointing directions for the three telescopes will be computed using divergent pointing tools for each source position. We are required to track the source for 20 minutes and then another list of positions will be given. In total, we require 20 h of Crab: 10h in divergent mode and 10h in parallel mode to be used as a comparison. The most important thing is the observing conditions (moon and zenith to be the same for both datasets)

Appendix C

Performance plots

The following section is dedicated to the performance plots of the configurations not reported in the main text.

C.1 Point-like performance

C.1.1 cfg1.5 - div0.0022

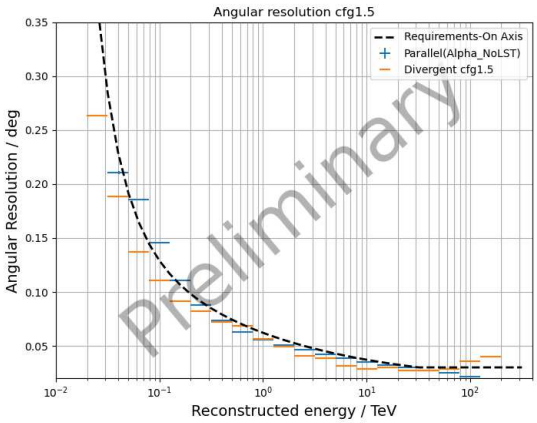

Figure C.1: Angular resolution for cfg1.5 obtained with `ctapipe`.

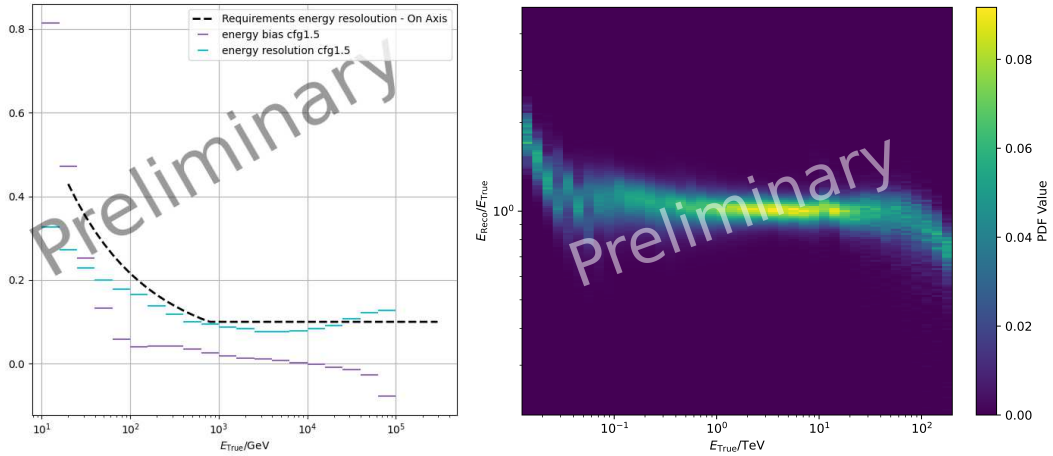

Figure C.2: **Left**: Effective area for divergent pointing configuration cfg1.5. The comparison is made with CTA requirements and with parallel pointing Southern array in the alpha configuration. **Right**: Background rate for divergent pointing configuration cfg1.5.

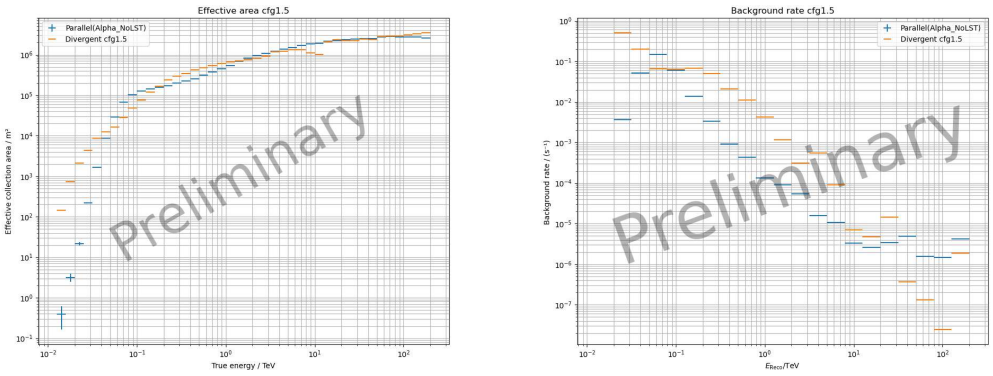

Figure C.3: **Left**: Effective area for divergent pointing configuration cfg1.5. The comparison is made with CTA requirements and with parallel pointing Southern array in the alpha configuration. **Right**: Background rate for divergent pointing configuration cfg1.5.

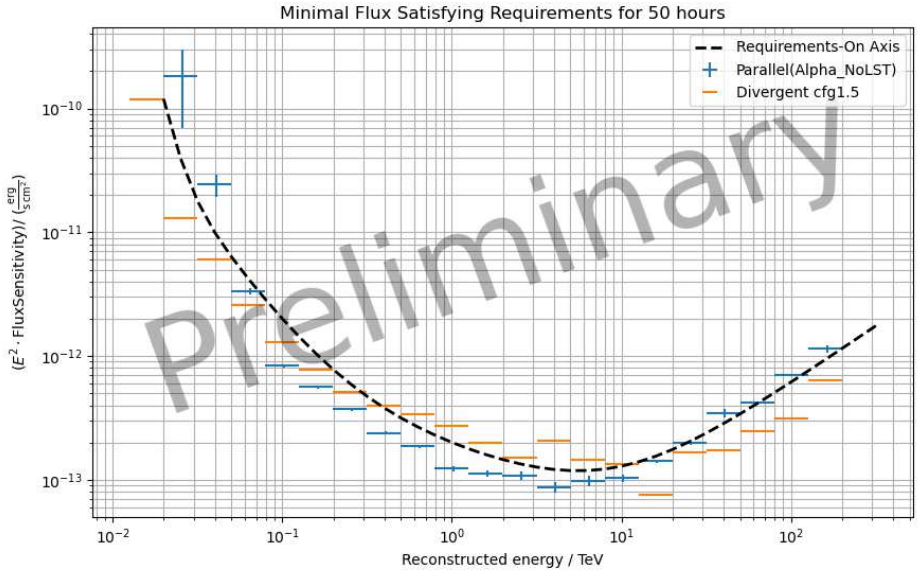

Figure C.4: Sensitivity to an on-axis point-like γ-ray source for divergent pointing cfg1.5.

C.1.2 cfg2 - div0.0043

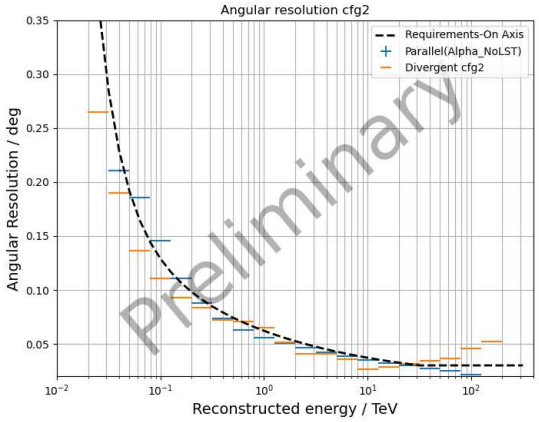

Figure C.5: Angular resolution for cfg2 obtained with `ctapipe`.

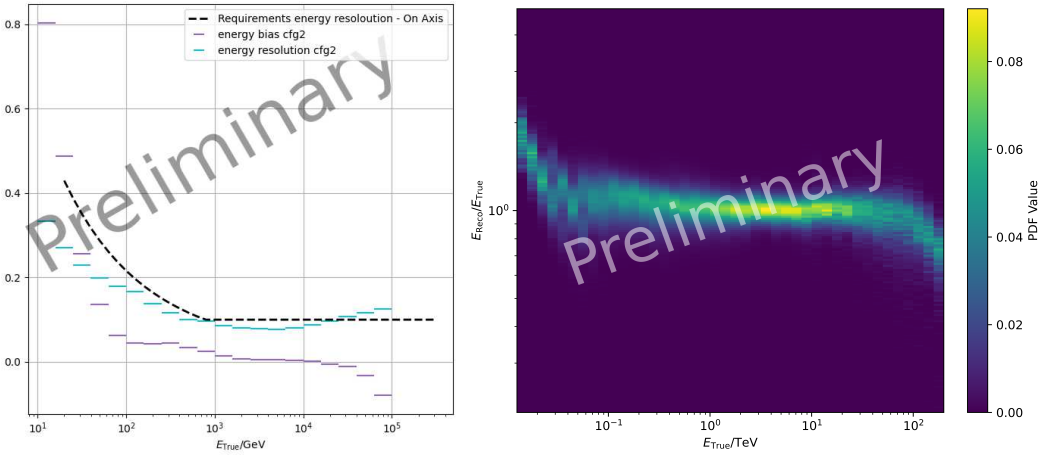

Figure C.6: **Left**: Energy bias and resolution for cfg2. The requirements refer to energy resolution only. **Right**: Energy dispersion relation for divergent pointing configuration cfg2.

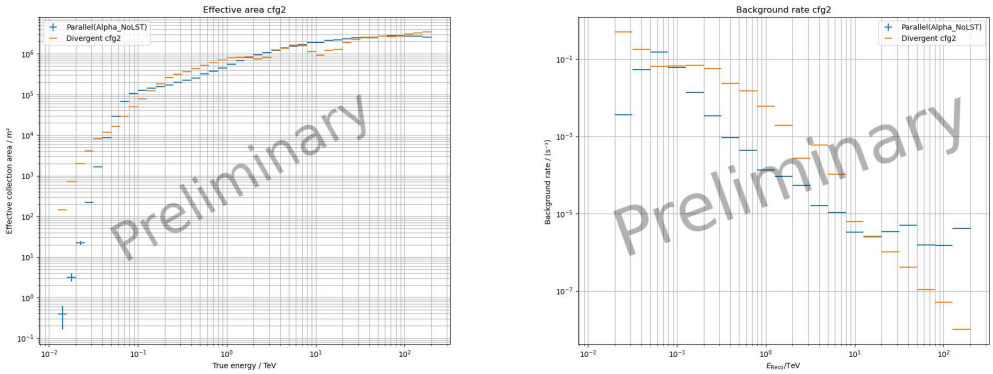

Figure C.7: **Left**: Effective area for divergent pointing configuration cfg2. The comparison is made with CTA requirements and with parallel pointing Southern array in the alpha configuration. **Right**: Background rate for divergent pointing configuration cfg2.

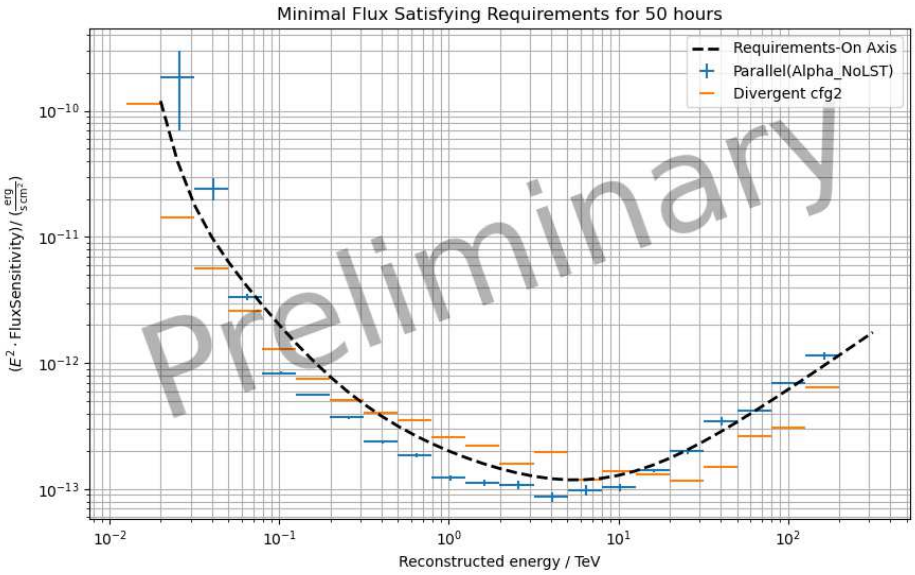

Figure C.8: Sensitivity to an on-axis point-like γ-ray source for divergent pointing cfg2.

C.1.3 cfg4 - div0.01135

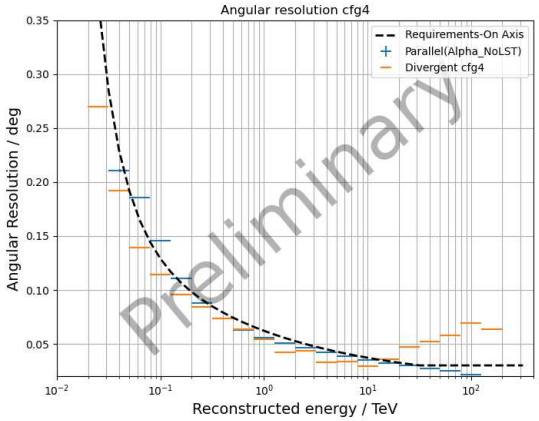

Figure C.9: Angular resolution for cfg4 obtained with `ctapipe`.

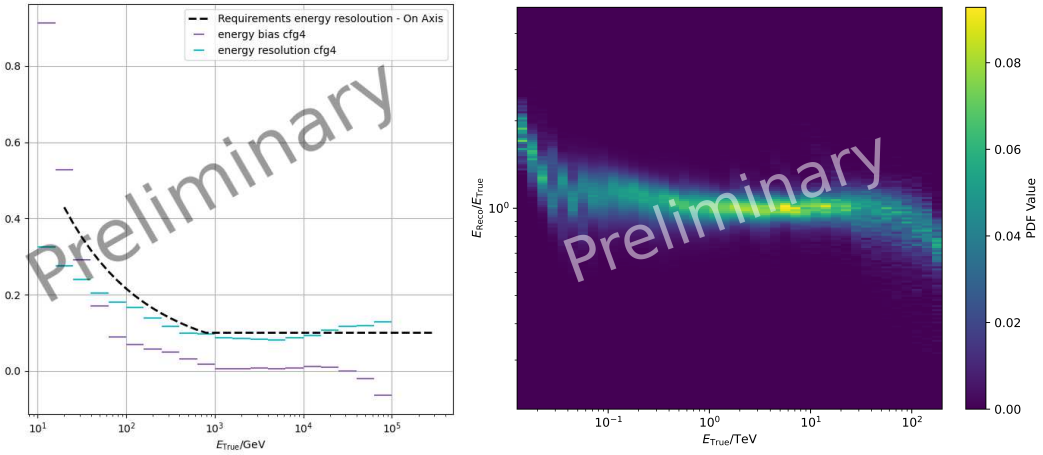

Figure C.10: **Left**: Energy bias and resolution for cfg4. The requirements refer to energy resolution only. **Right**: Energy dispersion relation for divergent pointing configuration cfg4.

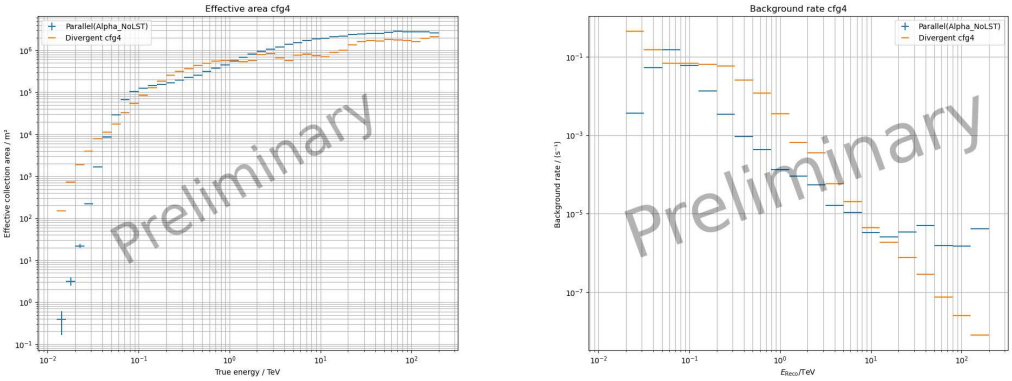

Figure C.11: **Left**: Effective area for divergent pointing configuration cfg4. The comparison is made with CTA requirements and with parallel pointing Southern array in the alpha configuration. **Right**: Background rate for divergent pointing configuration cfg4.

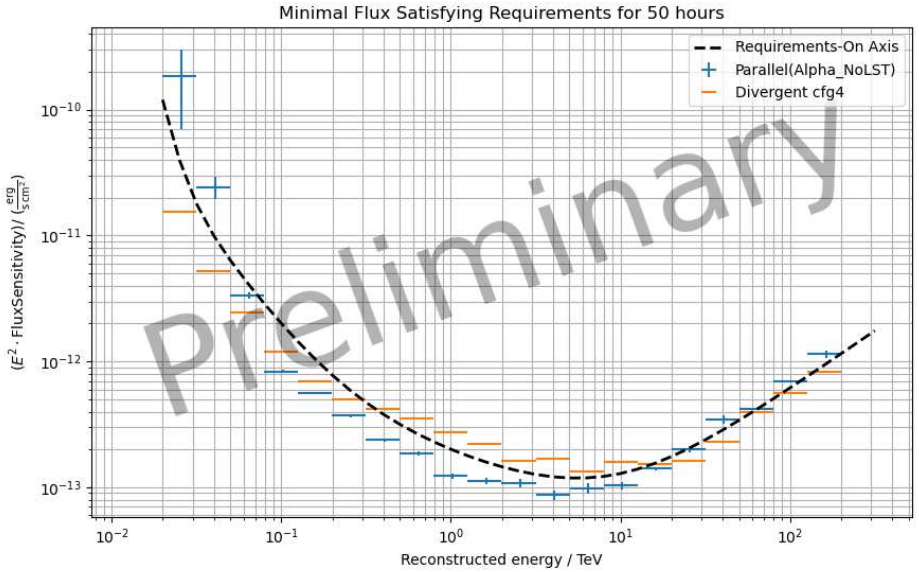

Figure C.12: Sensitivity to an on-axis point-like γ-ray source for divergent pointing cfg4.

C.1.4 cfg5 - div0.01453

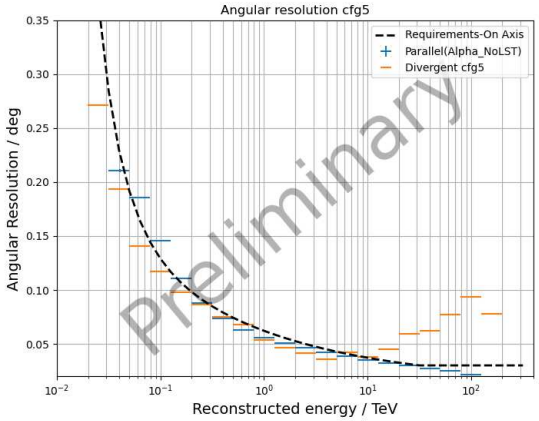

Figure C.13: Angular resolution for cfg5 obtained with `ctapipe`.

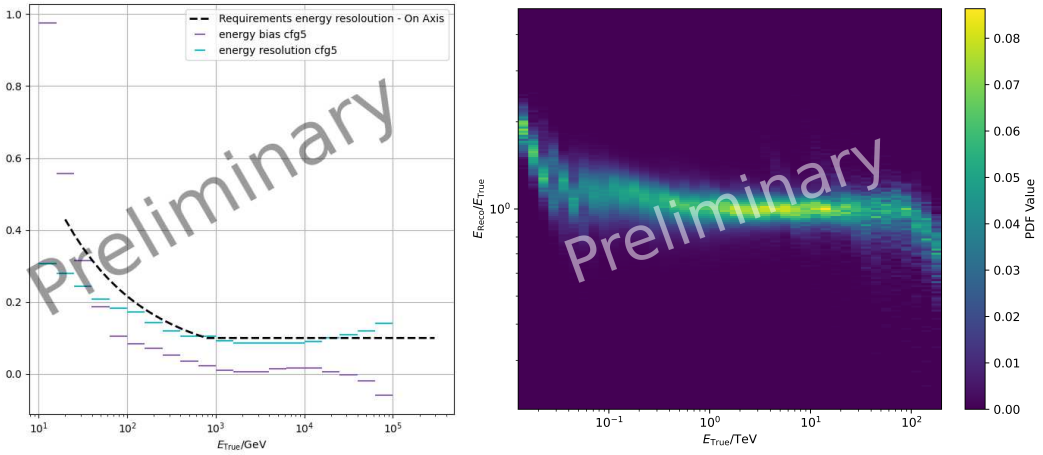

Figure C.14: **Left**: Energy bias and resolution for cfg5. The requirements refer to energy resolution only. **Right**: Energy dispersion relation for divergent pointing configuration cfg5.

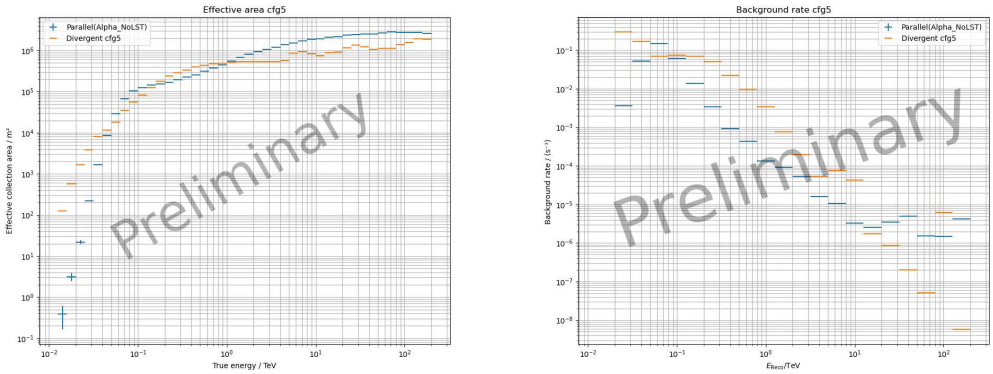

Figure C.15: **Left**: Effective area for divergent pointing configuration cfg5. The comparison is made with CTA requirements and with parallel pointing Southern array in the alpha configuration. **Right**: Background rate for divergent pointing configuration cfg5.

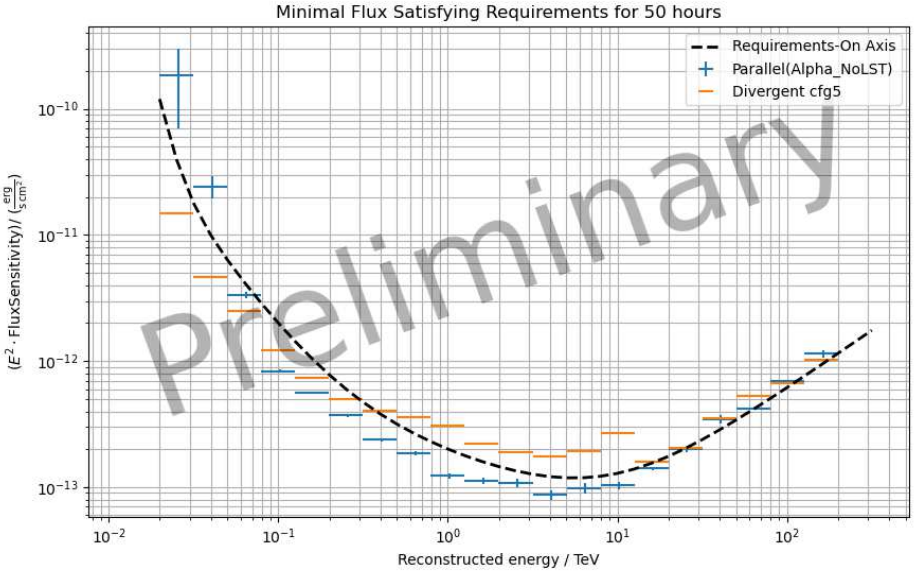

Figure C.16: Sensitivity to an on-axis point-like γ-ray source for divergent pointing cfg5.

C.2 Diffuse performance

C.2.1 cfg1.5 - div0.0022

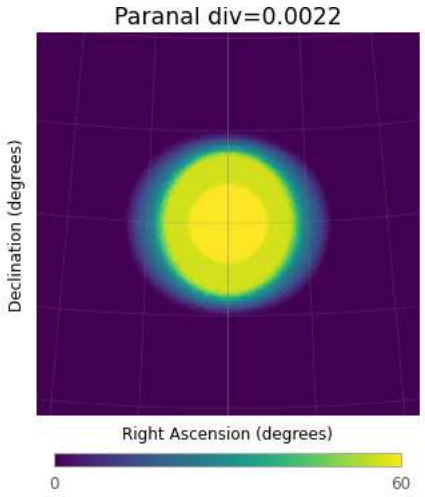

Figure C.17: Geometric HFoV for cfg1.5. The radius of the reported circles is used as a reference to select the maximum radius up to which the performance is computed for primary diffuse gammas.

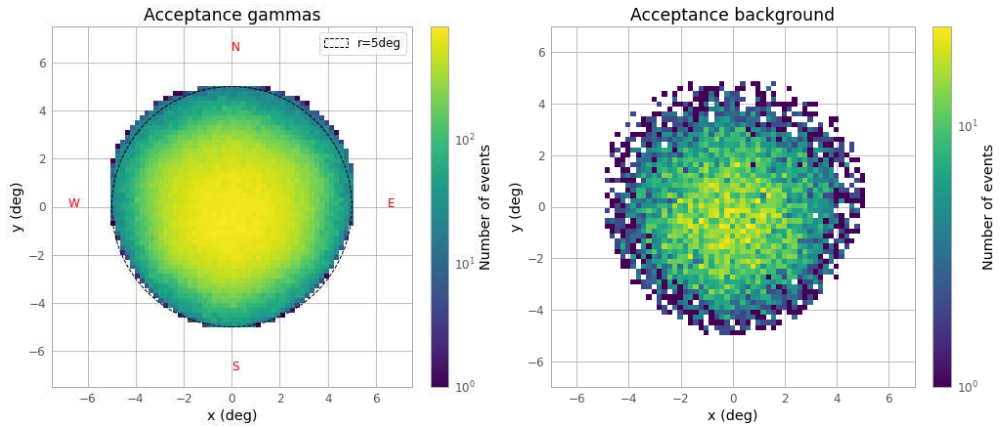

Figure C.18: Acceptance maps of gammas (left) and background (right) for divergent cfg1.5. The acceptance is computed up to a distance of 6deg from the center of the FoV, distance which is marked with a circle in the gamma's plot. The same plot also reports four letters marking the directions along which the symmetry of the FoV is checked.

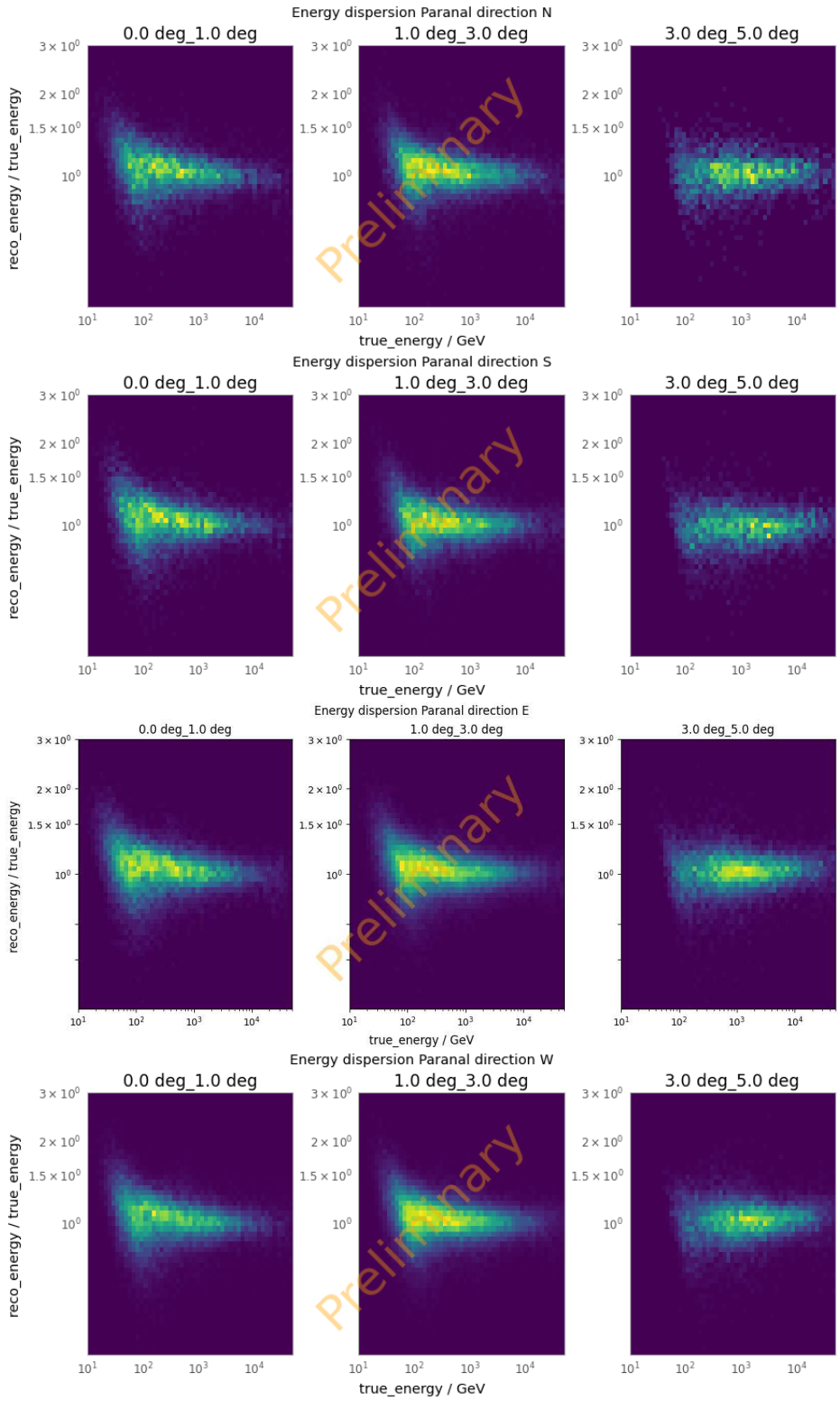

Figure C.19: Evolution of energy dispersion with growing distance from the center of the FoV for divergent cfg1.5. Each line refers to one of the directions reported in Figure C.18.

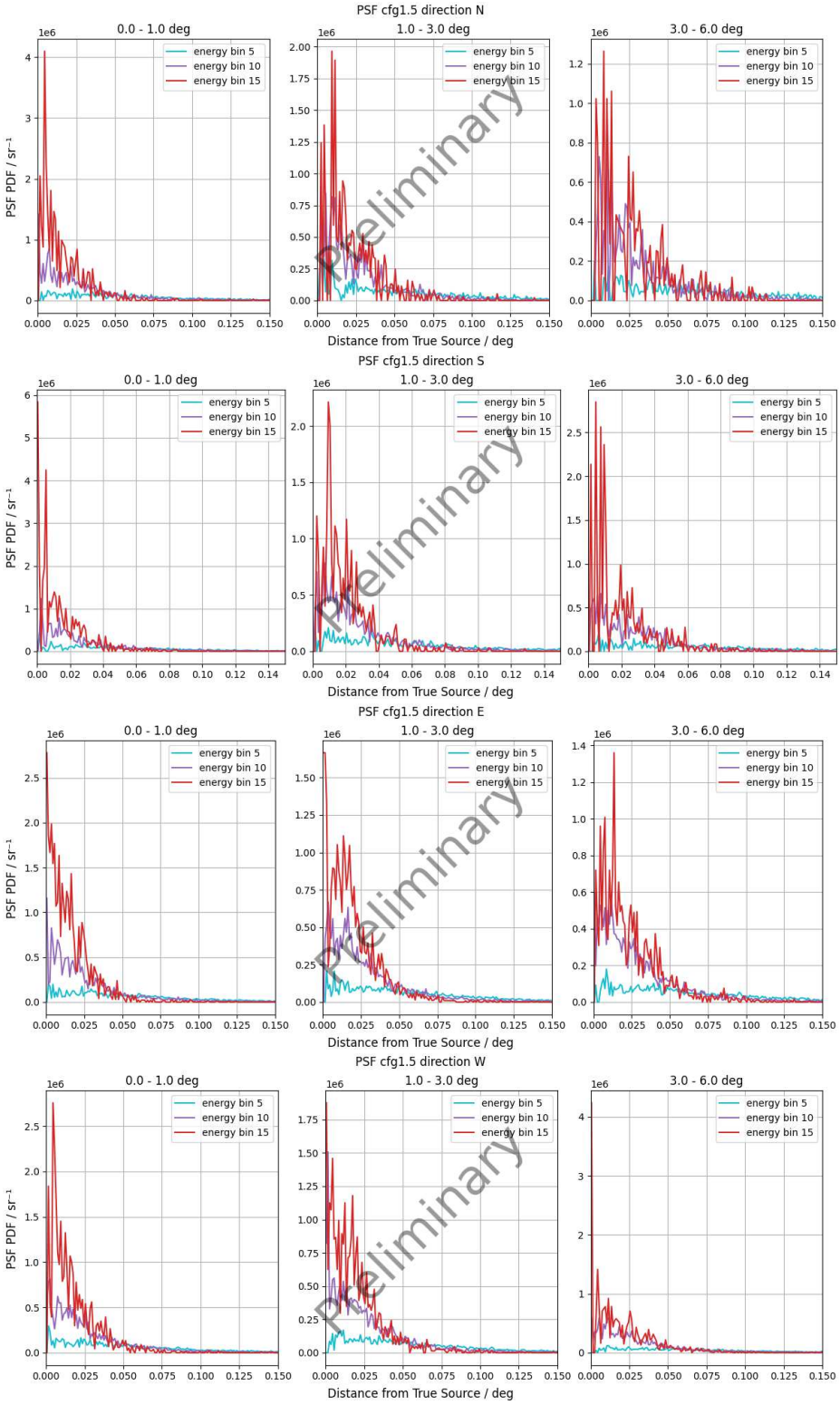

Figure C.20: Evolution of PSF with growing distance from the center of the FoV for divergent pointing cfg1.5. Each line refers to one of the directions reported in Figure C.18.

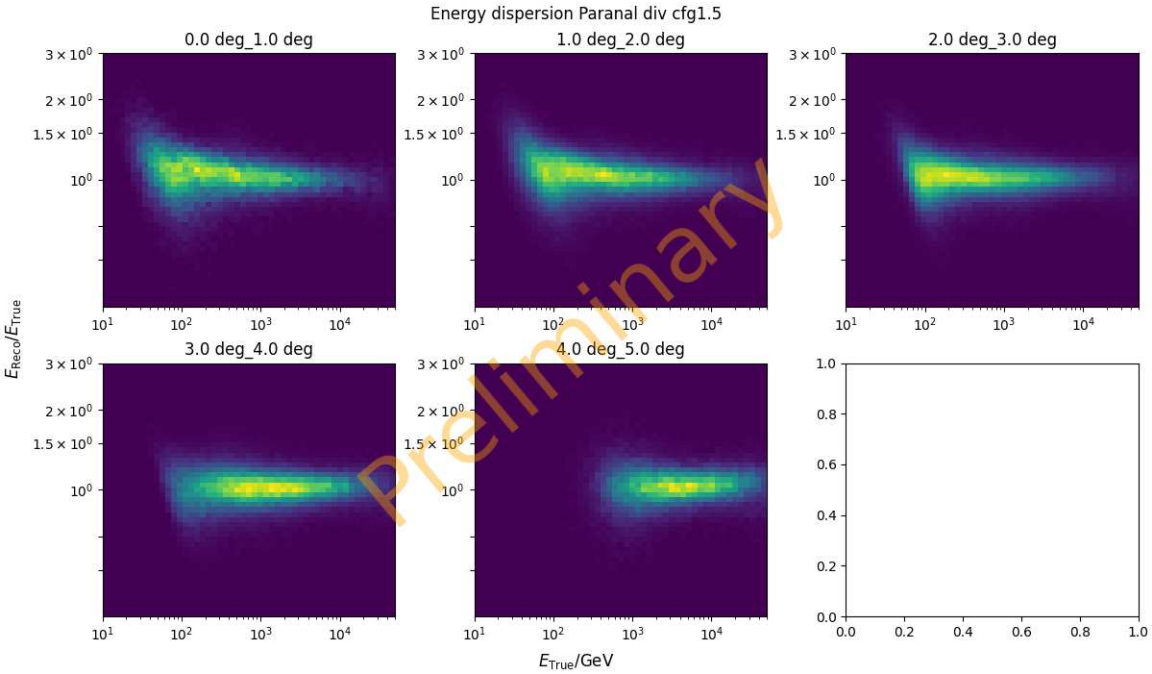

Figure C.21: Energy regression for cfg1.5 at different distances from FoV center.

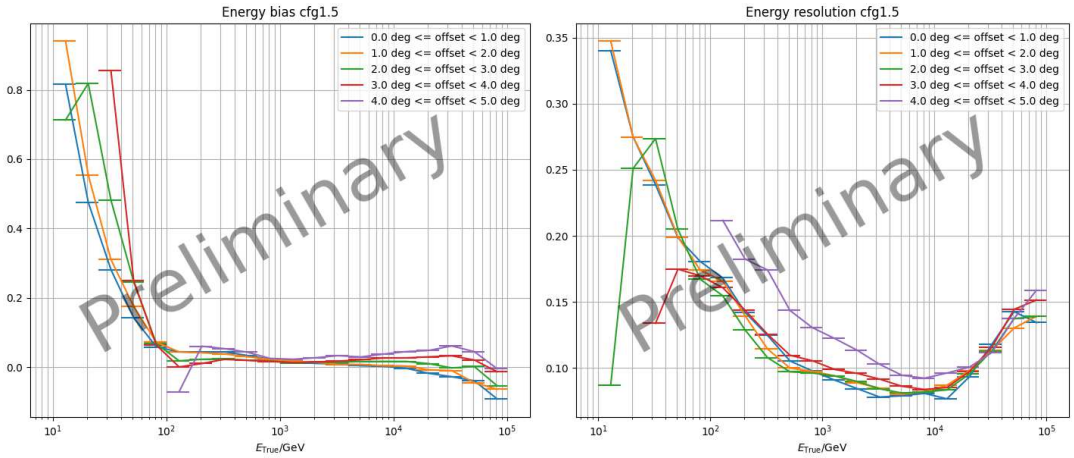

Figure C.22: Energy bias and resolution for cfg1.5 at different distances from FoV center.

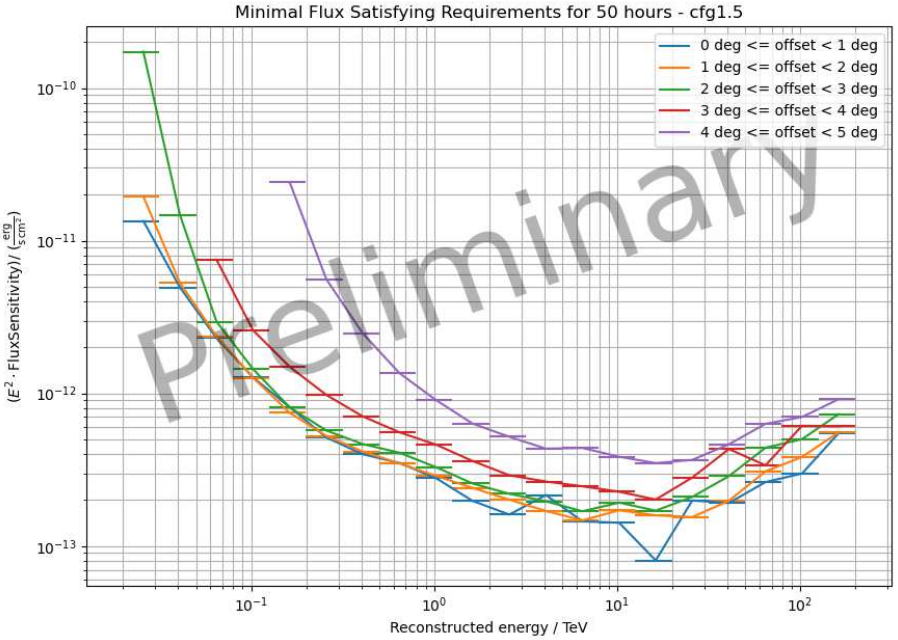

Figure C.23: Sensitivity curves for cfg1.5 in different bins of distance from the FoV center.

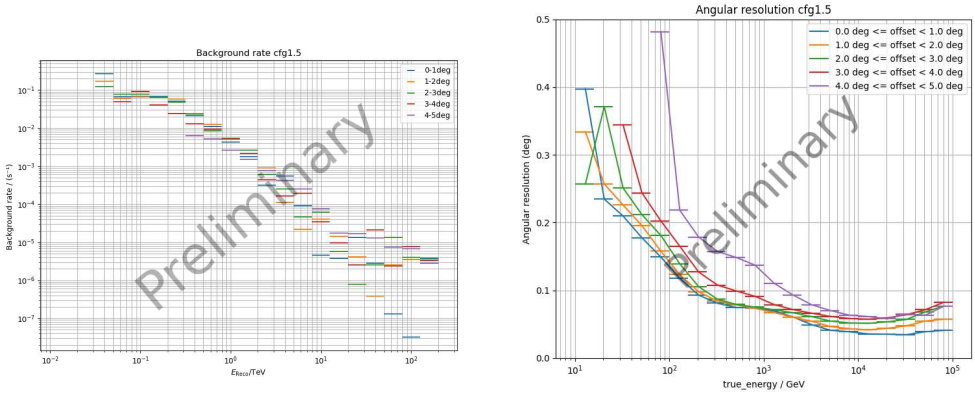

Figure C.24: **Left**: Background rate for cfg1.5 computed in different distance bins form the center of the Fov. **Right**: Angular resolution at different distances from the hFoV center for cfg1.5.

C.2.2 cfg2 - div0.0043

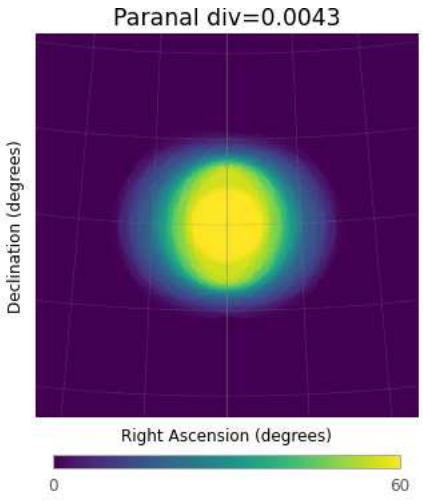

Figure C.25: Geometric HFoV for cfg2. The radius of the reported circles is used as a reference to select the maximum radius up to which the performance is computed for primary diffuse gammas.

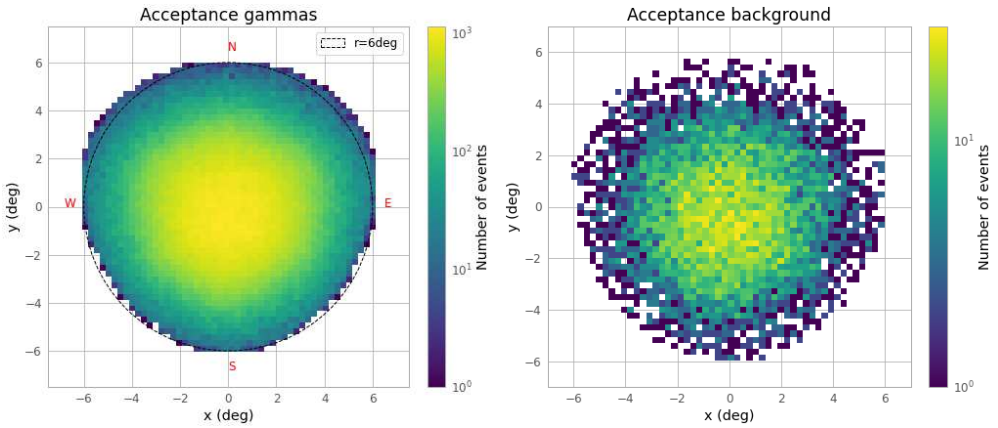

Figure C.26: Acceptance maps of gammas (left) and background (right) for divergent cfg2. The acceptance is computed up to a distance of 6deg from the center of the FoV, distance which is marked with a circle in the gamma's plot. The same plot also reports four letters marking the directions along which the symmetry of the FoV is checked.

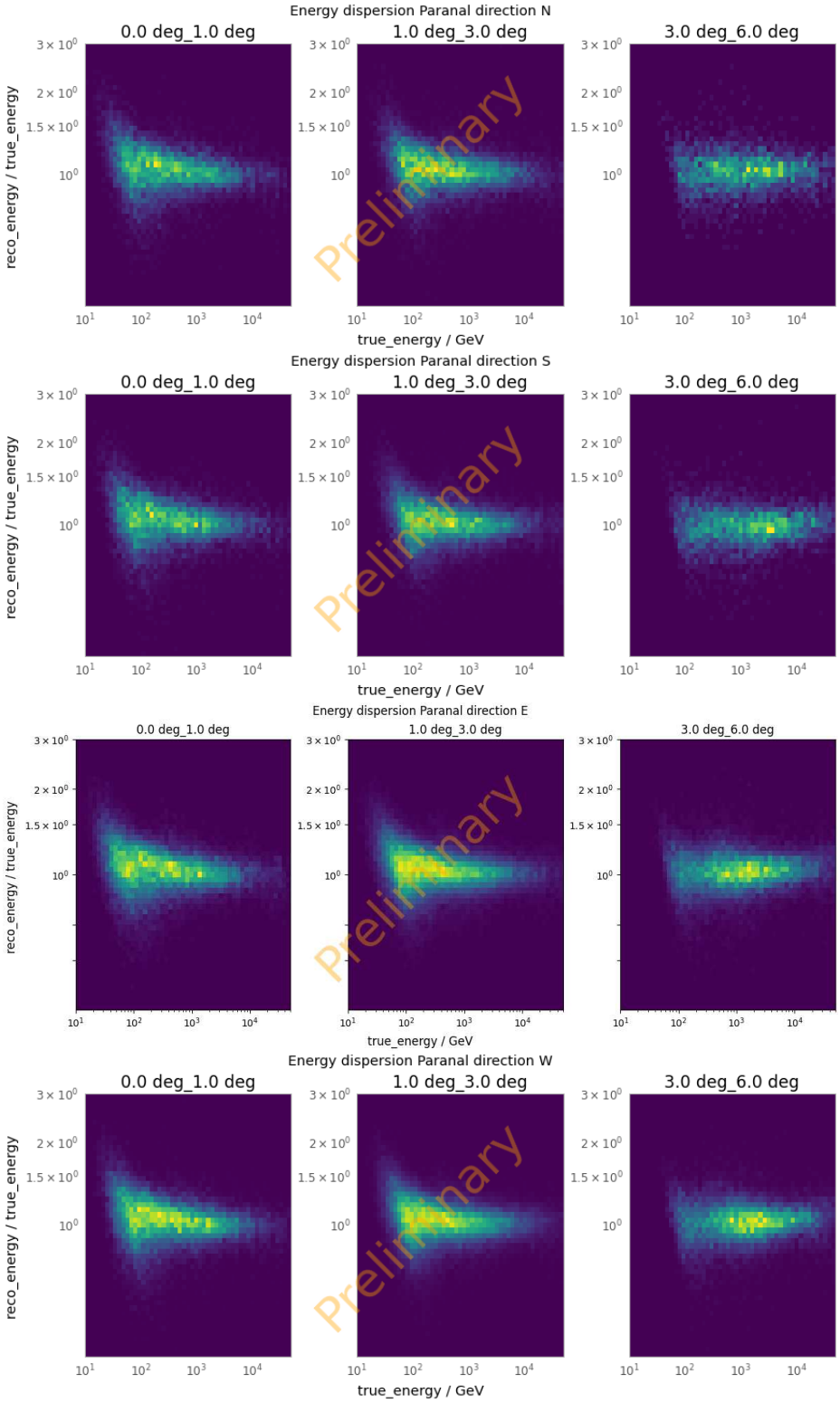

Figure C.27: Evolution of energy dispersion with growing distance from the center of the FoV for divergent cfg2. Each line refers to one of the directions reported in Figure C.26.

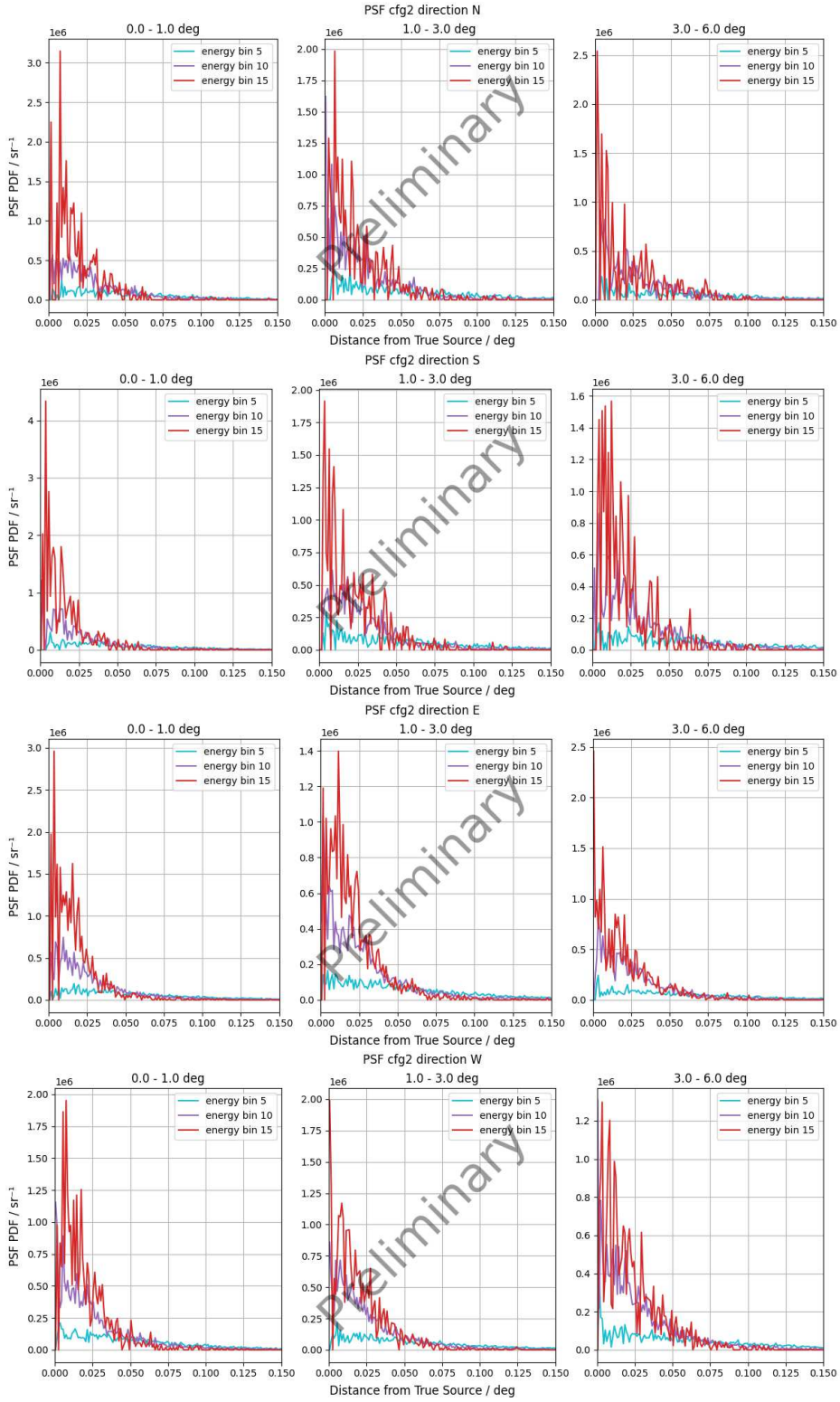

Figure C.28: Evolution of PSF with growing distance from the center of the FoV for divergent pointing cfg2. Each line refers to one of the directions reported in Figure C.26.

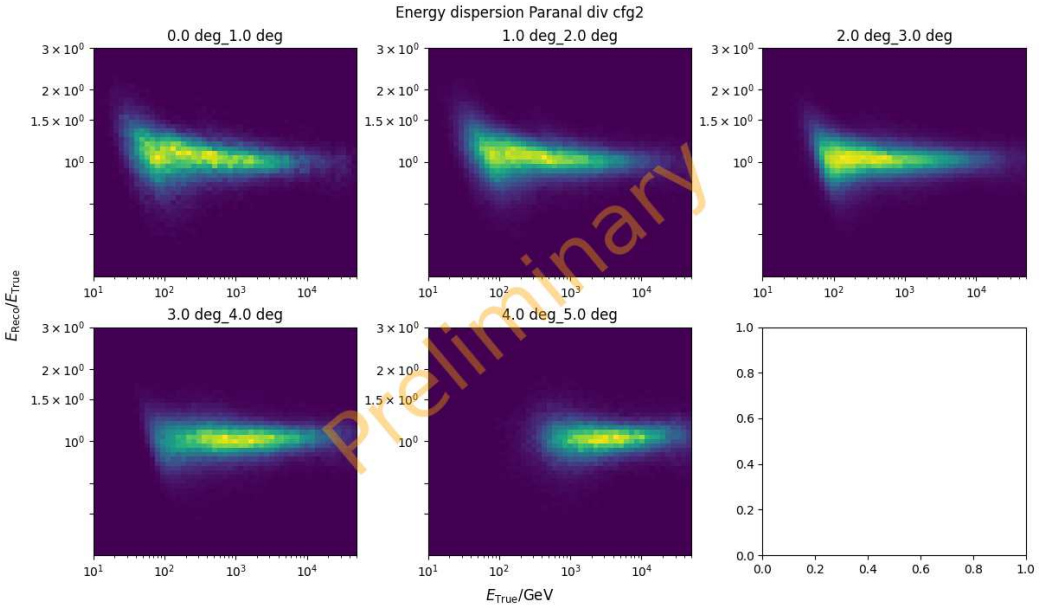

Figure C.29: Energy regression for cfg2 at different distances from FoV center.

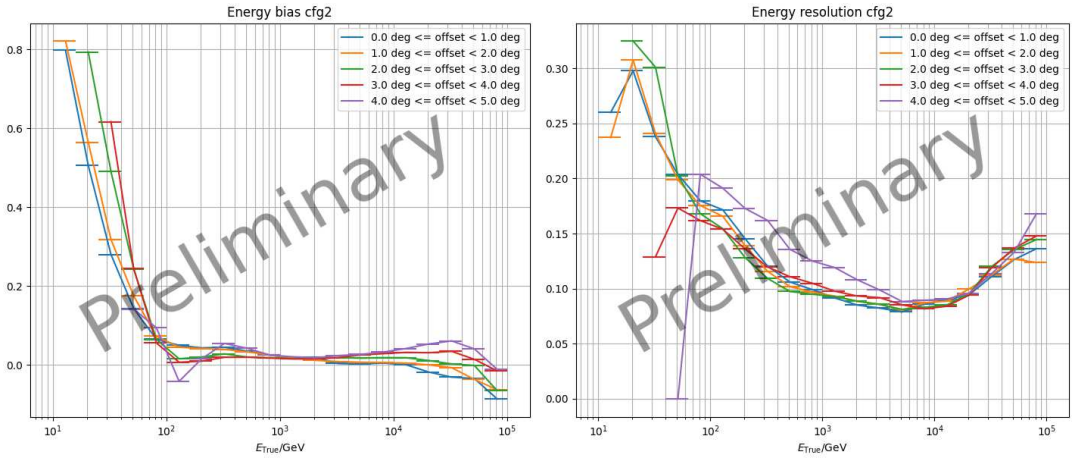

Figure C.30: Energy bias and resolution for cfg2 at different distances from FoV center.

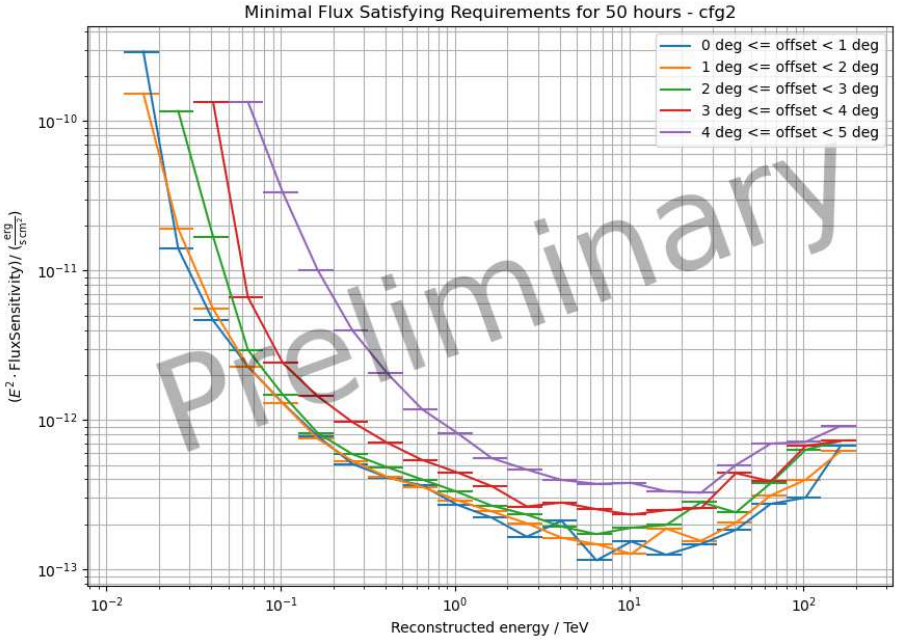

Figure C.31: Sensitivity curve for cfg2 in different bins of distance from the FoV center.

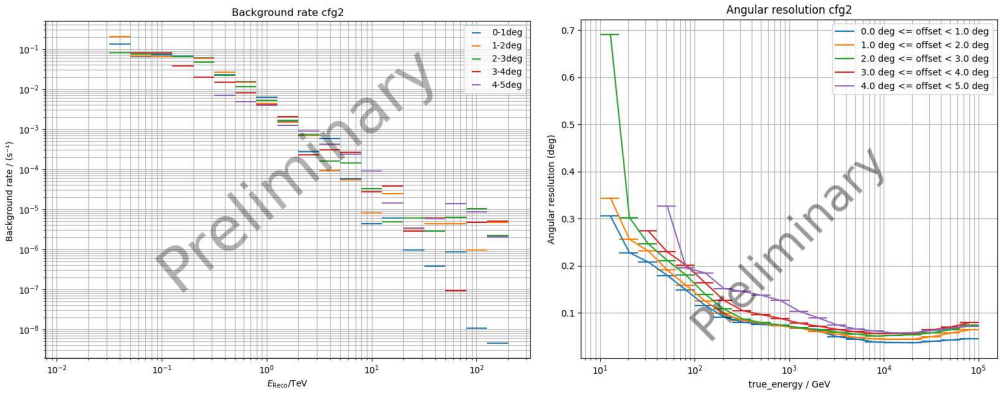

Figure C.32: **Left**: Background rate for cfg2 computed in different distance bins form the center of the Fov. **Right**: Angular resolution at different distances from the hFoV center for cfg2.

C.2.3 cfg4 - div0.01135

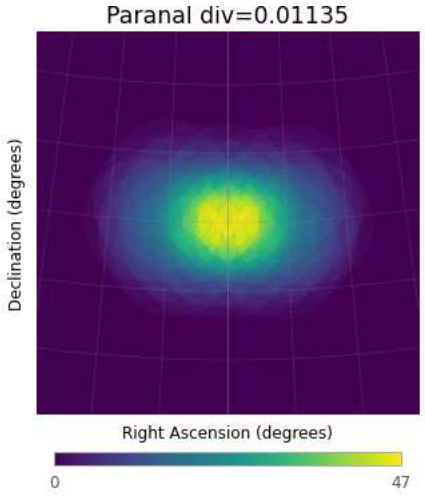

Figure C.33: Geometric HFoV for cfg4. The radius of the reported circles is used as a reference to select the maximum radius up to which the performance is computed for primary diffuse gammas.

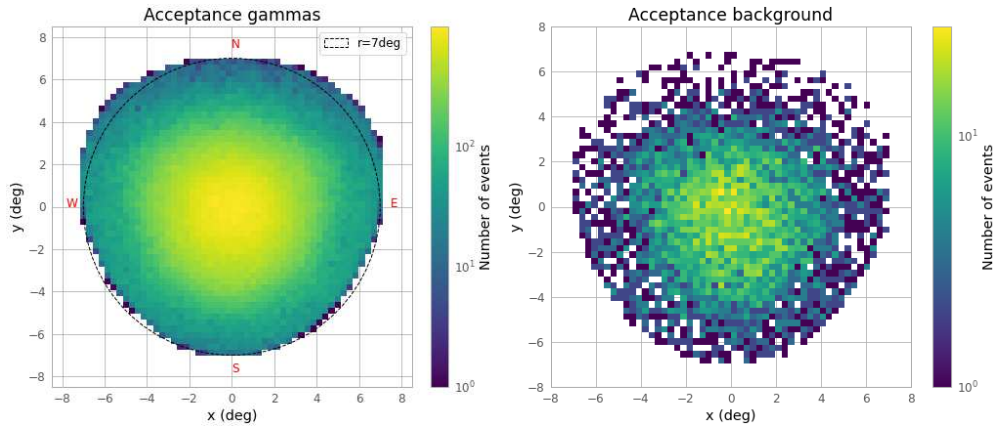

Figure C.34: Acceptance maps of gammas (left) and background (right) for divergent cfg4. The acceptance is computed up to a distance of 6deg from the center of the FoV, distance which is marked with a circle in the gamma's plot. The same plot also reports four letters marking the directions along which the symmetry of the FoV is checked.

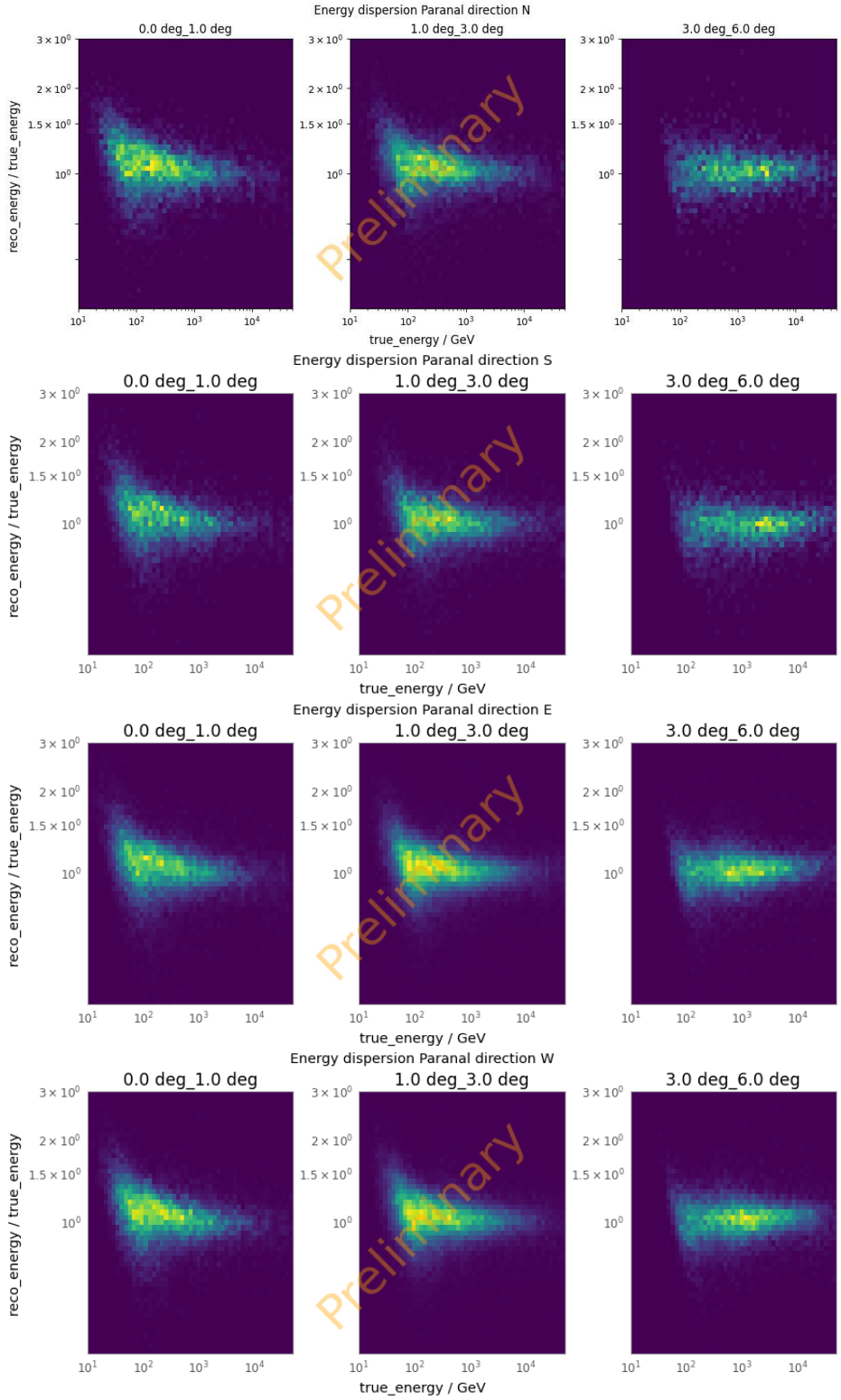

Figure C.35: Evolution of energy dispersion with growing distance from the center of the FoV for divergent cfg4. Each line refers to one of the directions reported in Figure C.34.

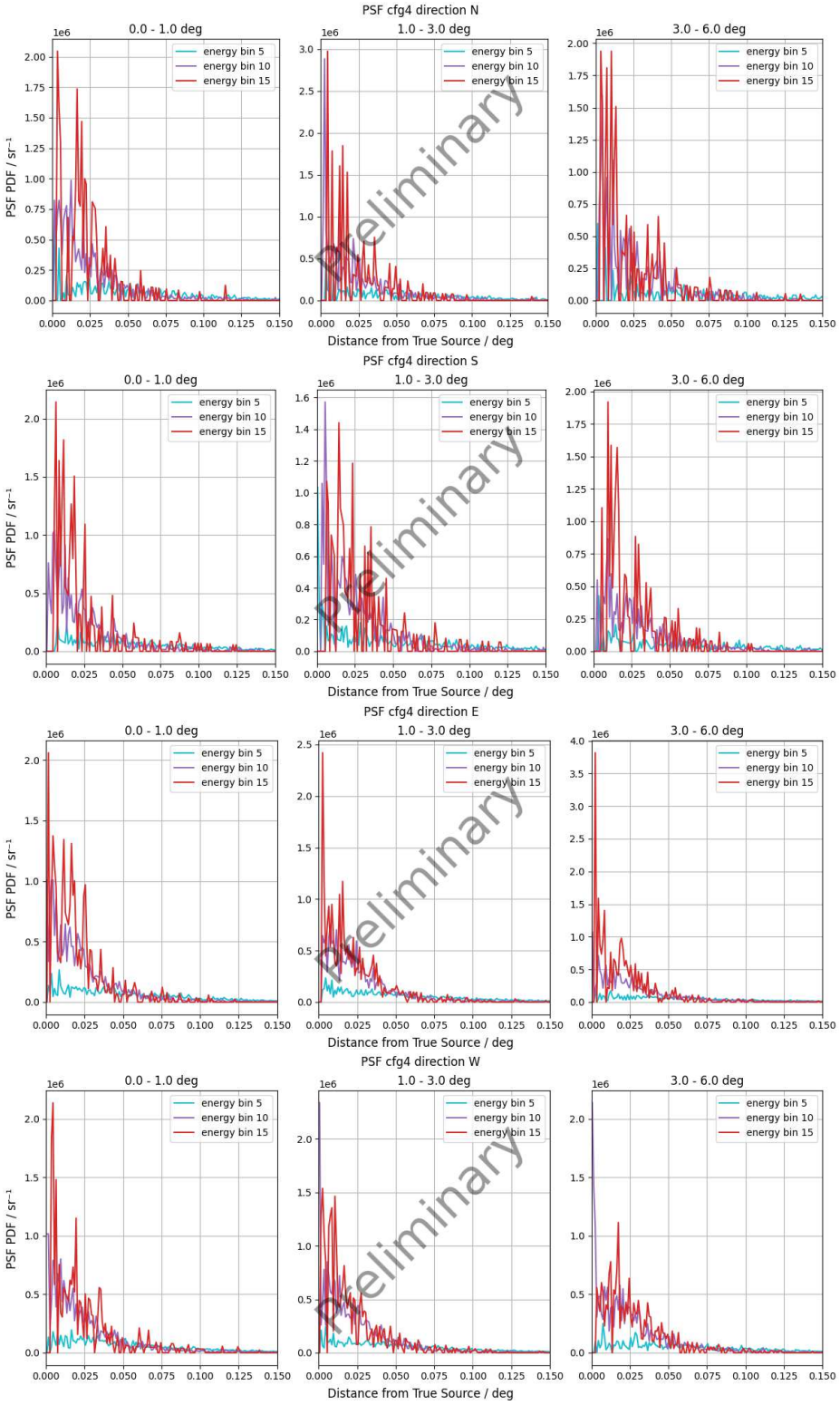

Figure C.36: Evolution of PSF with growing distance from the center of the FoV for divergent pointing cfg4. Each line refers to one of the directions reported in Figure C.34.

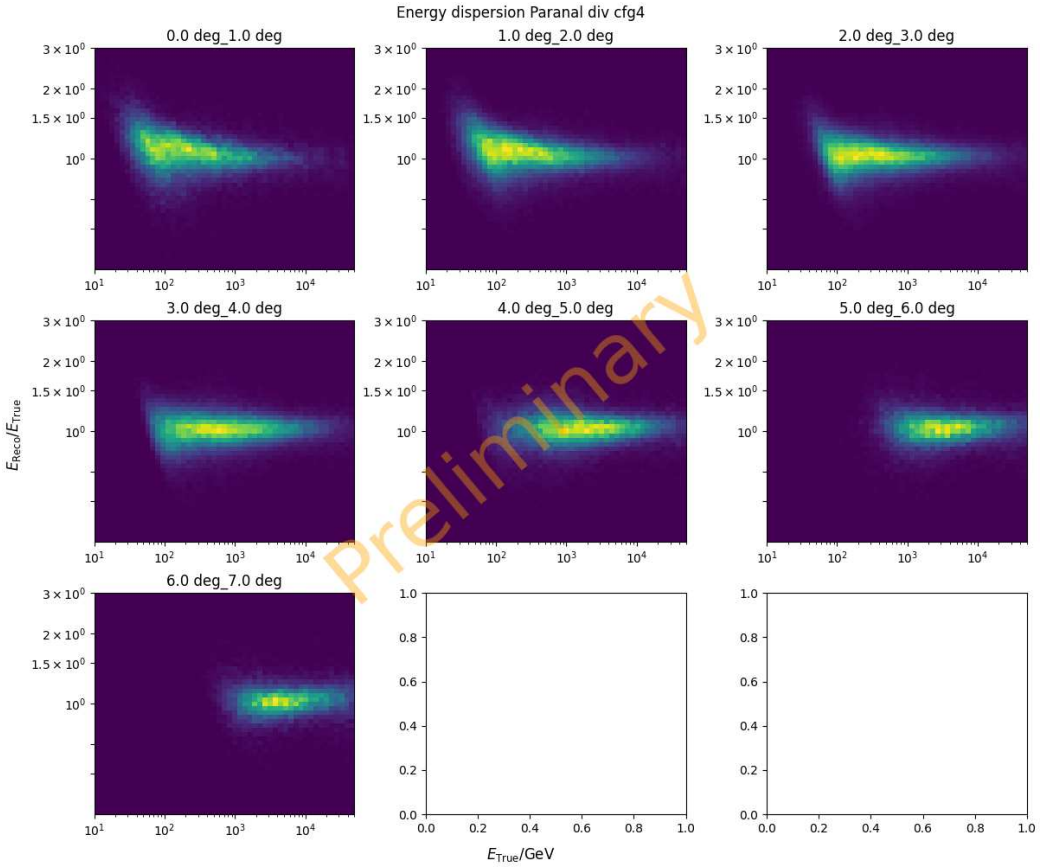

Figure C.37: Energy regression for cfg4 at different distances from FoV center.

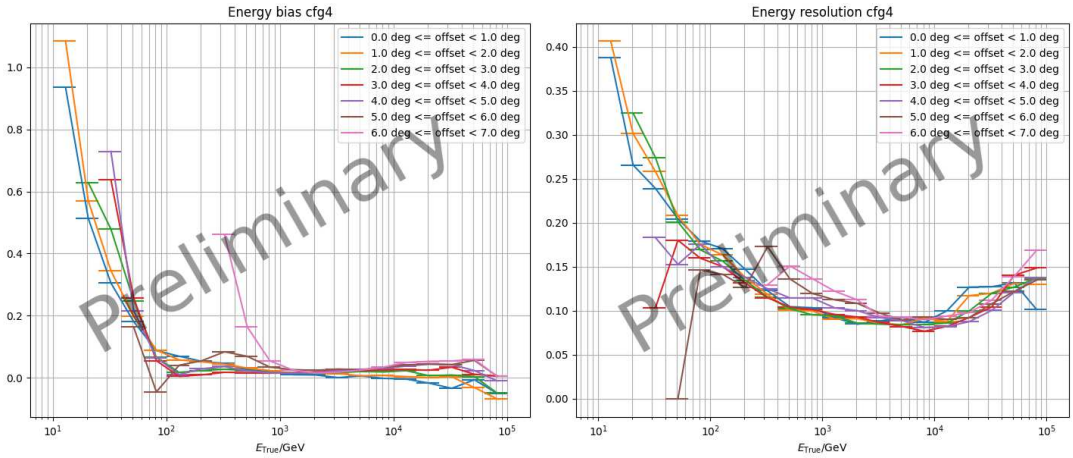

Figure C.38: Energy bias and resolution for cfg4 at different distances from FoV center.

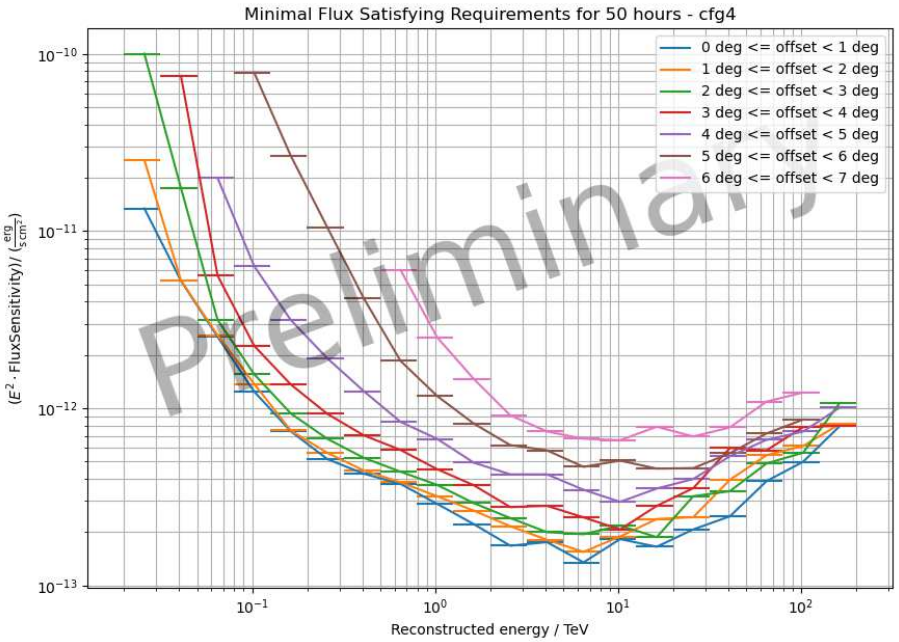

Figure C.39: Sensitivity curve for cfg4 in different bins of distance from the FoV center.

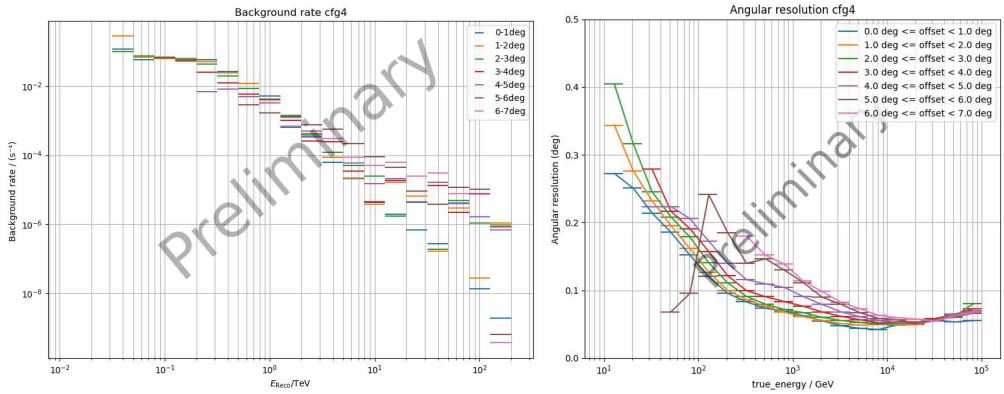

Figure C.40: **Left**: Background rate for cfg4 computed in different distance bins form the center of the Fov. **Right**: Angular resolution at different distances from the hFoV center for cfg4.

C.2.4 cfg5 - div0.01453

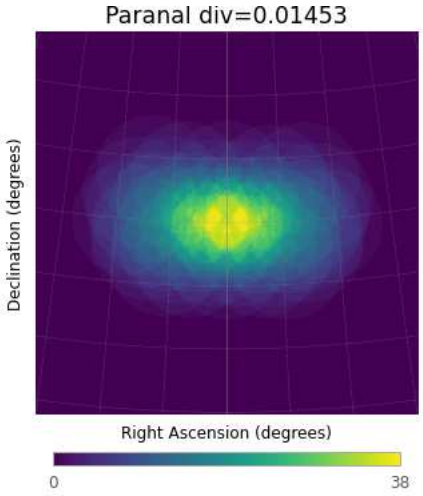

Figure C.41: Geometric HFoV for cfg5. The radius of the reported circles is used as a reference to select the maximum radius up to which the performance is computed for primary diffuse gammas.

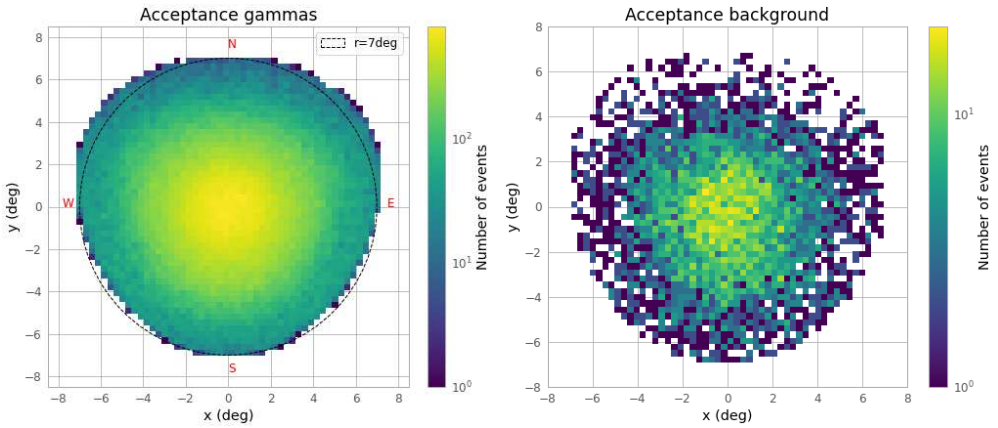

Figure C.42: Acceptance maps of gammas (left) and background (right) for divergent cfg5. The acceptance is computed up to a distance of 6deg from the center of the FoV, distance which is marked with a circle in the gamma's plot. The same plot also reports four letters marking the directions along which the symmetry of the FoV is checked.

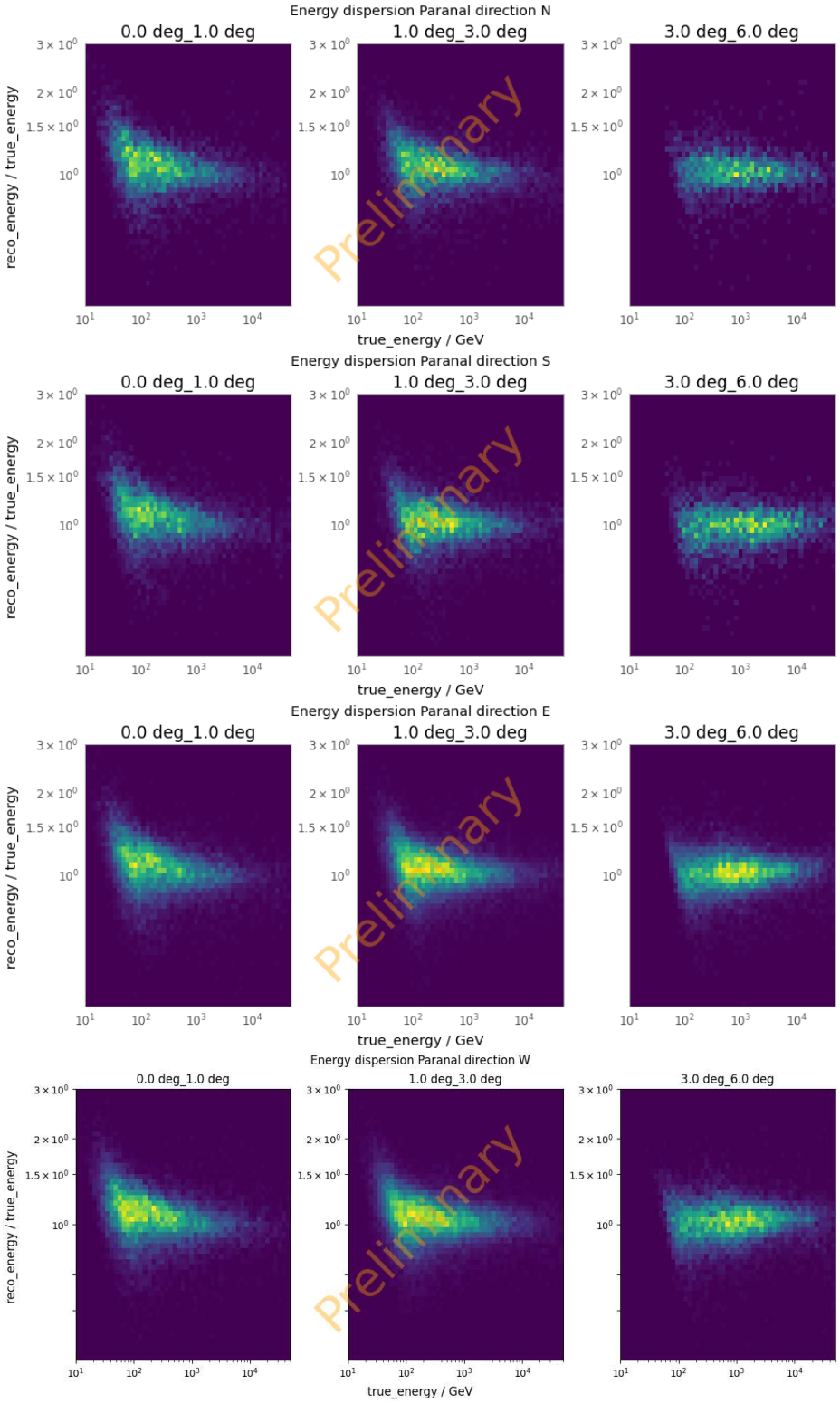

Figure C.43: Evolution of energy dispersion with growing distance from the center of the FoV for divergent cfg5. Each line refers to one of the directions reported in Figure C.42.

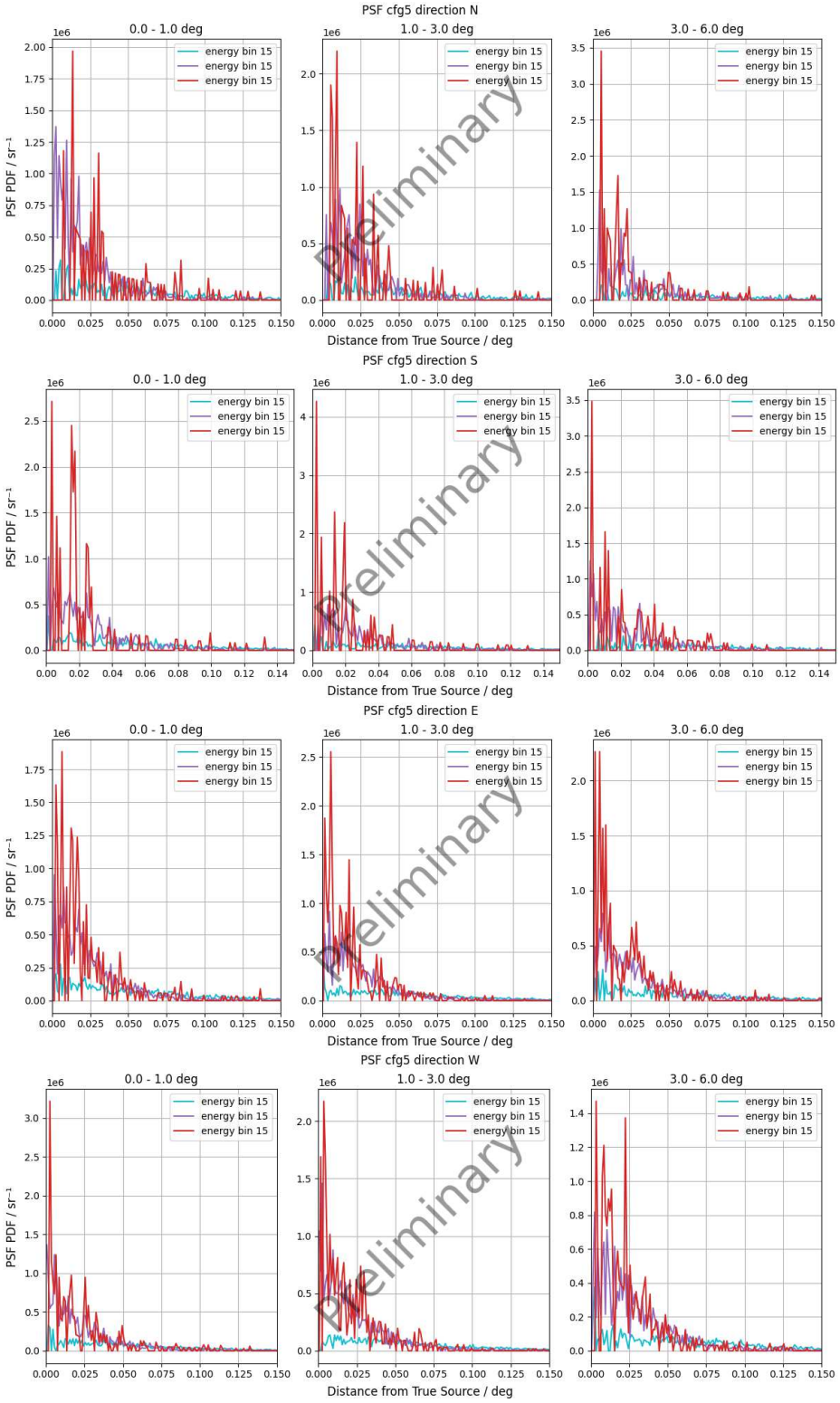

Figure C.44: Evolution of PSF with growing distance from the center of the FoV for divergent pointing cfg5. Each line refers to one of the directions reported in Figure C.42.

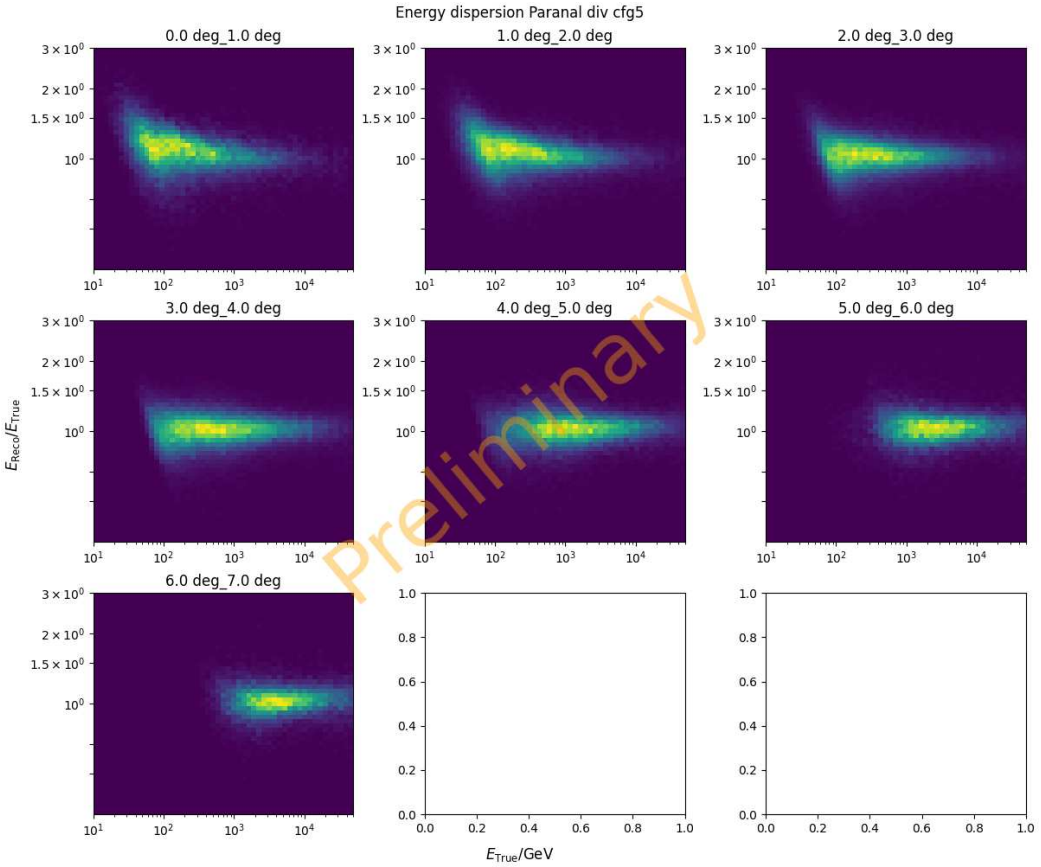

Figure C.45: Energy regression for cfg5 at different distances from FoV center.

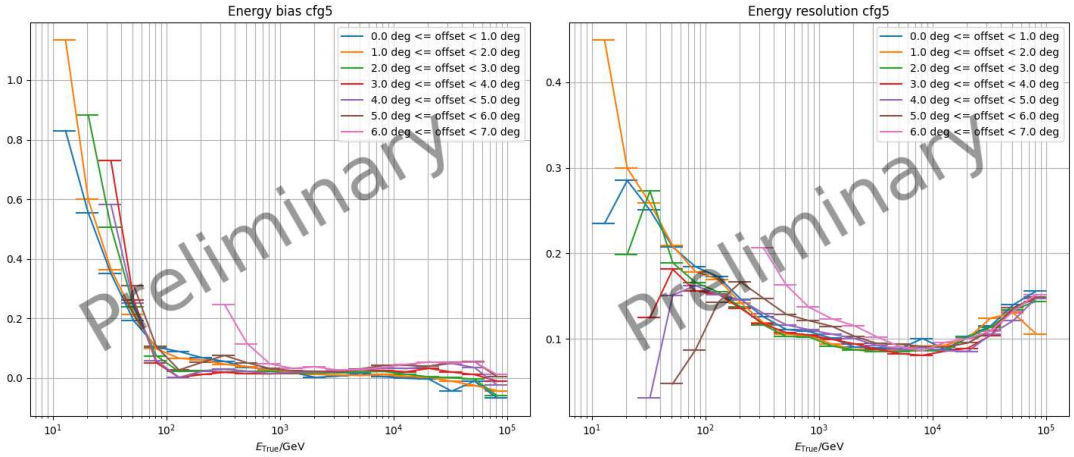

Figure C.46: Energy bias and resolution for cfg5 at different distances from FoV center.

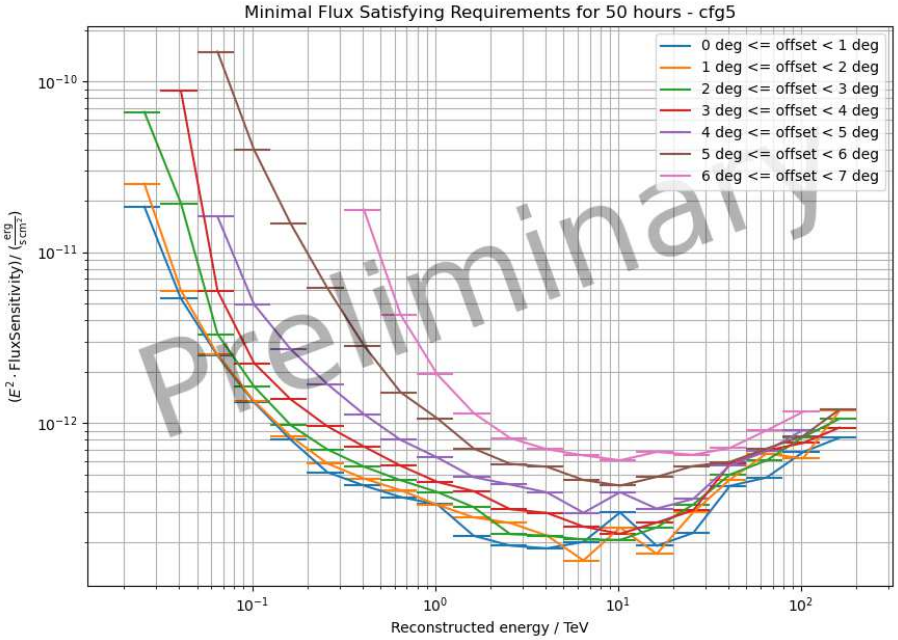

Figure C.47: Sensitivity curves for cfg5 in different bins of distance from the FoV center.

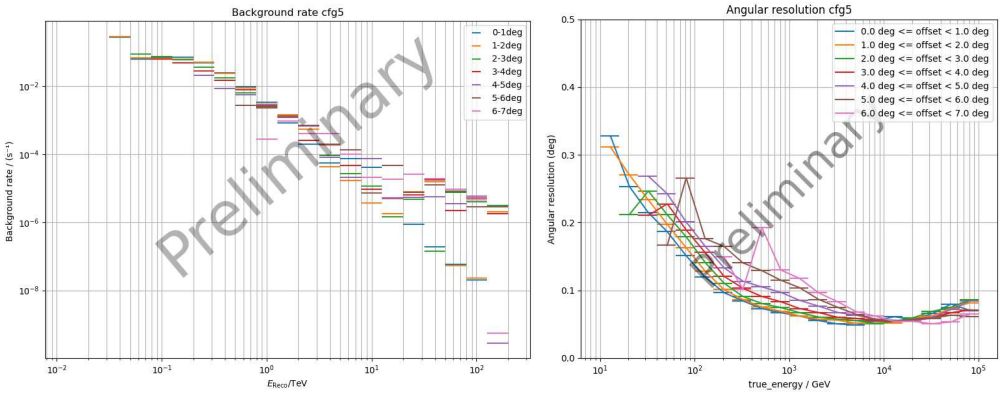

Figure C.48: **Left**: Background rate for cfg5 computed in different distance bins form the center of the Fov. **Right**: Angular resolution at different distances from the hFoV center for cfg5.

Bibliography

1. Abbott, B. P. *et al. Astrophysical Journal Letters* **848,** L13. arXiv: 1710.05834 [astro-ph.HE] (Oct. 2017).
2. Abbott, B. P. *et al. Physical Review Letters* **119,** 161101. arXiv: 1710.05832 [gr-qc] (Oct. 2017).
3. Abdalla, H. *et al. Nature* **575,** 464–467. arXiv: 1911.08961 [astro-ph.HE] (Nov. 2019).
4. Abe, H. *et al.* in *Proceedings of 37th International Cosmic Ray Conference — PoS(ICRC2021)* **395** (2021), 838.
5. Abeysekara, A. U. *et al. Astroparticle Physics* **50,** 26–32. arXiv: 1306.5800 [astro-ph.HE] (Dec. 2013).
6. Abeysekara, A. *et al. Astroparticle Physics* **35,** 641–650. ISSN: 0927-6505 (2012).
7. Acciari, V. A. *et al. Astrophysical Journal* **908,** 90. arXiv: 2012.07193 [astro-ph.HE] (Feb. 2021).
8. Acero, F. *et al. Astroparticle Physics* **150,** 102850 (Aug. 2023).
9. Acharyya, A. *et al. Monthly Notices of the Royal Astronomical Society* **523,** 5353–5387 (May 2023).
10. Aharonian, F., Buckley, J., Kifune, T. & Sinnis, G. *Reports on Progress in Physics* **71,** 096901 (Sept. 2008).
11. Aharonian, F. *et al. Astrophysical Journal* **614,** 897–913. arXiv: astro-ph/0407118 [astro-ph] (Oct. 2004).
12. Aharonian, F. *et al. Astronomy & Astrophysics* **503,** 817–825. arXiv: 0906.1247 [astro-ph.GA] (Sept. 2009).
13. Aharonian, F. A. *et al. Astronomy & Astrophysics* **375,** 1008–1017 (Sept. 2001).
14. Aharonian, F. A. *et al. Astronomy & Astrophysics* **395,** 803–811. arXiv: astro-ph/0209360 [astro-ph] (Dec. 2002).
15. Aielli, G. *et al. Nuclear Instruments and Methods in Physics Research A* **562,** 92–96 (June 2006).
16. Albert, J. *et al. Astrophysical Journal* **674,** 1037–1055. arXiv: 0705.3244 [astro-ph] (Feb. 2008).

17. Aleksić, J. *et al. Astroparticle Physics* **72,** 61–75. arXiv: 1409.6073 [astro-ph.IM] (Jan. 2016).
18. Aleksić, J. *et al. Astroparticle Physics* **72,** 76–94 (Jan. 2016).
19. Amenomori, M. *et al. Astrophysical Journal Letters* **525,** L93–L96. arXiv: astro-ph/9909172 [astro-ph] (Nov. 1999).
20. Archer, A. *et al. Astrophysical Journal* **790,** 149. arXiv: 1406.6383 [astro-ph.HE] (Aug. 2014).
21. Ashkar, H. *et al. Journal of Cosmology and Astroparticle Physics* **2021,** 045. arXiv: 2010.16172 [astro-ph.HE] (Mar. 2021).
22. Astropy Collaboration *et al. The Astronomical Journal* **156,** 123 (Aug. 2018).
23. Atkins, R. *et al. Astrophysical Journal* **595,** 803–811. arXiv: astro-ph/0305308 [astro-ph] (Oct. 2003).
24. Band, D. *et al. Astrophysical Journal* **413,** 281 (Aug. 1993).
25. Bartos, I. *et al. Monthly Notices of the Royal Astronomical Society* **477,** 639–647. arXiv: 1802.00446 [astro-ph.HE] (June 2018).
26. Bernlöhr, K. *et al. Astroparticle Physics* **43,** 171–188. arXiv: 1210.3503 [astro-ph.IM] (Mar. 2013).
27. Bernlöhr, K. *Astroparticle Physics* **30,** 149–158. arXiv: 0808.2253 [astro-ph] (Oct. 2008).
28. Bernlöhr, K. *Astroparticle Physics* **30,** 149–158. arXiv: 0808.2253 [astro-ph] (Oct. 2008).
29. Bernlöhr, K., Maier, G. & Moralejo, A. Version 1.0.0 (Zenodo, Feb. 2022).
30. Blanch, O. *et al. GRB Coordinates Network* **28659,** 1 (Oct. 2020).
31. Blanch, O. *The Astronomer's Telegram* **14275,** 1 (Dec. 2020).
32. Blumental, G. R. & Gould, R. J. *Reviews of Modern Physics* **42,** 237–270 (2 Apr. 1970).
33. Cao, Z. *et al. arXiv e-prints,* arXiv:1905.02773. arXiv: 1905.02773 [astro-ph.HE] (May 2019).
34. Cao, Z. *et al. Nature* **594,** 33–36 (June 2021).
35. Cerenkov, P. A. *Physics Review* **52,** 378–379 (1937).
36. Cherenkov, P. A. *Dokl. Akad. Nauk SSSR* **2,** 451–454 (1934).
37. Cherenkov Telescope Array Consortium *et al.* (2019).
38. Cherenkov Telescope Array Observatory & Cherenkov Telescope Array Consortium. Version v0.1 (Zenodo, Sept. 2021).
39. Costa, E. *et al. Nature* **387,** 783–785. arXiv: astro-ph/9706065 [astro-ph] (June 1997).

40. CTA-LST Project *et al.* in *Proceedings of 37th International Cosmic Ray Conference — PoS(ICRC2021)* (Mar. 2022), 838.
41. CTA-LST Project *et al. arXiv e-prints,* arXiv:2306.12960. arXiv: 2306.12960 [astro-ph.HE] (June 2023).
42. CTA-Observatory. (accessed: 2022-18-10).
43. CTAO Observatory Press release. *CTAO News* (2021).
44. de Naurois, M. & H. E. S. S. Collaboration. *GRB Coordinates Network* **25566,** 1 (Aug. 2019).
45. Deil, C. *et al.* in *Proceedings of 35th International Cosmic Ray Conference — PoS(ICRC2017)* **301** (July 2017), 766. arXiv: 1709.01751 [astro-ph.IM].
46. Deil, C. *et al.* in *6th International Symposium on High Energy Gamma-Ray Astronomy* **1792** (Jan. 2017), 070006. arXiv: 1610.01884 [astro-ph.IM].
47. Deil, C. *et al.* (Sept. 2018).
48. Doll, P. *et al. Verh. Dtsch. Phys. Ges* **25,** 1388 (Jan. 1990).
49. Donini, A. PhD thesis (Univerità degli Studi di Udine, 2020).
50. Dubus, G. *et al. Astroparticle Physics* **43,** 317–330. ISSN: 0927-6505 (2013).
51. DuVernois, M. A. & Di Sciascio, G. in *Handbook of X-ray and Gamma-ray Astrophysics. Edited by Cosimo Bambi and Andrea Santangelo* 21 (2022).
52. Fermi, E. *Astrophysical Journal* **119,** 1 (Jan. 1954).
53. Fermi, E. *Physics Review* **75,** 1169–1174 (Apr. 1949).
54. Fienberg, A. T. *et al. Nuclear Instruments and Methods in Physics Research A* **783,** 12–21. arXiv: 1412.5525 [physics.ins-det] (May 2015).
55. Fomin, V. P. *et al. Astroparticle Physics* **2,** 137–150 (May 1994).
56. Frank, I. M. & Tamm, I. E. *Compt. Rend. Acad. Sci. URSS* **14,** 109–114 (1937).
57. Galama, T. J. *et al. Nature* **395,** 670–672. arXiv: astro-ph/9806175 [astro-ph] (Oct. 1998).
58. Galbraith, W. & Jelley, J. V. *Nature* **171,** 349–350 (Feb. 1953).
59. Gasparetto, T. PhD thesis (Università degli Studi di Trieste, 2020).
60. Gerard, L. in *Proceedings of 34th International Cosmic Ray Conference — PoS(ICRC2015)* **236** (2016), 725.
61. Giebels, B. & H. E. S. S. Collaboration. *arXiv e-prints,* arXiv:1303.2850. arXiv: 1303.2850 [astro-ph.HE] (Mar. 2013).
62. Greisen, K. *Progress in Cosmic Ray Physics 3* (1956).
63. H. E. S. S. Collaboration *et al. Astronomy & Astrophysics* **612,** A1. arXiv: 1804.02432 [astro-ph.HE] (Apr. 2018).
64. Harris, C. R. *et al. Nature* **585,** 357–362 (Sept. 2020).

65. Heitler, W. (Oxford University Press, Oxford, 1936).
66. HESS Collaboration *et al. Nature* **531,** 476–479. arXiv: 1603.07730 [astro-ph.HE] (Mar. 2016).
67. Hillas, A. M. in *Proceedings of 19th International Cosmic Ray Conference — PoS(ICRC1985)* **3** (Aug. 1985), 445.
68. Hjorth, J. *et al. Nature* **423,** 847–850. arXiv: astro-ph/0306347 [astro-ph] (June 2003).
69. Huang, Y. *et al. GRB Coordinates Network* **32677,** 1 (Oct. 2022).
70. IceCube Collaboration *et al. Science* **361,** eaat1378. arXiv: 1807.08816 [astro-ph.HE] (July 2018).
71. Inoue, S. *et al. Astroparticle Physics* **43,** 252–275 (Mar. 2013).
72. Khélifi, B. *et al.* in *Proceedings of 38th International Cosmic Ray Conference — PoS(ICRC2023)* **444** (2023), 1510.
73. Klebesadel, R. W., Strong, I. B. & Olson, R. A. *Astrophysical Journal Letters* **182,** L85 (June 1973).
74. Kosack, K. *et al.* Version v0.19.3. June 2023.
75. LeBohec, S. *et al. Astrophysical Journal* **539,** 209–215. arXiv: astro-ph/0003265 [astro-ph] (Aug. 2000).
76. Li, T. .-. & Ma, Y. .-. *Astrophysical Journal* **272,** 317–324 (Sept. 1983).
77. Lidvansky, A. *Radiation Physics and Chemistry* **75,** 891–898 (Aug. 2006).
78. Linhoff, M. *et al.* in *Proceedings of 38th International Cosmic Ray Conference — PoS(ICRC2023)* **444** (2023), 703.
79. Longair, M. S. (Cambridge University press, 2011).
80. López-Oramas, A. *et al.* in *Proceedings of 37th International Cosmic Ray Conference — PoS(ICRC2021)* (Sissa Medialab, July 2021).
81. LST team for the CTA Consortium. Internal document available at https://www.lst1.iac.es/. 2019.
82. MAGIC Collaboration *et al. Nature* **575,** 455–458. arXiv: 2006.07249 [astro-ph.HE] (Nov. 2019).
83. Masuda, S. *et al.* in *Proceedings of 34th International Cosmic Ray Conference — PoS(ICRC2015)* **34** (July 2015), 1003. arXiv: 1509.00548 [astro-ph.IM].
84. Matthews, J. in *Proceedings of 27th International Cosmic Ray Conference — PoS(ICRC2001)* **1** (Jan. 2001), 261.
85. Matthews, J. *Astroparticle Physics* **22,** 387–397. ISSN: 0927-6505 (2005).
86. Mirzoyan, R. *Nuclear Physics B Proceedings Supplements* **239,** 26–34 (June 2013).
87. Morcuende, D. *et al.* Zenodo. Version v0.9.4. May 2022.

88. Noethe, M., Kosack, K., Nickel, L. & Peresano, M. in *Proceedings of 37th International Cosmic Ray Conference — PoS(ICRC2021)* **395** (2021), 744.

89. Pacini, D. *Il Nuovo Cimento* **3,** 93–100. arXiv: 1002.1810 [physics.hist-ph] (Dec. 1912).

90. Palatiello, M. *et al.* in *Proceedings of 35th International Cosmic Ray Conference — PoS(ICRC2017)* **301** (July 2017), 857. arXiv: 1708.09289 [astro-ph.IM].

91. Park, N. & VERITAS Collaboration. in *Proceedings of 34th International Cosmic Ray Conference — PoS(ICRC2015)* **34** (July 2015), 771. arXiv: 1508.07070 [astro-ph.IM].

92. Patricelli, B., Stamerra, A., Razzano, M., Pian, E. & Cella, G. *Journal of Cosmology and Astroparticle Physics* **2018,** 056. arXiv: 1801.05167 [astro-ph.HE] (May 2018).

93. Pühlhofer, G. *et al.* in *Optics for EUV, X-Ray, and Gamma-Ray Astronomy IX* (eds O'Dell, S. L. & Pareschi, G.) **11119** (Sept. 2019), 111191V.

94. Remy, Q. *et al.* in *Proceedings of 37th International Cosmic Ray Conference — PoS(ICRC2021)* (Sissa Medialab, July 2021).

95. Richardson, O. W. *Nature* **73,** 607 (Apr. 1906).

96. Ronchini, S. *et al. Astronomy & Astrophysics* **665,** A97. arXiv: 2204.01746 [astro-ph.HE] (Sept. 2022).

97. Ruiz, J. E. *et al.* in *Astronomical Society of the Pacific Conference Series* **532** (July 2022), 369. arXiv: 2101.09690 [astro-ph.IM].

98. Rybicki, G. B. & Lightman, A. P. (Wiley, New York, NY, 1985).

99. Sakurai, S., Depaoli, D. & Lopez-Coto, R. in *Proceedings of 36th International Cosmic Ray Conference — PoS(ICRC2019)* **36** (July 2019), 780. arXiv: 1907.09357 [astro-ph.IM].

100. Sitarek, J. *Galaxies* **10,** 21. arXiv: 2201.08611 [astro-ph.IM] (Jan. 2022).

101. Spurio, M. (Springer Cham, 2015).

102. Szanecki, M., Sobczyńska, D., Niedźwiecki, A., Sitarek, J. & Bednarek, W. *Astroparticle Physics* **67,** 33–46. arXiv: 1501.02586 [astro-ph.IM] (July 2015).

103. Tsiahina, A. *et al. Nuclear Instruments and Methods in Physics Research A* **1007,** 165413. arXiv: 2110.06030 [astro-ph.IM] (Aug. 2021).

104. Virtanen, P. *et al. Nature Methods* **17,** 261–272 (Feb. 2020).

105. Vuillaume, T., Donini, A. & Gasparetto, T. https://github.com/cta-observatory/divtel. 2022.

106. Weekes, T. C. *et al. Astrophysical Journal* **342,** 379 (July 1989).

107. Wilkinson, M. D. *et al. Scientific Data* **3,** 160018 (Mar. 2016).

108. Wulf, T. *Physikalische Zeitschrift* (1909).

109. Zanin, R. *et al.* in *Proceedings of 37th International Cosmic Ray Conference — PoS(ICRC2021)* **395** (2021), 005.